Spring 5-15-2017

Anisotropy and Emission from Air with Laser Filaments

Mohammadamin Rasoulof

Candidate

Department

This dissertation is approved, and it is acceptable in quality and form for publication:

Approved by the Dissertation Committee:

, Chairperson

Anisotropy and Emission from Air with Laser Filaments

by

M-Amin Rasoulof

DISSERTATION

Submitted in Partial Fulfillment of the
Requirements for the Degree of

Doctor of Philosophy
Optical Science and Engineering

The University of New Mexico

Albuquerque, New Mexico

July, 2017

Dedication

To Marziyeh,
a companion like ***no one*** else,
for her strength and love
and
to the memory of my brother ...

Acknowledgments

I would like to express my deep gratitudes to Dr. Jean-Claude Diels. He is the greatest advisor any student could ask for. I learned from him to be a passionate scientist and yet put humanity first. I had tons of nice moments with him in the lab and of course times that he got frustrated (which happened seldom). Many of his students have enjoyed a flight with him as the pilot. I also had a unique flight with him to San Jose with a couple of funny moments. Thank you Jean-Claude for everything and I hope we can continue to work together.

I also thank Dr. Ladan Arissian for her support and guidance on my academic work. She also helped me a lot to finish this work and I really appreciate her and hope to continue working with her in the future.

Special thanks to Dr. Jean-Pierre Wolf at the University of Geneva. He generously offered an internship opportunity in his group. I have enjoyed working with his team and would like to thank them all.

And my colleague Brian Kamer. He generously accepted to help me whenever I asked for help in the lab. He also performed some experiments to verify some of my data. Thank you bro!

Mrs. Linda Melville of Global Educations Office of UNM helped me through the immigration issues that I had. I feel indebted to her and thank her from bottom of my heart.

And my family who made it all possible with their companionship. Appreciating what they have done for me is beyond words and all I can say to them is THANK YOU!!!

Last but not least: All the people and friends who helped me and accompanied me during my stay in Albuquerque! Thank you and I wish you all the best.

Anisotropy and Emission from Air with Laser Filaments

by

M-Amin Rasoulof

Ph.D., Optical Science and Engineering, University of New Mexico, 2017

Abstract

Laser filaments are extremely interesting entities for their unique characteristics. The high intensity inside the laser filaments creates nonlinear effects that are useful in many areas of optics. The laser filamentation is an appealing tool in the stand-off spectroscopy for its ability to propagate over long distances while maintains its extreme intensity. However, depletion of energy hinders its propagation over any desired distance. In order to understand the effect of laser filaments on the transparent medium that they propagate through, one needs to investigate interaction of the laser filaments with the constituents of media. In this work we study the interaction of laser filaments with the molecular and atomic gaseous media. We try to separate the molecular and electronic responses of the media. Effect of laser polarization on the response of media is studied for linear and circular polarizations.

Emission from the nitrogen molecules and ions pumped by the laser filaments is studied. We show that there are emission in the forward and backward directions from nitrogen gas when it is irradiated by strong pulses that go through filamentation. Effects of laser polarization are also considered by using circular and linear laser pulses.

We propose a technique to enhance the longevity of 800 nm laser filaments. By spatially combining the UV laser filaments that have low loss and longer propagation distance one can feed the energy reservoir of the IR laser filament through four-wave mixing. We theoretically study this beam combining and show that this scheme is viable and under tunable conditions the energy will flow from the UV filament to the IR filament.

Contents

List of Figures x

List of Tables xiii

1 Introduction 1

1.1 Laser filamentation 1

1.1.1 Models of laser filamentation process 3

1.2 Laser filament properties 5

1.2.1 Intensity clamping inside the laser filaments 5

1.2.2 Energy reservoir of filaments 6

1.3 Energy loss in laser filamentation process 6

1.4 Optical Kerr effect 7

1.4.1 Molecular rotation by laser field 9

1.5 Polarization effect on laser filamentation 11

1.6 Emission from laser filaments 12

1.7 Scope of this work 14

2 Effects of Molecular Alignment on Laser Filament 16

2.1 Molecular rotation 16

2.2 Rotation of molecules while interacting with electromagnetic field . . 21

2.3 Interaction of linear molecules and linearly polarized electric field . . 24

2.4 Adiabatic vs. Nonadiabatic Alignment 26

2.5 Effects of pulse energy and duration on alignment 32

2.6 Effect of temperature on alignment 34

2.7 Fourier transform and $\langle\langle J^2 \rangle\rangle$ 35

2.8 Linear molecules interacting with arbitrarily polarized electric field . 36

2.9 Effect of molecular rotations on the refractive index of gaseous medium 40

2.10 Pump-probe experiment to investigate the rotational motion of molecules 43

2.10.1 Discussion 50

2.11 Energy exchange between the pump and the probe 54

2.12 Summary 56

3 Emission from laser filaments 60

3.1 Emission in the forward direction 63

3.2 Effect of the laser beam's angular momentum on the forward emission 69

3.3 Emission in the backward direction 71

3.4 Backward Raman scattering stimulated by laser filamentation . . . 74

3.5 Summary . . . 80

4 Filament refueling by Four-Wave Mixing **83**

4.1 Phase-matching with axicon . . . 84

4.2 Numerical simulations . . . 85

4.3 Summary . . . 89

A Euler rotations and polarizability transformation **91**

B $\langle \cos^2 \theta \rangle$ and selection rules **94**

C Vibrational and rotational states of molecules **97**

C.1 Rigid rotator model of diatomic molecules . . . 98

C.2 Oscillator model of diatomic molecules . . . 99

C.3 Nonrigid rotator model of diatomic molecules . . . 100

D Stimulated Raman scattering **103**

List of Figures

1.1 Schematic of self-guiding filamentation model 4

1.2 Schematic of alignment 10

2.1 Molecules with different symmetries 17

2.2 Boltzmann distribution of N_2 21

2.3 Effect of pulse duration on alignment 27

2.4 Effect of pulse duration on $\langle\langle \cos^2\theta_z \rangle\rangle$ 28

2.5 Effect of pulse duration on $\sqrt{\langle\langle J(J+1) \rangle\rangle}$ 29

2.6 Angular shape of a molecule interacting with laser field 30

2.7 $\langle\langle \cos^2\theta_x \rangle\rangle$ for N_2, O_2 and Air 31

2.8 $\langle\langle \cos^2\theta_x \rangle\rangle$ vs pulse energy 32

2.9 $\langle\langle \cos^2\theta_x \rangle\rangle$ vs pulse duration 33

2.10 $\langle\langle \cos^2\theta_x \rangle\rangle$ vs temperature 34

2.11 Variation of $\langle\langle J \rangle\rangle$ 36

2.12 Alignment by linearly and circularly polarized field 38

2.13 Effect of ellipticity on alignment 39

2.14 Pump-probe setup 44

2.15 Beam profile modulations due to molecular alignment evolution. . . 45

2.16 Spectrum modulations due to molecular alignment evolution. 45

2.17 Probe's center-of-mass temporal modulations 47

2.18 Fourier transform of probe's center-of-mass temporal modulations . 48

2.19 Wavelength shift of the probe in Argon 51

2.20 Wavelength shift of the probe in Nitrogen 53

2.21 Wavelength shift of probe in nitrogen near the zero-delay 54

2.22 Energy variation of the probe propagating in argon 56

2.23 Energy variation of the probe propagating in nitrogen 57

2.24 Energy variation of the probe propagating in nitrogen at zero delay . 58

3.1 Experiment setup to record the emission from N_2^+ in forward direction 62

3.2 Emission from N_2^+ at 427.8 nm 64

3.3 Raman and IR transitions in N_2^+ 65

3.4 Spectral lines fitted to the spectrum of 427.8 nm 66

3.5 Spectral lines fitted to the side peaks of 427.8 nm spectrum 67

3.6 $\langle\langle \cos^2\theta \rangle\rangle$ of N_2^+ 68

3.7 Schematic of the structure of a phase mask 70

3.8 Forward emission pumped by beam with angular momentum 70

3.9 Experiment setup for detection of backward emission from N_2 72

3.10 Backward emission from 800 nm filament 72

3.11 Backward emission signal for different energies 73

3.12 Schematic of different Raman scattering types 74

3.13 Spontaneous Raman signal from nitrogen molecules in air 76

3.14 Coherent Raman setup 77

3.15 Correlation between vibrational levels induced impulsively 79

3.16 Amplification of backward Raman signal 80

4.1 Phase-matching by axicon 85

4.2 Energy refueling by four-wave mixing 87

4.3 Effect of initial phases on four-wave-mixing 88

4.4 Four-wave mixing between an IR pulse and a DC, UV field. 89

A.1 Euler rotations 92

List of Tables

2.1 Molecular rotational properties of N_2, O_2 and CO_2 20

3.1 Properties of N_2^+ energy states 64

3.2 Properties of N_2 energy states 65

Chapter 1

Introduction

This chapter explains the essential concepts of laser filamentation and appreciates the importance of this phenomenon. We will mention the most significant applications of laser filamentation and will review a series of efforts in this field and toward the end of chapter we will put emphasis on the applications that will be used and developed in this work.

1.1 Laser filamentation

High intensity optical pulses experience appreciable Kerr effect as they pass through transparent media [1, 2]. The refractive index in a nonlinear medium up to the first power of intensity is

$$n = n_0 + n_2 I \tag{1.1}$$

Therefore, after propagation through length z of the medium, for a Gaussian shaped beam the phase across the beam profile is changed to

$$\Delta\varphi_{\text{Kerr}}(r, z) = -\frac{2\pi\ n_2}{\lambda}\ z\ I_0\ \exp(-\frac{2r^2}{w_0^2}) \tag{1.2}$$

On the other hand a Gaussian beam accumulates a phase due to diffraction which is

$$\Delta\varphi(r,z) = -\frac{k\ z}{2\rho_0^2} r^2 \tag{1.3}$$

where ρ_0 is the Rayleigh range of the beam. At a certain power diffraction and self-focusing will balance each other such that further increase of power will lead to collapse of the beam. The beam power at balance point is called the critical power, and is equal to

$$P_{\text{crit}} = \frac{\lambda^2}{8\pi\ n_0\ n_2} \tag{1.4}$$

where we used a parabolic approximation of the Gaussian function and considered the area of the Gaussian beam to be as $\pi w_0^2/2$. Although this formula gives the correct order of magnitude, numerical simulation (for continuous beams) lead to the most cited value of critical power [3]

$$P_{\text{crit}} = \frac{3.77\ \lambda^2}{8\pi\ n_0\ n_2} \tag{1.5}$$

A semi-empirical formula for the z distance for which beam collapses is [4]

$$z_{\text{crit}} = \frac{0.367\ \rho_0}{\sqrt{[(P/P_{\text{crit}})^{1/2} - 0.852]^2 - 0.0219}} \tag{1.6}$$

If the Gaussian beam is converging by passing through a lens this distance is changed to

$$\frac{1}{z_{f,\text{crit}}} = \frac{1}{z_{\text{crit}}} + \frac{1}{f} \tag{1.7}$$

These formulas remain qulitatively valid for ultrashort laser pulses despite the complexity of phenomena that exist for such short pulses [5]. Group velocity dispersion, multiphoton ionization, self-phase modulation, self-steepening and plasma generation bring different issues into play making it more difficult to define an exact critical power [6]. At atmospheric pressure the critical power of an infrared laser pulse centered at 800 nm of 100 fs duration and 400 μJ energy is approximately 3.2 GW [7].

1.1.1 Models of laser filamentation process

The simplest model of filamentation of ultrashort pulses is proposed by Akhmanov et. al. [8]. In this model the beam is self-focused due to the second-order nonlinear index, n_2. Beam collapse causes the increase of intensity which in return makes the higher nonlinear term, n_4, large enough. Negative sign of n_4 defocuses the beam and will balance the self-focusing. This model applies to the continuous beams [9].

Another proposed model for laser filament formation is based on balance between focusing and defocusing by optical Kerr and plasma effect, respectively. For $P > P_{\text{crit}}$ the pulse collapses and intensity increases to extreme values for which the nonlinear effects are strong. Multiphoton ionization rate is proportional to the nth power of the pulse intensity where n is the minimum number of photons absorbed to reach the ionization threshold [10], hence, by increase of the intensity inside the filament ionization rate increases and plasma channel is created. This plasma channel arrests further self-focusing and with its negative value of refractive index makes the beam diverge. If the diverged beam has sufficient energy to refocus, it collapses again and creates another negative refractive index by plasma formation. This sequence continues until the beam lacks enough energy to repeat this process. Fig. 1.1 shows this process schematically. This model is called as *self-guiding* model [11].

Another model that describes the laser filament formation is the *moving focus* model. In this scenario the ultrashort pulse is sliced into temporal stacks. The slices with powers higher than the critical power are focused in different distances depending on their difference with the critical power i.e. the closer their power to the critical power the shorter is their focusing distance. However, the slices with less power than the critical power are diffracted as a normal Gaussian beam. This model is completed when ionization is included, otherwise, the collapsed beam cannot propagate beyond the focus of each slice. Filamentation in solid state materials with

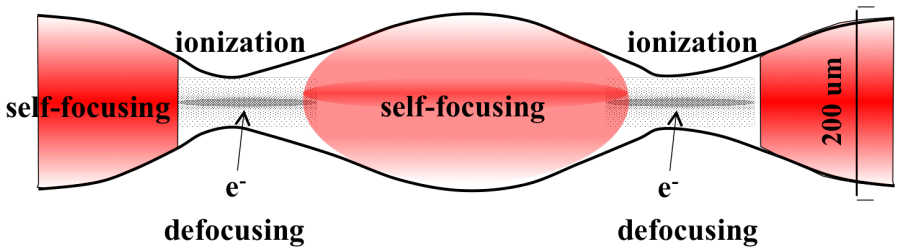

Figure 1.1: A schematic of self-guiding model for filamentation formation and propagation. See the text for details. Image courtesy of Dr. Jean-Claude Diels

nanosecond pulses is described by this model [12].

Combination of self-guiding and moving focus models describes the filament formation in form of a model called *spatial replenishment* [13]. This model combines the spatial model of self-guiding shown in Fig. 1.1 with the time slices of moving focus model. Numerical simulations show that self-focusing makes the pulse front to have the peak of intensity. This leading intense part ionizes the medium and causes the trail of the pulse to diffract due to the plasma's negative index of refraction. Also, intensity of the leading edge declines because of multiphoton absorption and in return the plasma generation is hindered. Upon the plasma reduction the pulse collapses again if the power is sufficient for self-focusing. This sequence is repeated until the power is less than the critical power and then the beam will diffract. A significant result of this model is that the beam propagates without appreciable change of beam size over distances longer than the Rayleigh range of a Gaussian beam.

There has been debates about the arrest of self-focusing by the higher-order Kerr terms instead of plasma generation [14], however, there are proofs that this assumption is not correct for filamentation process in gaseous media [15].

Femtosecond pulse duration is required in infrared wavelengths for filament formation. The avalanche breakdown of the gaseous medium that occurs due to inverse Bremsstrahlung needs picosecond time scales to establish [16]. Breakdown prevents

the required balance between self-focusing and defocusing. Hence, at infrared and longer wavelengths, we need pulses that are significantly shorter than picosecond [17]. It is not straightforward to establish laser sources with high powers and femtosecond time duration. In the UV region of electromagnetic spectrum the sub-picosecond duration is not a limit, therefore, UV pulses with longer durations can form filaments [18, 19]. There are UV sources with tens of picosecond durations and fractions of a Joule designed for laser filamentation [20]. UV filaments also enjoy the much smaller critical power than the IR filaments according to Eq. 1.4, and less nonlinear loss due to photons of higher energy i.e. less number of photons are required to ionize the molecules of air.

1.2 Laser filament properties

There are a variety of features that are brought in by the filament formation. Pulse self-compression [21, 22], spatial profile self-cleaning [23], super-continuum generation [24] and extended range propagation [25] are important properties of laser filaments. We would like to elaborate on the intensity-clamping and energy reservoir aspects of laser filaments.

1.2.1 Intensity clamping inside the laser filaments

It is shown that the intensity inside the filament core cannot be increased at will. Regardless of the initial power of the laser beam the value of intensity is limited to a range of $10^{13} - 10^{14}$ W/cm^2 [26, 27]. This could be intuitively deduced from the self-guiding model; when the beam inside the filament reaches a certain intensity, the ionization rate is high enough to generate a low density plasma cloud which defocuses the beam and limits the intensity to the *clamping intensity* value.

The second-order refractive index, n_2, is compensated by the generated plasma refractive index during the filament formation. Either of these refractive indices are proportional to the pressure, therefore, the clamping intensity is independent of pressure [28]. This has an important consequence in atmospheric research with laser filaments. Shooting a laser pulse vertically into the atmosphere, its intensity in different altitudes remains constant, however, the critical power in different altitudes is changed because of n_2 linear dependence on pressure (cf. Eq. 1.5). This implies that to generate filaments in higher altitudes one needs higher power and the higher the filament goes the larger becomes its area. Higher power inside the filament will result in more fluorescence signal which can be used in stand-off spectroscopy or remote-sensing.

1.2.2 Energy reservoir of filaments

Images of laser filaments show that at around the central filamentary part of the beam there is a halo. This halo is shown to be of crucial importance for the filament propagation and stability. It is shown that about 50% of the pulse energy is carried in the energy reservoir [29]. This energy reservoir makes the filament robust against the turbulence and interaction with particles e.g. it was shown that a filament obscured by particles with sizes comparable to filament diameter could be rebuilt after interacting with the particle [30].

1.3 Energy loss in laser filamentation process

There are three major drains of energy in laser filamentation. First, the self-generated plasma absorbs energy. Electrons of plasma are accelerated by the tail of the pulse and if the pulse is long enough these electrons can generate secondary electrons

through inverse Bremsstrahlung. Cross-section of inverse Bremsstrahlung is proportional to the square of wavelength [31], so, in infrared region it is much larger than ultraviolet region. As we already discussed, this is a limiting criterion on IR pulse durations to form a filament. Hence, for femtosecond IR filaments this energy leak is negligible because of pulse duration and in UV filaments this effect is very small because of small cross-section value.

Second cause of energy loss in laser filaments is the multiphoton absorption. Oxygen molecule needs 8 photons of 800 nm pulse to be ionized and nitrogen molecule takes 10 photons of this pulse. However, the number of UV photons required for ionization of oxygen molecule is three photons. This comparison suggests that the amount of absorbed energy over the same length of propagation is less for the case of UV filament. We also discussed that the UV sources used for filamentation have appreciably higher energies than the femtosecond IR sources. Then, UV filaments not only carry initial larger energy but they lose less energy as they propagate. We will show how this difference between IR and UV filaments will help to increase the IR filament propagation length.

Third drain of energy is produced by the processes that result in conical emission. Through conical emission the energy of laser filament is turned into other wavelengths that at the far-field are visible in the form of periphery rings. Čerenkov-type process, self-phase modulation or four-wave-mixing are invoked to explain the conical emission [32].

1.4 Optical Kerr effect

Intense optical pulses in molecular gaseous medium like air, which is a mixture of oxygen and nitrogen molecules, can manipulate the dipole moment of molecules (if any dipole moment exists for the molecules) or change the polarizability of molecular

constituents. Each of the situations induce totally different quantum behavior to the interaction of light and matter [33]. Variation of dipole moment needs absorption of photons and upon the return of excited electron, which occurs over time scales equal to the lifetime of the upper state, the emitted photon has generally a different wavelength. However, when the polarizability is changed by the laser field a Raman-type transition occurs and a photon is emitted in timescales that are proportional to the inverse of the energy difference of the levels involved. In this case one photon is scattered by the molecule and not absorbed.

There are three different types of scattering from molecules. The first is due to the electron's motion in molecule. When irradiated by the laser field the electronic change of polarizability scatters the impinging photon in timescales shorter than a femtosecond. This is the *electronic Kerr* contribution to the nonlinear refractive index. Molecules have two other degrees of freedom; vibration of nuclei from their equilibrium position and rotation of the nuclei around their center of mass. Any change to the internuclear distance changes the polarizability of molecule. Rotation of molecules also change their polarizability and contributes to the refractive index just like electronic motion and vibrational motion of nuclei.

Vibrational motion has minimum energy according to the quantum mechanical model of a vibrating system. The rotational motion, however, can have zero energy. We discuss in Appendix C that vibrational and rotational energies have discrete values and the spacing of vibrational levels are many times the spacing between the rotational energy levels. In other words the response time of the rotational polarizability to the laser field is much slower than the response time of the vibrational polarizability. In nitrogen molecules the vibrational period is about 14 fs and the period of rotational motion is about 8 picoseconds. Hence, the total refractive index due to the Kerr effect depends on the pulse duration. If the pulse is shorter than the vibrational period of the molecule only the electronic Kerr contributes to the refrac-

tive index. It is shown that for femtosecond-long pulses, the rotational effects make the wake of the pulse highly anisotropic. This has severe consequences on the pulses that are following the first pulse. We will discuss this effect on how the refractive index of medium is changed under the influence of laser filamentation.

1.4.1 Molecular rotation by laser field

Interaction of a laser with a molecule without permanent dipole moment induces a dipole moment, μ, by separating the centers of positive and negative charges. This dipole moment is proportional to the electric field through the polarizability tensor, α. The laser makes the induced dipole moment to be aligned along the same direction as the electric field. Assuming a linear molecule with diagonal polarizability tensor, the energy of molecule inside the electric field is changed as

$$U = -\frac{1}{2}\vec{\mu}\cdot\vec{E} \tag{1.8}$$

Let us assume that the electric field is linearly polarized and polarizability of a linear molecule along its symmetry axis is represented by $\alpha_{\parallel}$ and polarizability in the plane normal to the symmetry axis is shown by $\alpha_{\perp}$. Hence

$$\begin{aligned} U &= -\frac{|\vec{E}|^2}{2}\left[\alpha_{\parallel}\cos^2\theta + \alpha_{\perp}\sin^2\theta\right] \\ &= -\frac{|\vec{E}|^2}{2}\left[\Delta\alpha\ \cos^2\theta + \alpha_{\perp}\right] \end{aligned} \tag{1.9}$$

where $\Delta\alpha = \alpha_{\parallel} - \alpha_{\perp}$ and θ is the polar angle between the field's axis of polarization and the symmetry axis of molecule (cf. Fig. 1.2). This implies that the molecule rotates to align along the field axis, $\theta = 0$, so it maintains minimum energy. We know that the refractive index is related to the average of the polarizability tensor as

$$n^2 = 1 + N\langle\alpha\rangle \tag{1.10}$$

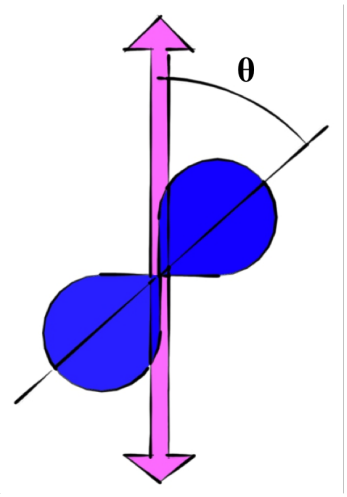

Figure 1.2: Orientation of a linear molecule with respect to a linearly polarized electric field. Pink double arrow represents the electric field and solid line shows the symmetry angle of molecule.

From Eq. 1.9 we replace $\langle\alpha\rangle$, hence

$$n^2 = 1 + N\Big[\Delta\alpha\ \langle\cos^2\theta\rangle + \alpha_\perp\Big] \tag{1.11}$$

In absence of electric field the molecules are directed in space isotropically, then $\langle\cos^2\theta\rangle = 1/3$. Hence, the average polarizability is

$$n_0^2 = 1 + N\Big[\frac{\Delta\alpha}{3} + \alpha_\perp\Big] \tag{1.12}$$

Differential refractive index, $\Delta n = n - n_0$, can be derived from the approximation that $n^2 - n_0^2 \approx (n - n_0)(2n_0)$, so

$$\Delta n = \frac{N\Delta\alpha}{2n_0}\Big[\langle\cos^2\theta\rangle - \frac{1}{3}\Big] \tag{1.13}$$

This formula implies that the refractive index of a medium depends on the angle between the electric field and the molecular axis. As a result an ultrashort pulse passing through air rotates the molecules according to Eq. 1.9. The trailing edge of this pulse is affected by the rotation of molecules as shown in Eq. 1.13.

It is shown that the duration of the interacting pulse is very important in the type of behavior that the molecular ensemble shows [34]. For the pulses with their duration equal or longer than the period of rotation, molecules start to align along the linear electric field and they gain the smallest angle with the field at the peak of the pulse. As the pulse leaves the medium, molecules are returned to their initial alignment in the absence of the field. However, if the pulse duration is much shorter than the rotational period of molecules, rotational levels are excited impulsively and as the pulse vanishes molecules continue to change their rotation over timescales much longer than their period of rotation.

Hence, for the femtosecond pulses in air where the rotational period of nitrogen and oxygen are of the order of picosecond we should expect that the molecular rotations persist for many picoseconds after the pulse turn-off. According to Eq. 1.13 if $\langle \cos^2 \theta_Z \rangle$ is a function of time. As function of the time the refractive index is therefore increased or decreased compared to its value in absence of the pulse. If another pulse with spatial overlap but temporal delay with the first pulse passes the medium it experiences different refractive indices depending on the its delay. We will show how this delay can manipulate the properties of the second pulse and its propagation.

1.5 Polarization effect on laser filamentation

There are a variety of differences between linear and circular polarization in terms of filament formation and emission. Fibich et. al. showed that circularly polarized beams are less likely to form multiple filamentation i.e. the initial beam does not break into more than one filament [35, 36]. After Hauri and colleagues compressed a linear pulse by laser filamentation [21], Liu et. al. showed that circularly polarized light can be compressed with initial intensity 3/2 the initial intensity of a linear pulse

without breaking into multiple filements [37].

It is shown by Diels et. al. that the pre-filamentation phase is playing a decisive role for circular filaments [38]. They showed that if the circularly polarized beam is focused into vaccum and then emerge into the atmospheric pressure no filament forms.

Circular and linear polarizations are different in terms of ionizing the medium, too [39]. This affects specially the emission from laser filaments which we will discuss in next section.

In this work we will show that the rotational Kerr effect depends on the polarization of the beam and how this difference affects the anisotropy in medium.

1.6 Emission from laser filaments

We discussed that laser filamentation process brings highly nonlinear effects because of the extreme intensities inside the filament core. A variety of nonlinear emissions are enhanced by filamentation e.g. high-order harmonic generation and conical emission. One of the most interesting features of laser filaments is their constant beam size over long distances and their property that one can adjust the position of filament formation from the laser source by changing the pulse chirp [40, 41]. These features enables us to initiate high intensity beams at desired position in space and keep this intensity along extended distances.

High intensity inside the laser filaments excites the constituents of air, which emit in form of spontaneous and stimulated emission. Dogariu et. al showed backward emission from oxygen molecules in air pumped by 226 nm pulse [42]. This method generates high gain emission at 854 nm at atmospheric pressure, however, the absorption and scattering at 226 nm makes the excitation in far distances difficult. The

pumping mechanism of this emission is investigated and understood. Stimulated emission from nitrogen molecules has been a trending subject due to the abundance of nitrogen in air which makes the air a fascinating lasing medium.

Yao et. al. showed stimulated emission in forward direction from nitrogen cation [43]. The observed lines belong to transitions between different vibrational states of transition $B^2\Sigma_u^+ \rightarrow X^2\Sigma_g^+$ of N_2^+ [33]. Since the first observation, there have been exhaustive studies about the properties of this emission and the pumping mechanism. A candidate process to explain the pumping of $B^2\Sigma_u^+$ is the seeding the excited ions by the tail of super-continuum generated by the filamentation process and possible local second-harmonic due to focusing effects [44]. However, *so far there has been no inclusive explanation* of the process that explains all the involved transitions between different electronic and vibrational levels of N_2^+.

Backward emission from nitrogen molecules have been detected by exciting them through interaction with laser filaments. The emitted lines correspond to the transitions between various vibrational levels in the electronic transition $C^3\Pi_u \rightarrow B^3\Pi_g$ [33]. Kartashov et. al. detected backward emission from nitrogen molecules of air pumped by 1053 nm laser filaments [45]. It is claimed that the lasing effect in this experiment is pumped by the third-harmonic of laser generated through filamentation [46]. We already mentioned the limit on the pulse duration in near-IR and longer pulses in order to form filaments which limits the initial energy of pulses a well. Hence, this limit encourages the scientists to use near-IR filaments where the sources are widely available. Backward emission from nitrogen molecules pumped by 800 nm pulses has been recently extensively studied. Mitryukovskiy et. al. showed stimulated emission in backward direction from nitrogen molecules pumped by 800 nm circularly polarized laser pulses [47]. Polarization dependence sheds some light on the pumping mechanism of nitrogen molecules, though, the full description of the process is debatable [48].

1.7 Scope of this work

We are interested in utilizing the infrared laser filamentation in stand-off spectroscopy. As discussed before, nonlinear loss in IR filaments depletes the filament energy and limits the length of laser filament. The magnitude of backward signals depend on the length of filament, hence, longer filaments create better signal-to-noise ratio. On the other hand the UV filaments carry more energies and can propagate over very long distances. If the energy reservoir of an IR filament is fed by UV energy, then the IR filament can propagate over longer distances. For this energy flow from UV to IR filaments, their electric fields should be coupled through a physical process. We propose the four-wave mixing process between 266 nm and 800 nm fields to direct energy from the former to the later field. In four-wave mixing the electric fields are related to each other by third-order susceptibility, $\chi^{(3)}$. We mentioned that $\chi^{(3)}$ has molecular and electronic origins. Therefore, the importance of studying the $\chi^{(3)}$ dynamics under influence of a laser field is twofold. First, it helps to determine the strength of coupling between the UV and IR fields. Second, as we pointed out in previous sections, ultrashort laser pulses propagating through air manipulate the refractive index of air for extended time scales after they pass the environment. Since the four-wave mixing requires spatial beam combining we need to understand the effect of laser filaments on the refractive index of air.

In Chapter 2 we investigate the pulse propagation effect on $\chi^{(3)}$. Numerical treatment is used to simulate the rotational and electronic Kerr effect on the propagation of a second pulse through the wake of a laser filament. Application of laser filamentation in stand-off spectroscopy requires the knowledge of emission from laser filaments. Hence, we experimentally examined the backward and forward emission from filaments and effects of laser polarization and angular momentum of the beam. These results are presented in Chapter 3. At the end of this chapter we will discuss numerical calculations to simulate backward Raman scattering pumped by an 800

nm filament and probed by a UV pulse. In Chapter 4 four-wave mixing between UV and IR fields is examined numerically to determine the feasibility of pumping up the IR filament reservoir by UV filament energy through four-wave mixing.

Chapter 2

Effects of Molecular Alignment on Laser Filament

In this chapter we will examine the variation of third-order susceptibility through interaction by intense ultrashort laser pulses. A numerical study of effect of laser pulse on the rotational motion of molecules is performed. Changes of refractive index due to molecular alignment is presented. Finally, we show the results of a pump-probe experiment in air to test the numerical outcomes and to investigate the effect of laser filament propagation on the medium.

2.1 Molecular rotation

Rotational motion of molecules could be equivalently pictured as the rotation of classical objects. Similar to their classical counterparts molecules have a moment of inertia, $\bar{\mathrm{I}}$, an angular momentum, $\hat{J}$ from which their rotational energy can be

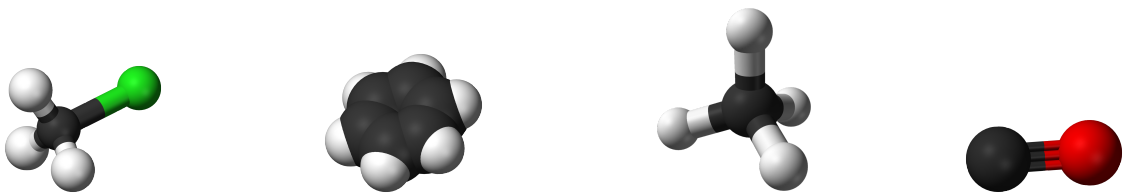

(a) (b) (c) (d)

Figure 2.1: (a) Chloromethane, prolate symmetric top, (b) Benzene, oblate symmetric top, (c) Methane, spherical top molecule and (d) Carbon monoxide, linear molecule

expressed. For symmetric-top molecules

$$\hat{H}_{\text{rot}} = \frac{\hat{J}_X^2}{2\bar{\text{I}}_{XX}} + \frac{\hat{J}_Y^2}{2\bar{\text{I}}_{YY}} + \frac{\hat{J}_Z^2}{2\bar{\text{I}}_{ZZ}} \tag{2.1}$$

where $\hat{J}_k$ is the total angular momentum operator in body-fixed coordinate system with $k = X, Y, Z$, $\bar{\text{I}}_{kk} = \sum_i m_i(r_i^{e2} - r_{ik}^{e\,2})$ are the moments of inertia around the k axis and i accounts for the components of the system. r_i^e denotes that distances are considered at vibrational equilibrium of the molecule, i.e., effects of nonrigid model of molecules are ignored. The body-fixed coordinate system is chosen in a way that for symmetric-top molecules, the off-diagonal matrix elements of the moment of inertia $\bar{\text{I}}_{kk'} = -\sum_i m_i(r_{ik}^e r_{ik'}^e)$ are equal to zero. Principal moments of inertia are related as $\bar{\text{I}}_{aa} \leq \bar{\text{I}}_{bb} \leq \bar{\text{I}}_{cc}$ by convention with a, b and c the body-fixed axes. $\bar{\text{I}}_{aa} \leq \bar{\text{I}}_{bb} = \bar{\text{I}}_{cc}$ represents a prolate symmetric-top molecule e.g. chloromethane, $\bar{\text{I}}_{aa} = \bar{\text{I}}_{bb} \leq \bar{\text{I}}_{cc}$ shows an oblate symmetric-top molecule e.g. benzene, $\bar{\text{I}}_{aa} = \bar{\text{I}}_{bb} = \bar{\text{I}}_{cc}$ shows spherical-top molecule and $\bar{\text{I}}_{aa} = 0, \bar{\text{I}}_{bb} = \bar{\text{I}}_{cc}$ defines the linear molecule e.g. O_2 and N_2, Fig. 2.1.

By introducing the coefficients $A = 1/2\bar{\text{I}}_{aa}$, $B = 1/2\bar{\text{I}}_{bb}$ and $C = 1/2\bar{\text{I}}_{cc}$ into

Eq. 2.1, this equation in terms of the axes along the principal moments of inertia is

$$\hat{H}_{\text{rot}} = A\hat{J}_a^2 + B\hat{J}_b^2 + C\hat{J}_c^2 \ . \tag{2.2}$$

Considering the relation between the angular momentum components, $\hat{J}^2 = \hat{J}_X^2 + \hat{J}_Y^2 + \hat{J}_Z^2$ in the body-fixed coordinate system, by proper assignment of axes one has

$$\hat{H}_{\text{rot}} = C\hat{J}^2 + (A - C)\hat{J}_Z^2 \tag{2.3}$$

with the eigenvalues

$$E_{JK} = \left[CJ(J+1) + (A-C)K^2\right]\hbar^2 \tag{2.4}$$

for a prolate symmetric-top molecule with $a \equiv$ Z and

$$\hat{H}_{\text{rot}} = A\hat{J}^2 + (C - A)\hat{J}_Z^2 \tag{2.5}$$

with the eigenvalues

$$E_{JK} = \left[AJ(J+1) + (C-A)K^2\right]\hbar^2 \tag{2.6}$$

for an oblate symmetric-top molecule with $c \equiv$ Z.

K is the projection of the total angular momentum along the Z axis. Note that a linear molecule is a special form of a prolate molecule and the projection of the

total angular momentum along Z axis is small enough to consider rotation around Z to be zero, $K = 0$, although there are exception in linear molecules such as NO with $K \neq 0$ [33]. Classically it is analogous to a very narrow rod for which the moment of inertia along its long axis is negligible compared the other two axis perpendicular to its long axis. Hence the rotational Hamiltonian of a linear molecule $A \ll C$ is

$$\hat{H}_{\text{rot}} = \frac{\hat{J}^2}{2\bar{\text{I}}_{bb}} = \frac{\hat{J}^2}{2\bar{\text{I}}_{cc}}. \tag{2.7}$$

We demonstrate the eigenvalue relation of the Hamiltonian in Eq. 2.7 as

$$\hat{H}_{\text{rot}} \ |j\rangle = \frac{\hbar^2}{4\pi\bar{\text{I}}_{bb}} \ |j\rangle \tag{2.8}$$

where $|j\rangle$ is the eigenfunction of this Hamiltonian. However, it is common to report the spectroscopical values in units of m^{-1}. Hence, we divide Eq. 2.8 by "hc" and represent the eigenvalue with

$$B = \frac{\hbar}{4\pi \ c \ \bar{\text{I}}_{bb}} \ . \tag{2.9}$$

See Table 2.1 for the values of B for different molecules.

In many elementary quantum mechanics books the eigenvalues and eigenfunctions of the total angular momentum are calculated. The commutation relation between the angular momentum components are

$$\begin{aligned} \left[\hat{J}^2, \hat{J}_{\pm}\right] &= 0 \\ \left[\hat{J}^2, \hat{J}_z\right] &= 0 \\ \left[\hat{J}_x, \hat{J}_y\right] &= i\hbar\hat{J}_z \end{aligned} \tag{2.10}$$

where $\hat{J}_{\pm} = \hat{J}_x \pm i\hat{J}_y$ and the wavefunction that describes the rotational motion of a quantum system is [49]

$$|\psi(\theta,\phi)\rangle = \sum_{J} \sum_{M=-J}^{J} a_{JM} Y_{JM}(\theta,\phi) \tag{2.11}$$

where Y_{JM} is the spherical harmonics function and θ and ϕ are the polar and azimuthal angles with the choice of quantum axis along the Z axis, J is the orbital angular momentum quantum number and M is the projection of the total angular momentum along the z axis of the space-fixed coordinate system.

The probability that a rotational system in thermal equilibrium and temperature T is in J state with its rotational energy $E_J = BJ(J+1)$, is defined by the Boltzmann distribution

$$P(E_J) = \frac{1}{Z}\, g_J\, (2J+1)\, \exp\Big(-\frac{E_J}{k_B T}\Big) \tag{2.12}$$

where Z, g_J, k_B are the partition function, nuclear spin statistics and the Boltzmann constant. We multiply the term $(2J+1)$ to account for the number of degenerate M states for each J state. The probability distribution for nitrogen at T=295°K is shown in Fig. 2.2 (for the related constants see Table 2.1)

Molecule	$B(\mathrm{cm}^{-1})$	$D_0(\mathrm{cm}^{-1})$	$\Delta\alpha_\nu(\mathring{A}^3)$	g_{even}	g_{odd}
N_2	1.989581	5.76×10^{-6}	1	2	1
O_2	1.4297	4.839×10^{-6}	1.15	0	1
CO_2	0.3902	0.135×10^{-6}	2	1	0

Table 2.1: Molecular rotational properties of N_2, O_2 and CO_2 [33, 50]

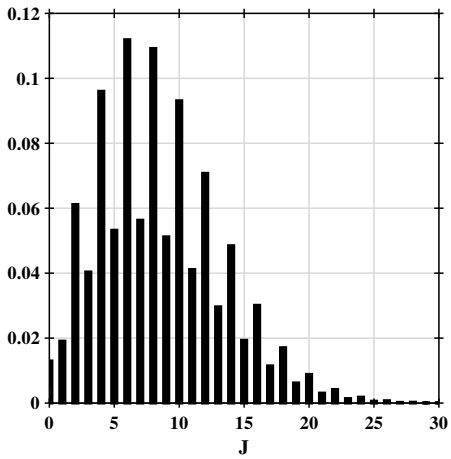

Figure 2.2: Boltzmann distribution of nitrogen molecule at T=295°K

2.2 Rotation of molecules while interacting with electromagnetic field

Non-perturbative interaction of a rotating quantum system with a laser field is considered in this section. The electric field is treated classically and is presented as

$$\vec{E}(t,z) = \frac{1}{2}[\tilde{\boldsymbol{\mathcal{E}}}(t)e^{i\omega t - kz} + c.c.] \tag{2.13}$$

where $\tilde{\boldsymbol{\mathcal{E}}}$ and ω are the field amplitude and the frequency of the field, respectively. Polarization axis of the linearly polarized field is in x direction, however, for elliptically polarized field the polarization ellipse lies in x-y plane, by convention. We assume the propagation in z direction

$$\tilde{\boldsymbol{\mathcal{E}}}(t) = \tilde{\mathcal{E}}(t)\hat{x} \qquad \text{Linear polarization} \tag{2.14}$$

$$\tilde{\boldsymbol{\mathcal{E}}}(t) = \tilde{\mathcal{E}}(t)(\cos\eta\ \hat{x} - i\ \sin\eta\ \hat{y}) \qquad \text{Elliptical polarization} \tag{2.15}$$

with $\tan\eta$ the ratio of the minor axis to the major axis of the ellipse and $\tilde{\mathcal{E}}(t)$ is the complex envelope of electric field. This method of defining the elliptical polarization

inserts the helicity of the field into the mathematical definition. For circular polarization $\eta = \pm\pi/4$ with the choice of different signs for right-handed and left-handed rotation of the field.

The field works on the molecule by inducing a dipole moment and depositing energy to align this dipole along direction of field

$$\hat{H}_{\text{int}} = -\mu \cdot \vec{E}(t) \tag{2.16}$$

where the dipole moment is defined as the sum over the coordinates of all the electrons; $\mu = \sum_j e\, \hat{r}_j$. The orthogonal set of basis for this Hamiltonian is defined by an electronic quantum number, ϵ, a vibrational quantum number, v, and a rotational quantum number, j. Hence any wavefunction is expanded as

$$|\Psi\rangle = \sum_{\epsilon,v,j} a_{\epsilon,v,j} |\epsilon, \nu, j\rangle \tag{2.17}$$

When the field frequency is tuned off the vibrational transitions but photon energy is much larger than separation of rotational levels of the same electronic and vibrational states the Hamiltonian is [51]

$$\hat{H}_{\text{int}} = -\frac{1}{4} \sum_{\rho\rho'} \tilde{\mathcal{E}}_\rho \alpha_{\rho\rho'} \tilde{\mathcal{E}}^*_{\rho'} \tag{2.18}$$

where $\rho = x, y, z$ are the spaced-fixed coordinates and are related to the body-fixed coordinate system, $k = X, Y, Z$ by Euler rotations (see Fig. A.1). Note that by comparing equations 2.16 and 2.18 we have

$$\hat{H}_{\text{int}} = -\frac{1}{4} \sum_{\rho} \tilde{\mathcal{E}}_\rho\ \mu_\rho, \qquad \mu_\rho = \sum_{\rho'} \alpha_{\rho\rho'}\ \tilde{\mathcal{E}}'_\rho. \tag{2.19}$$

With proper Euler rotation terms the polarizability in space-fixed frame is

$$\alpha_{\rho\rho'} = \sum_{kk'} \langle\rho|k\rangle \alpha_{kk'} \langle k'|\rho'\rangle \tag{2.20}$$

Euler rotations relate the space-fixed and body-fixed coordinates (cf. Appendix A for transformation matrices). For the case of electric field linearly polarized in x direction Eq. 2.20 is expanded as

$$\begin{aligned}\alpha_{xx} &= \langle x|X\rangle\alpha_{\perp}\langle X|x\rangle + \langle x|Y\rangle\alpha_{\perp}\langle Y|x\rangle + \langle x|Z\rangle\alpha_{\parallel}\langle Z|x\rangle \\ &= -\alpha_{\perp}\sin^2\theta\cos^2\phi + \alpha_{\perp} + \alpha_{\parallel}\sin^2\theta\cos^2\phi \end{aligned} \tag{2.21}$$

where for linear molecule we assumed that $\alpha_{XX} = \alpha_{YY} = \alpha_{\perp}$ and $\alpha_{ZZ} = \alpha_{\parallel}$.

Hence, from equations 2.21 and 2.15 the Hamiltonian of Eq. 2.18 becomes

$$\hat{H}_{\text{int}} = -\frac{|\tilde{\mathcal{E}}(t)|^2}{4}\Big\{\alpha_{\parallel}\sin^2\theta\cos^2\phi - \alpha_{\perp}\sin^2\theta\cos^2\phi + \alpha_{\perp}\Big\} \tag{2.22}$$

Note that the Hamiltonian in this equation is shifted by $\alpha_{\perp}$ amount which is angle-independent and does not change the rotational dynamics except a shift of energy. The interaction Hamiltonian in Eq. 2.22 is reduced to

$$\hat{H}_{\text{int}}^{\text{Linear}} = -\frac{|\tilde{\mathcal{E}}(t)|^2}{4}\Delta\alpha\cos^2\theta_x \tag{2.23}$$

where $\cos^2\theta_x = \sin^2\theta\cos^2\phi$ and $\Delta\alpha = \alpha_{\parallel} - \alpha_{\perp}$ is the difference of polarizability along the molecular axis and perpendicular to that.

For elliptical polarization, Eq. 2.15, the Hamiltonian of interaction between electric field and a molecule is derived by Eq. 2.18 and Eq. 2.20 and is [52]

$$\begin{aligned}\hat{H}_{\text{int}}^{\text{Elliptical}} = -\frac{|\tilde{\mathcal{E}}(t)|^2}{4} \quad \Big\{ & \quad (\alpha_{ZZ} - \alpha_{XX})\big[(|e_x|^2 - |e_y|^2)\langle x|Z\rangle^2 + |e_y|^2\sin^2\theta\big] \\ & + \quad (\alpha_{YY} - \alpha_{XX})\big[(|e_x|^2 - |e_y|^2)\langle x|Y\rangle^2 \\ & + \quad |e_y|^2(\cos^2\psi + \cos^2\theta\sin^2\psi)\big]\Big\} \end{aligned} \tag{2.24}$$

$$\begin{aligned}\langle x|Z\rangle &= -\sin\theta\cos\phi \\ \langle x|Y\rangle &= -\sin\phi\cos\psi - \cos\theta\cos\phi\sin\psi\end{aligned}$$

where $e_x = \cos\eta$ and $e_y = -i\sin\eta$. Hence, for a linear molecule interacting with an elliptically polarized field we have

$$\hat{H}_{\rm int}^{\rm Elliptical} = -\frac{|\tilde{\mathcal{E}}(t)|^2\Delta\alpha}{4}\Big[(|e_x|^2 - |e_y|^2)\sin^2\theta\cos^2\phi + |e_y|^2\sin^2\theta\Big] \tag{2.25}$$

where $\Delta\alpha$ is the same as in Eq. 2.23.

2.3 Interaction of linear molecules and linearly polarized electric field

Time evolution of rotational states is determined by solving the Schrödinger equation, numerically. Schrödinger equation for interaction of linear electric field with a linear molecule is

$$\begin{aligned} i\hbar\frac{\partial|\Psi(\theta,t)\rangle}{\partial t} &= \Big[\frac{J(J+1)\hbar^2}{2\bar{\rm I}} - \frac{\Delta\alpha}{4}|\tilde{\mathcal{E}}(t)|^2\cos^2\theta_x\Big]|\Psi(\theta,t)\rangle \\ &= \Big[\frac{J(J+1)\hbar^2}{2\bar{\rm I}} - \frac{2\pi\Delta\alpha_\nu}{c}|I(t)|^2\cos^2\theta_x\Big]|\Psi(\theta,t)\rangle \end{aligned} \tag{2.26}$$

where we assume the electric field as plane wave with $I(t) = c\epsilon_0/2|\tilde{\mathcal{E}}(t)|^2$. $\Delta\alpha$ which is defined in Eq. 2.20 and has dimensions of $\mathrm{CV^{-1}m^2}$ is related to $\Delta\alpha_\nu$ with $\mathrm{m^3}$ dimensions as $\Delta\alpha_\nu = \Delta\alpha/4\pi\epsilon_0$.

In spectroscopy it is common to define energy units in $\mathrm{m^{-1}}$, so Eq. 2.26 in $\mathrm{m^{-1}}$ units is

$$\frac{\partial|\Psi(\theta,t)\rangle}{\partial t} = -2\pi\, i\, c\Big[J(J+1)B - \frac{\Delta\alpha_\nu}{\hbar c^2}|I(t)|^2\cos^2\theta_x\Big]|\Psi(\theta,t)\rangle \tag{2.27}$$

where $\Delta\alpha_\nu$ and B are given for air molecules in Table 2.1.

We assume that the frequency of electric field is tuned far from any electronic or vibrational transition. Hence the electronic and vibrational numbers in Eq. 2.17

remain the same and the choice of orthogonal basis is the matter of convenience and here they are chosen to be the spherical harmonics in Eq. 2.11. This choice makes the post-pulse part of simulations easier to calculate. Introducing the Eq. 2.11 into Eq. 2.26 results in

$$\begin{aligned}\dot{a}_{JM} = \; &- \; 2i\pi c\Big[J(J+1)B\; a_{JM} \\ &- \; \frac{\Delta\alpha_\nu}{\hbar c^2}|I(t)|^2 \sum_{J,J'}\sum_{M,M'} a_{JM}a^*_{J'M'}\langle J', M'|\cos^2\theta_x|J, M\rangle\Big].\end{aligned} \tag{2.28}$$

$|J, M\rangle$ represents the spherical harmonics. The bracket of second term in right-hand-side has analytical solutions in terms of J and M. See Appendix B for details. Linearly polarized electric field couples the states for which $\Delta J = 0, \pm 2$ and $\Delta M = 0, \pm 2$.

After the electric field is turned-off or the pulse passes the molecular sample the rotational states evolve freely with the rotation Hamiltonian Eq. 2.7 and we have

$$|\psi(\theta,\phi)\rangle = \sum_{J,M} a_{JM}\; \exp\Big(\frac{-i\hat{H}_{\rm rot}t}{\hbar}\Big)|J, M\rangle \tag{2.29}$$

where a_{JM} is the expansion coefficient at the end of the pulse duration. A measure that shows the angular alignment of molecules is

$$\langle\cos^2\theta\rangle = \sum_{J,J'}\sum_{M,M'} a_{JM}a^*_{J'M'}\langle J', M'|\cos^2\theta|J, M\rangle \tag{2.30}$$

This measure for freely evolving molecules is

$$\langle\cos^2\theta\rangle = \sum_{J,J'}\sum_{M,M'} a_{JM}a^*_{J'M'}\langle J', M'|\cos^2\theta|J, M\rangle\exp\Big[-i\frac{(E_J - E'_J)t}{\hbar}\Big] \tag{2.31}$$

The average of this measure for an ensemble of molecules in thermal equilibrium is

$$\langle\langle\cos^2\theta\rangle\rangle = \frac{1}{Z}\sum_{J,M} g_J\; \exp\Big(-\frac{E_J}{k_BT}\Big)\langle\cos^2\theta\rangle_{J,M} \tag{2.32}$$

where the Boltzmann distribution in Eq. 2.12 is used to average the $\langle\cos^2\theta\rangle$ for the rotational states initially in J and M state, e.g. $\langle\cos^2\theta\rangle_{J,M}$ means that we assume that only $|J,M\rangle = 1$ and population of the rest of states is zero, then we calculate $\langle\cos^2\theta\rangle$ and multiply it by its thermal weight and the same for the rest of states. Since we should account for all M states then the $(2J+1)$ factor vanishes as weight of them is the same for each J state.

In order to solve Eq. 2.29 numerically we use the Runge-Kutta 4th method to calculate $a_{JM}(t+\Delta t)$ from $a_{JM}(t)$,

$$a_{JM}(t+\Delta t) = a_{JM}(t) + \frac{k_1}{6} + \frac{k_2}{3} + \frac{k_3}{3} + \frac{k_4}{6} \tag{2.33}$$

where

$$\begin{aligned} k_1 &= \Delta t\ f_{JM}(t, a_{JM}) \\ k_2 &= \Delta t\ f_{JM}(t+\frac{\Delta t}{2}, a_{JM}+\frac{1}{2}k_1) \\ k_3 &= \Delta t\ f_{JM}(t+\frac{\Delta t}{2}, a_{JM}+\frac{1}{2}k_2) \\ k_4 &= \Delta t\ f_{JM}(t+\Delta t, a_{JM}+k_3) \end{aligned} \tag{2.34}$$

and f_{JM} is the right-hand-side of Eq. 2.29.

2.4 Adiabatic vs. Nonadiabatic Alignment

The rotational period of a molecule in absence of electric field is $\tau_{\rm rot} = 1/2Bc$ with c the speed of light. From Eq. 2.29 one finds that the longest period of oscillations is for $J = 1$ ($J = 0$ is non-oscillatory) and the oscillation period of higher rotational states are intgral fractions of $J = 1$. This is a scale to define two regimes of interaction with respect to the pulse duration τ: adiabatic regime ($\tau > \tau_{\rm rot}$) and nonadiabatic or impulsive regime $\tau < \tau_{\rm rot}$. These induce completely different phenomena. There

are analytical treatments of problem to understand this difference [53], however, numerical simulations presented in Fig. 2.3 show how rotational states evolve at different regimes. We assume that molecule is at zero temperature so only $J = 0$ is

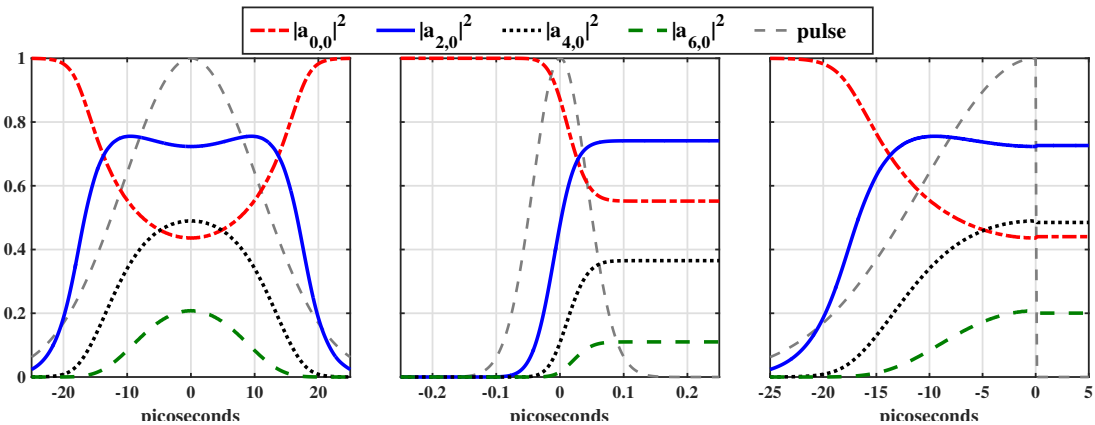

Figure 2.3: Dynamics of wavefunction coefficients, $a_{J,M}$ as function of time for N_2 at T=0°K for different pulse shapes and durations. (left) [$\tau_{\text{on}} = 25$ ps, $\tau_{\text{off}} = 25$ ps], (middle) [$\tau_{\text{on}} = 100$ fs, $\tau_{\text{off}} = 100$ fs] and (right) [$\tau_{\text{on}} = 25$ ps, $\tau_{\text{off}} = 100$ fs]. Normalized pulse shape is shown with grey line. τ_{on} is the rising half-width at half-maximum of the rising side of pulse and τ_{off} is the rising half-width at half-maximum of the falling side of pulse.

populated, initially. In adiabatic regime, as shown on the left panel of Fig. 2.3 and Fig. 2.4, higher J states are populated at presence of the pulse, though, by change of the pulse slope to negative, the population rolls back to $J = 0$ and upon the pulse turn-off the system is back to its initial condition before the pulse. This requires the pulse duration to be longer than the rotational period. This is the adiabatic regime.

Nonadiabatic regime is shown in Fig. 2.3 and Fig. 2.4 (middle) where the pulse duration is much shorter than τ_{rot}. In this case before the system has enough time to return to its initial state, the pulse vanishes and leaves the molecule in a superposition of rotational states. Later, these states evolve freely and beat just like a superposition of sinusoidal functions with different frequencies.

$\langle\langle \cos^2 \theta_{x,y,z} \rangle\rangle$ is a measure that quantifies how the molecule aligns with respect to space-fixed frame. Fig. 2.4 shows the evolution of this parameter calculated with

the values up to $J = 20$. It is obvious that in the adiabatic case the θ_x of molecule decreases, in other words molecule's axis of symmetry aligns along the electric field axis, as the pulse rises. Maximum alignment occurs at the peaks of pulse and then drops to its initial value as the pulse declines. Effect of nonzero values of coefficients after the pulse turn-off, Fig. 2.3 (middle), on the $\langle\langle\cos^2\theta_x\rangle\rangle$ appears like a beating signal Fig. 2.4 (middle). The angle of molecule with x-axis oscillates with τ_{rot} time scale (≈ 8.3 ps for N_2).

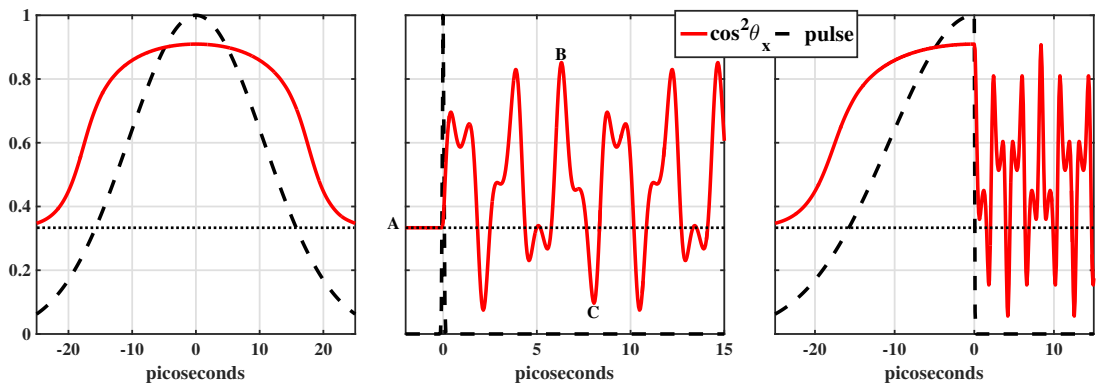

Figure 2.4: Dynamics of $\langle\langle\cos^2\theta_x\rangle\rangle$ (red) with same conditions as in Fig. 2.3. (left) [$\tau_{\text{on}} = 25$ ps, $\tau_{\text{off}} = 25$ ps], (middle) [$\tau_{\text{on}} = 100$ fs, $\tau_{\text{off}} = 100$ fs] and (right) [$\tau_{\text{on}} = 25$ ps, $\tau_{\text{off}} = 100$ fs]. Normalized pulse shape is shown with black dashed line and for comparison value of $\langle\langle\cos^2\theta_x\rangle\rangle = 1/3$ is shown with black dotted line.

Value of $\sqrt{\langle\langle J(J+1)\rangle\rangle}$ is shown in Fig. 2.5 with blue dashed line. It shows that in case of nonadiabatic alignment that molecule is left in $J > 0$ states contrary to the adiabatic alignment that angular momentum is zero.

Right panel of figures 2.3, 2.4 and 2.5 show the case that $\tau_{\text{on}} = 25$ ps (adiabatic turn-on) and $\tau_{\text{on}} = 100$ fs (nonadiabatic turn-off). This case inherits the properties of adiabatic and nonadiabatic cases. The most striking differences of this with nonadiabatic interaction is that the value of $\sqrt{\langle\langle J(J+1)\rangle\rangle}$ is higher, i.e. more rotational states contribute to the dynamics of the molecule. As a result the beating between these states which is observable in $\langle\langle\cos^2\theta_x\rangle\rangle$ quantity results in sharper features for

Fig. 2.4 (right). In other words, broader wavepacket in J space is equivalent of sharper alignment peaks. For this hybrid type of interaction, simulations show that the vertical separation between peaks and dips of $\langle\langle\cos^2\theta_x\rangle\rangle$ are more pronounced. The angular distribution of molecules for T=0°K is shown in Fig. 2.6 before interac-

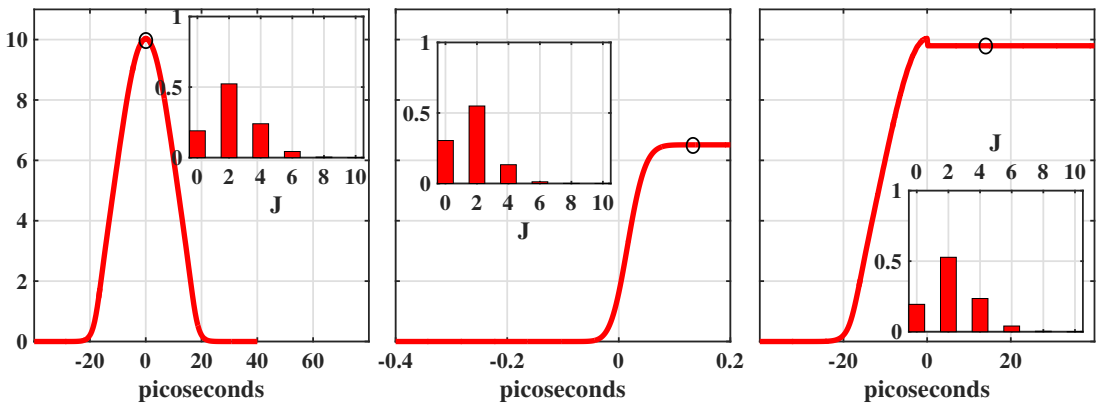

Figure 2.5: Dynamics of $\sqrt{\langle\langle J(J+1)\rangle\rangle}$ with same conditions as in Fig. 2.3. (left) [$\tau_{\rm on}$ = 25 ps, $\tau_{\rm off}$ = 25 ps], (middle) [$\tau_{\rm on}$ = 100 fs, $\tau_{\rm off}$ = 100 fs] and (right) [$\tau_{\rm on}$ = 25 ps, $\tau_{\rm off}$ = 100 fs]. Insets show the populations of rotational states at the encircled positions of each main panel.

tion with the laser pulse (left panel), at the increase of $\langle\langle\cos^2\theta_x\rangle\rangle$ (middle panel) and decrease of $\langle\langle\cos^2\theta_x\rangle\rangle$ (right) instances.

We will discuss more properties of nonadiabatic alignment hereafter. Numerical results of Eq. 2.32 are shown in Fig. 2.7 for nitrogen, oxygen and air molecules ensemble at T=295°K interacting with a linear pulse. Air is assumed to consist of 78% nitrogen and 22% oxygen. The pulse has a Gaussian temporal shape with full-width at half-maximum of 60 femtosecond and peak intensity is 50 TW/cm^2. Higher temperature requires more rotational states to be considered in Eq. 2.32 according to Eq. 2.12. As we mentioned previously, a broader wavepacket in rotational space brings sharper alignments with less features. Similar to Fig. 2.4 (middle), after the pulse declines the molecular wavepacket beats at multiples of the rotational frequency. After integral multiples of $\tau_{\rm rot}$, "full-revival", the molecule's axis of sym-

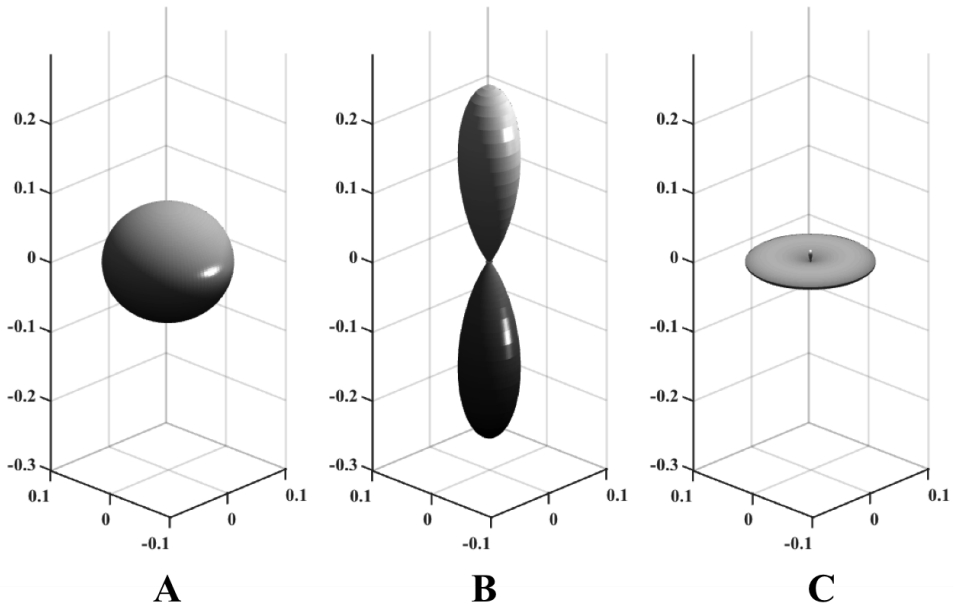

Figure 2.6: Angular distribution of N_2 molecule at T=0°K corresponding to the middle panel of Fig. 2.4. (A) In the absence of the aligning pulse (point A in Fig. 2.4), (B) in the alignment instance near the full-revival (point B in Fig. 2.4) and (C) anti-alignment near the full-revival (point C in Fig. 2.4).

metry makes the same angle with electric field. Weaker alignments are formed at integral multiples of $\tau_{\rm rot}/4$, "quarter-revival" and $\tau_{\rm rot}/2$, "half-revival".

"Half-revival"s are combinations of a peak and a trough in $\langle\langle\cos^2\theta_x\rangle\rangle$. The maxima represent alignment of molecules in direction of laser polarization i.e. the angle between the laser polarization and the molecular axis is reduced while the minima show the antialignment of molecules i.e. the angle between the laser polarization and the molecular axis is increased. Fig. 2.7 shows that the transition from alignment to antialignment and vice versa is very fast compared to the rotational period. $\langle\langle\cos^2\theta_x\rangle\rangle$ starts from 1/3 before the pulse arrives and shortly after peak of the pulse rises towards a maximum. 1/3 value can be justified by the fact that addition of

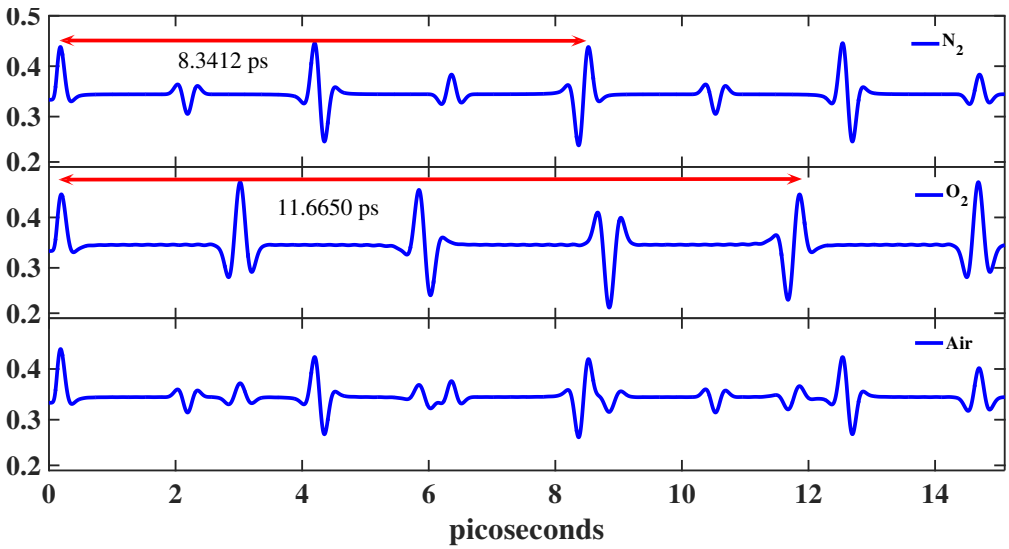

Figure 2.7: $\langle\langle \cos^2\theta_x \rangle\rangle$ as a function of time for nitrogen (top), oxygen (middle) and air (bottom) molecules at 295°K interacting with a linearly polarized pulse of 60 fs duration and 50 TW energy.

cosine of polar angles with respect to space-fixed axes is

$$\cos^2\theta_x + \cos^2\theta_y + \cos^2\theta_z = 1 \tag{2.35}$$

and for a randomly aligned ensemble of molecules we expect that the average of all angles to be equal, hence, $\cos^2\theta_x = \cos^2\theta_y = \cos^2\theta_z = 1/3$. Values of $\langle\langle \cos^2\theta_x \rangle\rangle$ after the pulse show an "alignment enhancement" i.e. linear molecules after interaction with a linearly polarized pulse do not return to their 1/3 value but maintain some degree of alignment that depends on the energy of pulse. We will discuss this enhancement in the next sections.

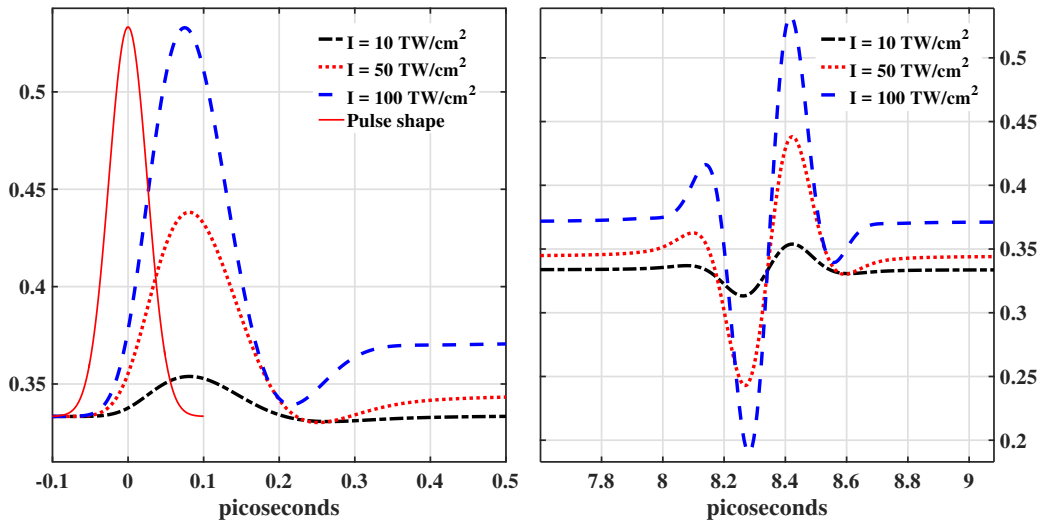

(a) (b)

Figure 2.8: Time evolution of $\langle\langle \cos^2\theta_x \rangle\rangle$ of nitrogen molecules for different optical pulse energies. All the pulses have the same pulse duration of 60 fs and are linearly polarized. Molecules are at 295°K. (a) Near the pulse, (b) at the first full-revival.

2.5 Effects of pulse energy and duration on alignment

Numerical calculation of Eq. 2.32 is performed for different pulse energies. Note that at high the intensities considered in Fig. 2.32 ionization rate of nitrogen molecules is high, however, we only consider the molecular alignment. Fig. 2.8a (left) shows evolution of $\langle\langle \cos^2\theta_x \rangle\rangle$ close to the existence of pulse. This shows that for the same pulse duration the one with the higher energy creates sharper alignment of molecules. The same order of evolution happens near the revivals; the pulse with higher energy creates a larger modulation and magnitude of $\langle\langle \cos^2\theta_x \rangle\rangle$. Fig. 2.8b shows this fact near the first full-revival of nitrogen.

On the other hand we examine the dependence of molecular alignment on the pulse temporal duration. Fig. 2.9a shows the temporal evolution of molecular align-

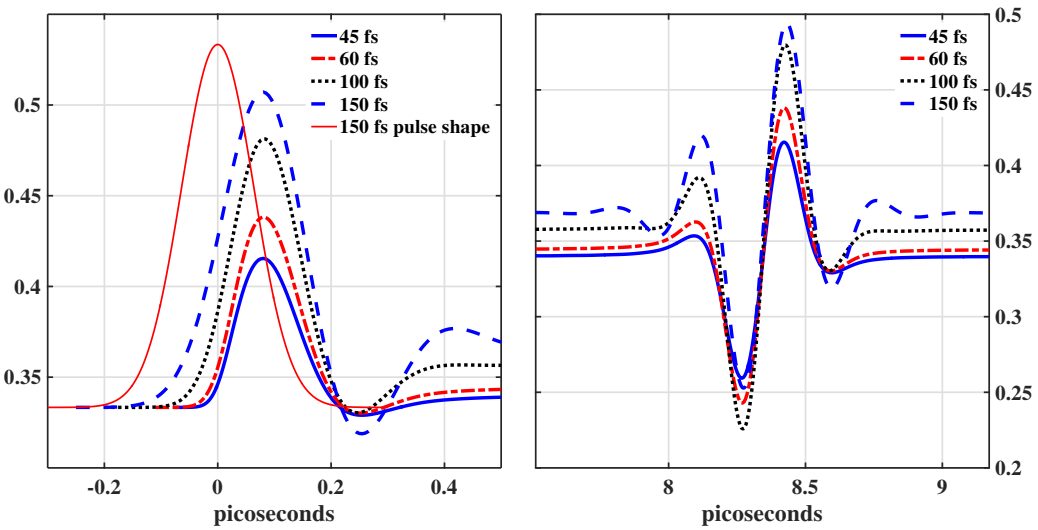

(a) (b)

Figure 2.9: Time evolution of $\langle\langle \cos^2\theta_x \rangle\rangle$ of nitrogen molecules for different optical pulse durations at the vicinity of pulse (a) and around the first full-revival. All the pulses have the same intensity equal to 50 TW/cm^2 and are linearly polarized. Molecules are at 295°K. The longest pulse in this simulation is shown for comparison.

ment of nitrogen molecules as a function of time for pulses with same energy but different durations. This shows that in the nonadiabatic regime a shorter pulse creates a less aligned ensemble of molecules. One can see that the DC part of $\langle\langle \cos^2\theta_x \rangle\rangle$, after the pulse vanishes, is larger for the longer pulse, i.e. pulse leaves the molecules in a smaller angle with respect to the polarization axis or creates "alignment enhancement". Fig. 2.9b shows the behavior of molecules at the first full-revival. Here we see the same behavior of molecules as in the vicinity of pulse.

Effect of pulse duration on the alignment is explained by the fact that longer pulse allows the molecule to reach higher rotational states, so a broader wavepacket is created in rotational space. Sharper alignment peaks and dips appear for a longer pulse because more J states are adding up. Improved "alignment enhancement" for longer pulses is due to the amount of $BJ(J+1)$ for larger J values in Eq. 2.26 which signifies the effect of higher "J"s in wavepacket.

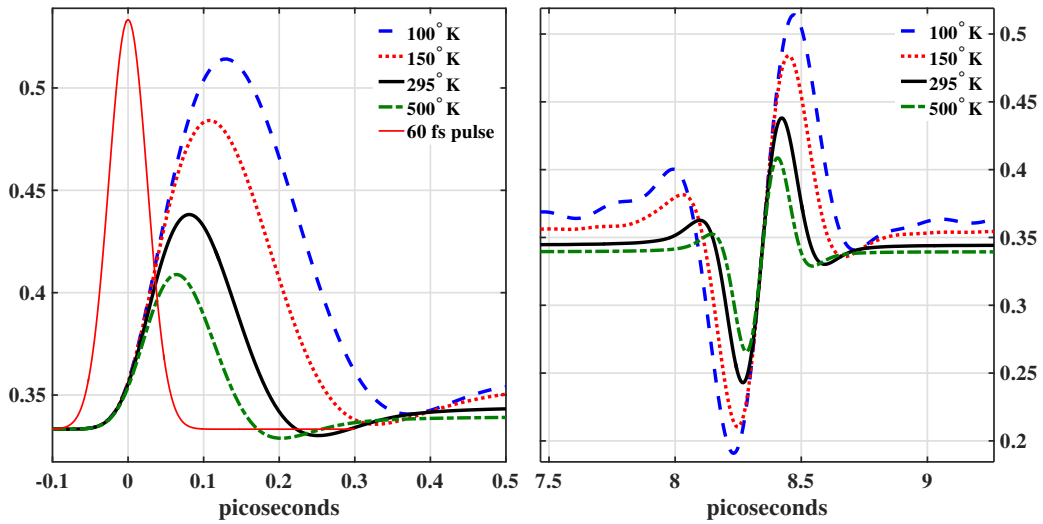

(a) (b)

Figure 2.10: Time evolution of $\langle\langle \cos^2\theta_x \rangle\rangle$ of nitrogen molecules that interact with a linear pulse of 60 fs duration and 50 TW/m^2 at different temperatures. (a) Close to the pulse where the prompt response occurs and (b) at the first full-revival

2.6 Effect of temperature on alignment

From the Boltzmann distribution one finds that in higher temperatures larger Js are occupied, initially. According to Eq. 2.32, hence, more rotational states add up to create the molecular alignment as their weight is significantly changed compared to T=0°K. The relative phases of different rotational states cancel out more when larger number of Js are involved and weaker alignment is created, consequently. Fig. 2.10a and Fig. 2.10b show $\langle\langle \cos^2\theta_x \rangle\rangle$ as a function of time for nitrogen molecules at different temperatures near the pulse and close to the first full-revival. This shows that the molecular ensemble at higher temperature is less aligned in the direction of pulse polarization axis and transition from alignment to antialignment takes a longer time at higher temperature.

"Alignment enhancement" is observed in this case as well. At the lower temper-

atures the DC part of $\langle\langle \cos^2\theta_x \rangle\rangle$ is larger. This means that the molecules in lower temperature are more aligned in the direction of laser polarization after interaction with a linearly polarized pulse.

2.7 Fourier transform and $\langle\langle \mathbf{J}^2 \rangle\rangle$

We showed that the initial energy distribution of molecular ensemble with rotational motion is defined by Boltzmann ensemble. At T=295°K nitrogen molecules are mostly probable to be found in J=6 (Fig. 2.2). However after the interaction with the pulse, energy distribution is changed and it is more likely to find the molecules in higher "J"s. Fig. 2.11 (left) compares the J distribution before and after the ensemble of nitrogen molecules at T=295°K interacts with a short pulse of 60 fs duration and intensity of 50 TW/cm^2. It is shown that after interaction $J = 8$ is most likely to be occupied by the nitrogen molecules.

However the oxygen molecules that initially occupy $J = 7$ after interaction are more probable to be found in $J = 11$. Larger value of $\Delta\alpha$ (cf. Table 2.1) which causes more efficient coupling between field and molecule, and smaller amount of B for O_2 which implies that the energy spacing between rotational states are smaller, make bigger shift in J value compared to N_2. Right plot in Fig. **??** shows the evolution of $\sqrt{\langle\langle J(J+1) \rangle\rangle} \approx \langle\langle J \rangle\rangle$ as a function of time during the interaction with a 60 fs pulse with three different energies. This shows that higher pulse energy transfers the molecules to higher J states as was discussed before.

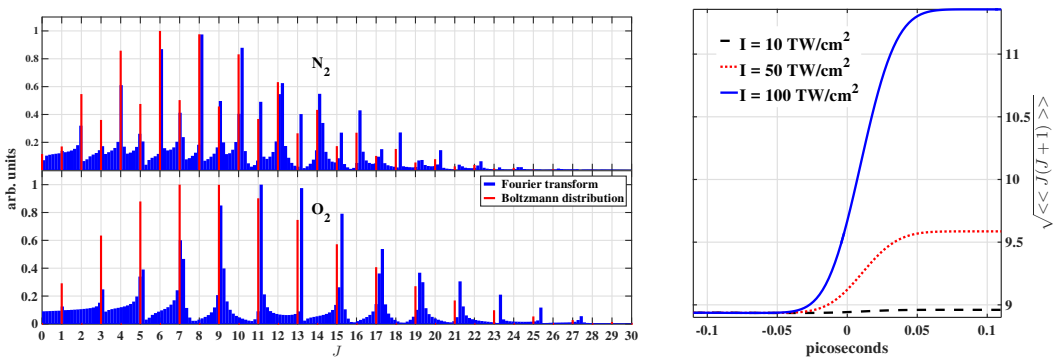

(a) (b)

Figure 2.11: Comparison of J distribution of N_2 (left top) and O_2 (left bottom), before and after interaction with a short pulse of 60 fs duration and intensity of 50 TW/cm^2 at T=295°K. Value of $\sqrt{\langle\langle J(J+1)\rangle\rangle}$ of nitrogen molecules at 295°K as a function of time for three different pulse energies with same duration of 60 fs (right).

2.8 Linear molecules interacting with arbitrarily polarized electric field

We derived the Hamiltonian of elliptically polarized electric field interacting with a symmetric-top molecule in Eq. 2.25. Depending on the choice of η in Eq. 2.15 and its sign one can select the polarization ellipticity and helicity of the electric field.

Hence the time-dependent Schrödinger equation is the same as Eq. 2.26 except for the second term on the right-hand-side. The final form is

$$i\hbar\frac{\partial|\Psi(\theta,t)\rangle}{\partial t} = \Big[2\pi\hbar J(J+1)B - \frac{2\pi\Delta\alpha_\nu I_0}{c}|\tilde{\mathcal{E}}(t)|^2\Big[(|e_x|^2-|e_y|^2)\cos^2\theta_x + |e_y|^2\sin^2\theta_z\Big]\Big]|\Psi(\theta,t)\rangle \tag{2.36}$$

where θ_x and θ_z are the polar angle with respect to x-axis and z-axis, respectively.

Introducing Eq. 2.11 into Eq. 2.36 we have

$$\begin{aligned}\dot{a}_{JM} = &-2i\pi c\Big\{ J(J+1)B\ a_{JM} \\ &- \frac{\Delta\alpha_\nu I_0}{\hbar c^2}|\tilde{\mathcal{E}}(t)|^2\Big[\sum_{J,J'}\sum_{M,M'} a_{JM}a^*_{J'M'}(|e_x|^2-|e_y|^2)\langle J',M'|\cos^2\theta_x|J,M\rangle \\ &+\sum_{J,J'}\sum_{M,M'} a_{JM}a^*_{J'M'}|e_y|^2\langle J',M'|\sin^2\theta_z|J,M\rangle\Big]\Big\} \end{aligned} \tag{2.37}$$

The matrix elements of $\langle\cos^2\theta_x\rangle$ are derived analytically as [54]

$$\begin{aligned}\langle J',M'|\cos^2\theta_x|J,M\rangle = &\ \delta_{M',M}\{A^J_M\delta_{J',J}+B^{J'}_M\delta_{J',J+2}+B^J_M\delta_{J',J-2}\}+ \\ &\delta_{M',M+2}\{C^J_M\delta_{J',J}+D^J_M\delta_{J',J+2}+D^{J'}_{-M'}\delta_{J',J-2}\}+ \\ &\delta_{M',M-2}\{C^J_{M'}\delta_{J',J}+D^J_{-M}\delta_{J',J+2}+D^{J'}_{M'}\delta_{J',J-2}\}. \end{aligned} \tag{2.38}$$

Matrix elements of $\langle\sin^2\theta_z\rangle$ could be calculated from Eq. B.5 from the relation of cosine and sine functions. From these one finds that the transitions occur between the rotational states with $\Delta J = 0, \pm 2$ and $\Delta \mathrm{M} = 0, \pm 2$. Then for circular polarization as a special shape of elliptical polarization where $e_x = e_y$, $\Delta J = 0, \pm 2$ and $\Delta \mathrm{M} = 0$. Comparing Eq. 2.38 with Eq. B.5 one concludes that with elliptical polarization the projection of total angular momentum along z-axis is not conserved contrary to linear and circular polarization.

Fig. 2.12 shows the results of numerical simulations of Eq. 2.37 for linearly and circularly polarized lights interacting with nitrogen molecules at T=30°K. Intensity of circularly polarized laser is twice the intensity of linearly polarized laser. We chose this ratio in order to make the second term of the Hamiltonian in Eq. 2.36 equal for both linear and circular polarizations. This shows that soon after interacting with the *linearly* polarized field, the angle of molecular axis is smaller to the x-axis (note that in Eq. 2.15 $\eta = 0$); molecules are aligned mainly around the axis of polarization. In this case θ_z and θ_y have the same temporal evolutions.

However, in the case of *circularly* polarized field (in Eq. 2.15 $\eta = \pi/4$) molecular axis is mainly aligned in the xy plane i.e. the plane of polarization. In this case

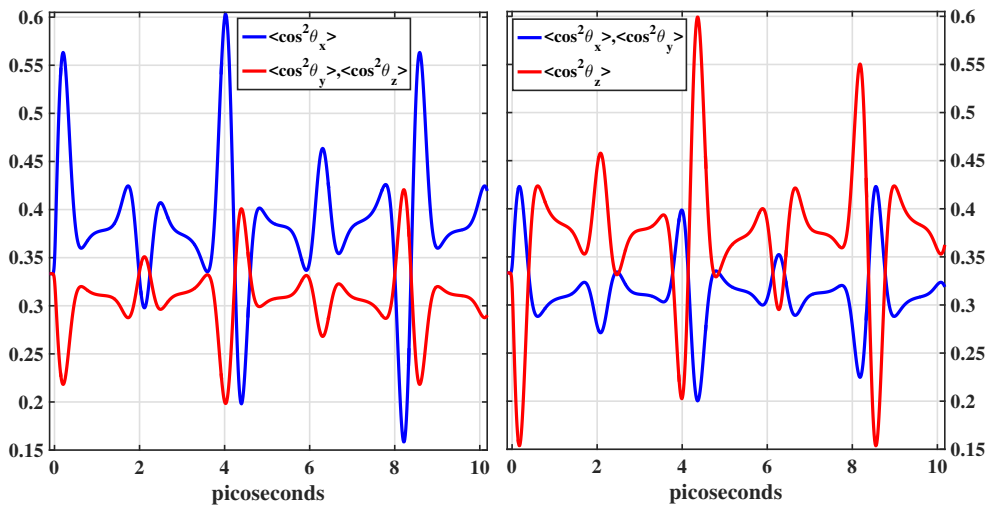

Figure 2.12: Variations of nitrogen alignment as a function of time for (left) linearly polarized light pump with intensity of 50 TW/cm^2($\eta = 0$) and (right) circularly polarized ($\eta = \pi/4$) pump with intensity of 100 TW/cm^2. Duration of the pump is the same for both the polarizations and is equal to 45 fs duration. Molecular ensemble is at T=30°K.

the θ_x and θ_y behave the same over the time. In the case of alignment with circular polarization one can define alignment (anti-alignment) as the smaller (larger) angle of molecular axis with respect to polarization plane. This scale is defined with respect to polarization axis in the case of linearly polarized field. Taller peaks, or in other words more effective modulation of alignment, in the case of linear polarization is because of smaller effective intensity for circular polarization i.e. in Eq. 2.36 we have $e_x = e_y = 1/\sqrt{2}$ for circular polarization, so effective intensity is half the intensity of linear field.

Effect of ellipticity of the field is shown in Fig. 2.13 for different values of the angle between the axis of quarter-wave plate (QWP) and a laser field in x direction. All the properties of the laser field are the same for all the lines except the ellipticity. As we discussed before the effective intensity of the laser decreases with increasing η, consequently, the modulation depth of alignment degrades.

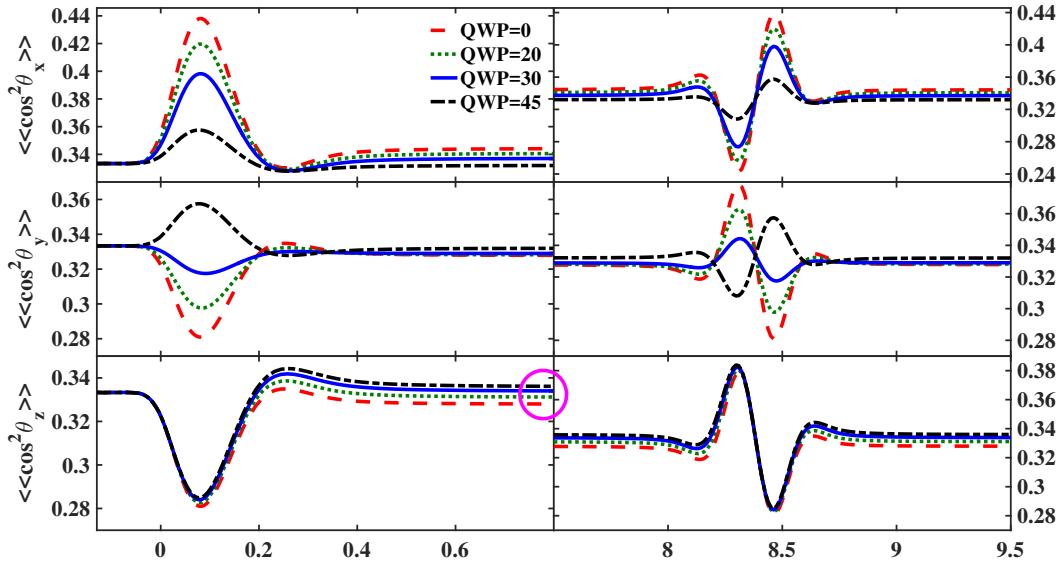

Figure 2.13: Scales of alignment, $\langle\langle\cos^2\theta_x\rangle\rangle$, $\langle\langle\cos^2\theta_y\rangle\rangle$ and $\langle\langle\cos^2\theta_z\rangle\rangle$, of nitrogen molecules at T=295°K at the zero-delay region (left column) and around full-revival (right column). We assume a quarter-wave plate (QWP) modulates the polarization of a linear field that lies in x-direction. Different QWP angles are shown. Molecules interact with 50 TW/cm^2 and 60 fs duration field. The abscissa is in picosecond.

Left column of Fig. 2.13 depicts the alignment variations near the pulse. For the linear case, as we expect the molecular ensemble makes a better alignment with the x-axis i.e. the field direction. At the full-revival moment, right column of Fig. 2.13, molecules rotate through a fast passage from being perpendicular to the field to parallel to the field. For circular polarization molecules make smaller angle with the xy plane while their polar angles with each of the x or y axes are the same. Passage from anti-alignment to alignment at full-revival is transition a from out of xy plane towards inside of this plane. Rotational dynamics of molecules for $0 < \eta < 1$ is similar to linear polarization. However, to fully illustrate the spatial alignment of molecules one needs to define the Euler angles (ϕ, θ, ψ) (cf. Fig. A.1). It is shown [55] that for linear and circular polarizations one only can control the ψ and θ angles while the distribution of ϕ angle over $[0, \pi]$ is a flat line. This implies that the molecules after interaction with laser field rotate around the linear polarization axis (here we assume

that it is in x direction) or inside the plane of polarization (xy plane). Contrary to linear and circular polarizations, for the case of elliptically polarized field one can control the alignment over al the Euler angles.

Note that the encircled part of Fig. 2.13 emphasizes on the difference between the "alignment enhancement" of various polarizations. After the pulse induces the rotational wavepacket impulsively, the alignment of linear molecule along the z-axis is more efficient for the circularly polarized laser i.e. molecule leans away from the polarization plane.

2.9 Effect of molecular rotations on the refractive index of gaseous medium

The refractive index of a medium is a function of polarizability of its constituents,

$$n^2 = 1 + N\langle\langle\alpha\rangle\rangle \tag{2.39}$$

where N is the density of molecules and $\langle\langle\alpha\rangle\rangle$ is the expectation value of second-order tensor of polarizability. Eq. 2.20 marks out the relation between the polarizability tensors in body and space-fixed frames as

$$\alpha_{\rho\rho'} = \sum_{kk'} \langle\rho|k\rangle \alpha_{kk'} \langle k'|\rho'\rangle \tag{2.40}$$

For the linear molecules ($\alpha_{XX} = \alpha_{YY} = \alpha_\perp$, $\alpha_{ZZ} = \alpha_\parallel$ and $\Delta\alpha = \alpha_\parallel - \alpha_\perp$) aligned by linearly polarized laser ($\hat{\mathcal{E}} = \hat{k}$) Eq. 2.39 is reduced to

$$\begin{aligned} n^2_{\text{par}} &= 1 + N\langle\langle\alpha_{zz}\rangle\rangle \\ &= 1 + N\langle\langle\sin^2\theta\ \alpha_\perp + \cos^2\theta\ \alpha_\parallel\rangle\rangle \\ &= 1 + N\Big[\Delta\alpha\ \langle\langle\cos^2\theta\rangle\rangle + \alpha_\perp\Big] \end{aligned} \tag{2.41}$$

for the refractive index parallel to the electric field i.e. along the x-axis and

$$\begin{aligned} n_{\text{perp}}^2 &= 1 + N\langle\langle \alpha_{xx} \rangle\rangle \\ &= 1 + N\Big\langle\Big\langle \Big(\sin^2\varphi + \cos^2\theta\cos^2\varphi\Big)\alpha_\perp + \Big(\sin^2\theta\cos^2\varphi\Big)\alpha_\parallel \Big\rangle\Big\rangle \\ &= 1 + N\Big[\frac{\Delta\alpha}{2}\left(1 - \langle\langle\cos^2\theta\rangle\rangle\right) + \alpha_\perp\Big] \end{aligned} \tag{2.42}$$

for the refractive index perpendicular to the electric field polarization direction. We note that $\sin^2\theta\cos^2\varphi = \cos^2\theta_x$ and $\cos^2\theta_x + \cos^2\theta_y + \cos^2\theta_z = 1$ and $\cos^2\theta_x = \cos^2\theta_y$ (for this specific case) with $\theta_{x,y,z}$ the polar angles with respect to x, y and z axes, respectively. Here we have $\theta_z = \theta$ for brevity.

The refractive index of randomly aligned molecules is then

$$n_0^2 = 1 + N\Big[\frac{\Delta\alpha}{3} + \alpha_\perp\Big] \tag{2.43}$$

as we shown that the average value of $\langle\langle\cos^2\theta\rangle\rangle$ for randomly aligned ensemble is $1/3$. Hence, by applying the approximation that $n^2 - n_0^2 = (n - n_0)(n + n_0) \approx 2n_0\Delta n$, the change in refractive index because of alignment of molecules is

$$\Delta n_{\text{par}} = \frac{N\Delta\alpha}{2n_0}\Big[\langle\langle\cos^2\theta\rangle\rangle - \frac{1}{3}\Big] \tag{2.44}$$

$$\Delta n_{\text{perp}} = -\frac{N\Delta\alpha}{4n_0}\Big[\langle\langle\cos^2\theta\rangle\rangle - \frac{1}{3}\Big] \tag{2.45}$$

Negative sign of Eq. 2.45 implies that by increase in $\langle\langle\cos^2\theta\rangle\rangle$ i.e. alignment of molecules along the polarization axis, refractive index in normal plane to the polarization of the pump decreases. From this equation we also conclude that the magnitude of refractive index modulations in normal plane is half compared to change of refractive index parallel to the polarization of the pump. For the general case of

elliptically polarized beam, with the xy plane as the polarization plane, refractive index is

$$\begin{aligned} n^2 &= 1 + N\Big(a^2 \ \langle\langle \alpha_{xx} \rangle\rangle + b^2 \ \langle\langle \alpha_{yy} \rangle\rangle\Big) \\ &= 1 + N\Delta\alpha\Big[a^2 \ \langle\langle \cos^2\theta_x \rangle\rangle + b^2 \ \langle\langle \cos^2\theta_y \rangle\rangle\Big] + \alpha_\perp \end{aligned} \tag{2.46}$$

so the change in refractive index is

$$\Delta n = \frac{N\Delta\alpha}{2n_0}\Big[a^2 \ \langle\langle \cos^2\theta_x \rangle\rangle + b^2 \ \langle\langle \cos^2\theta_y \rangle\rangle\Big] \tag{2.47}$$

Equations 2.44 and 2.45 show that gaseous media whose molecules are aligned by a linearly polarized pulse (pump) become birefringent or in other words are not isotropic any longer. If a second linearly polarized pulse (probe) passes through the wake of the pump, the refractive index that it experiences depends on whether its polarization is parallel or perpendicular to the polarization of the pump. For the general case where the probe is elliptically polarized, the major and minor axis of polarization will rotate if they initially have a nonzero angle with polarization axes of the pump.

From fundamentals of optics we know that change of the refractive index varies the wavelength of the electromagnetic wave. A pulse with central wavelength of λ_0 that propagates through a length of L acquires a wavelength shift as

$$\Delta\lambda = \frac{L\lambda_0}{c}\frac{d}{dt}\Delta n \tag{2.48}$$

with c the vacuum speed of light.

2.10 Pump-probe experiment to investigate the rotational motion of molecules

In order to observe the effect of molecular rotational motion a variety of techniques have been used, some of them based on the photodissociation and ionization of molecules that are pre-aligned by a laser pulse (for a review see [34]). The aforementioned changes of refractive index suggest a straightforward method to investigate the molecular rotations. Variations of refractive index affect the beam shape and spectrum of a pulse that travels through the wake of an aligning pulse. A pump-probe experiment could be used to record the modulations of spectra and beam shapes of the probe pulse as a function of its delay with respect to the pump.

In Fig. 2.14 we study the rotations of nitrogen molecules at the room temperature by aligning them with a pump; an 800 nm laser pulse with 60 fs duration and its energy close to 1 mJ inside the gas cell. The nitrogen gas pressure is 15 psi. A probe pulse is generated by letting 10% of the initial 800 nm pulse pass through a 1 mm thick LBO crystal. The energy of the 400 nm pulse is less than 10 μJ and it traverses a delay line at the end of which it is spatially combined with the 800 nm. The pump is focused by a lens with a focal length of 1 m while the probe passes a lens with focal length of 50 cm. The focal spot of probe is deliberately chosen to overlap with the pump focal spot, longitudinally and transversely. The delay line is equipped with the Physik Instrumente's translation stage which is set to move in 10 fs increments. After being combined with the pump inside the gas cell, the probe is separated from the pump by a short-pass filter and is focused by a 10 cm biconvex lens into the optical fiber of an Ocean Optics' spectrometer. We also monitor the beam shape of the probe pulse by a CCD camera placed after the short-pass filter. There are half-wave-plates (HWP) and quarter-wave-plates (QWP) to control the polarizations of the either of pump or probe beams. Here only the case of parallel

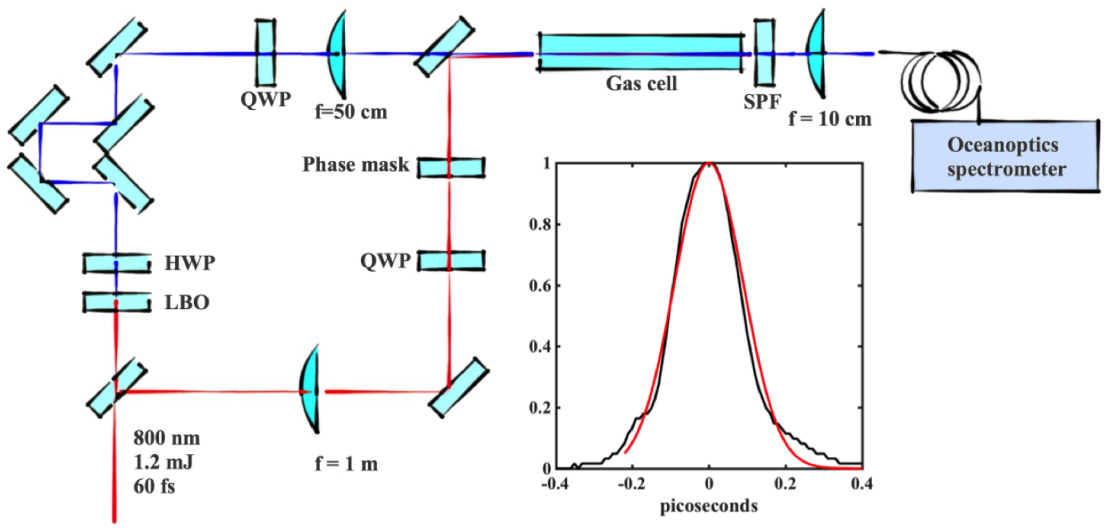

Figure 2.14: Pump-probe setup for rotational alignment investigation. 800 nm pulse with 60 fs duration acts as aligning pulse (pump) and its second harmonic probes the modulations of refractive index. Probe's spectra are recorded by a spectrometer and its beam profile is captured by a CCD camera. Plot shows the sum-frequency signal of the pump and probe as function of their delay (black), generated by a type-I KDP crystal and a cross-correlation fit (red).

polarizations of the linearly polarized pump and probe is considered (cf. Eq. 2.44). Circularly polarized pump and probe are combined as well. Temporally, the probe pulse follows the pump and we call this positive delay. Obviously for a negative delay, when the pump is following the probe, we do not expect any changes to the spectrum or the beam shape of the probe and our observations confirm this. Zero delay is found by placing a 1 mm type-I KDP crystal to capture the sum-frequency signal generated by overlap of pump and probe. This signal is captured as function of delay between the two pulses and is shown in Fig. 2.14. We fit a line calculated by cross-correlation of two gaussians with 150 fs durations. This is shown by red line in Fig. 2.14.

As mentioned before, changes in refractive index affect both beam profile and the

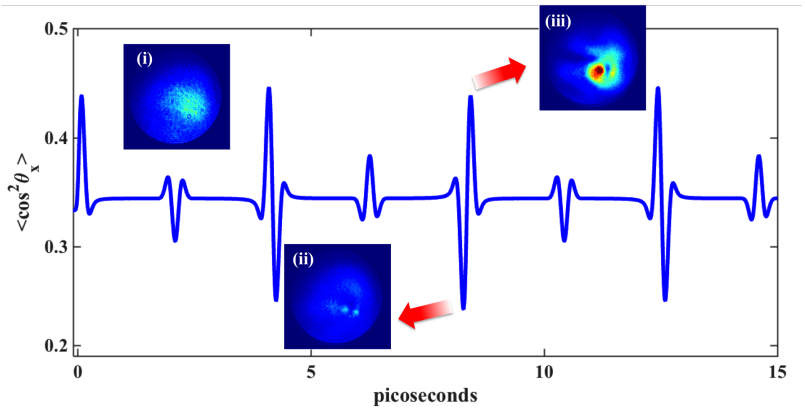

Figure 2.15: Main plot shows the evolution of $\langle\langle \cos^2 \theta_x \rangle\rangle$ as function of time for nitrogen in room temperature. Probe's beam profiles from the setup in Fig. 2.14 are shown at different instances of delay in the main panel. (i) Beam profile at absence of the pump (ii) at the antialignment instance of full-revival and (iii) at the alignment instance of full-revival.

spectrum of any pulse that travels in the trail of the pump. Fig. 2.15 (i), (ii) and (iii) compare the beam shape of the probe when the pump is blocked with its beam

Figure 2.16: Spectra as a function of delay between the pump and probe. Here pump and probe polarizations are parallel. Inset shows the probe's spectrum at the absence of the pump.

shape at a delay equal to the first full revival of nitrogen; 8.3 ps. It is shown that the fall of $\langle\langle \cos^2\theta_x \rangle\rangle$ at around 8.3 ps (full-revival) shows antialignment of nitrogen molecules (cf. right panel in Fig. 2.6) which causes the refractive index to drop from its initial value, n_0, according to Eq. 2.44. This is shown in the Fig. 2.15 (ii) where the beam profile is less intense on the CCD due to the defocusing. However, alignment instance follows anti-alignment in less than 200 femtoseconds. This causes increase in refractive index and changes the refractive index to a larger magnitude than n_0 which contracts the beam to focus. This is shown in Fig. 2.15 (iii) where the intensity profile is stronger compared to the original intensity distribution. Later we will discuss the observation of transverse spatial modulation of the probe with another method.

Fig. 2.16 depicts the spectra modulations of probe pulse as a function of its delay with the pump. The instances of changes in wavelength match the rotational revivals of nitrogen and blue-shift or red-shift happen depending on the alignment or anti-alignment of molecules. Although the same phenomena are observed around all the revival instances, the strengths of modulations of the beam profile are weaker near the odd multiples of quarter-revival.

Further information could be inferred by calculating the wavelength center-of-spectrum (CS) of the probe

$$\lambda_{\mathrm{CS}} = \frac{\int_{\lambda_1}^{\lambda_2} \lambda\ A(\lambda)\ d\lambda}{\int_{\lambda_1}^{\lambda_2} A(\lambda)\ d\lambda} \tag{2.49}$$

with $A(\lambda)$ the amplitude of each wavelength in the spectra. Differential CS is defined as

$$\Delta\lambda_{\mathrm{CS}} = \lambda_{\mathrm{CS}} - \lambda^0_{\mathrm{CS}} \tag{2.50}$$

where λ^0_{CS} represents the center wavelength of the probe when the pump is blocked. $\Delta\lambda_{\mathrm{CS}}$ of spectra of Fig. 2.16 at each delay point i.e. at each point of abscissa are

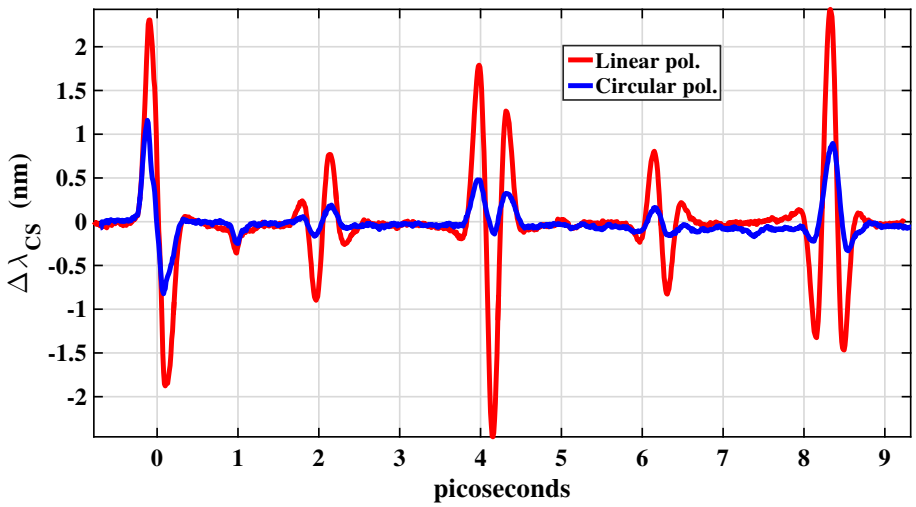

Figure 2.17: Temporal modulations of $\Delta\lambda_{\mathrm{CS}}$ of the probe pulse.

shown in Fig. 2.17 for linearly polarized pump and probe and circularly polarized pump and probe. Maximum wavelength shift of more than 2 nm is obvious at blue-side and red-side of the λ^0_{CS} at the half-revival and full-revival instances for linear polarization. For circularly polarized pump and probe the CS deviation from λ_0 is smaller compared to the linear polarization case. Odd multiples of quarter-revivals impose less intense wavelength shift on the probe compared to the even multiples.

Fig. 2.18 is the Fourier transform of Fig. 2.17 as a function of angular momentum quantum number J. We believe that the pump impulsively excites the rotational states of nitrogen and the incoming probe pulse goes through a series of Raman-type transitions between the the states with energy spacings of $B(4J + 6)$. From Fig. 2.18 this assumption is verified. It is obvious that the even J values have stronger amplitudes than the odd ones. This is compatible with Table 2.1 values of N_2 where the thermal population of even rotational levels are higher than the odd levels. We also observe that the maximum value of J is equal to 8 which matches with Fig. 2.2.

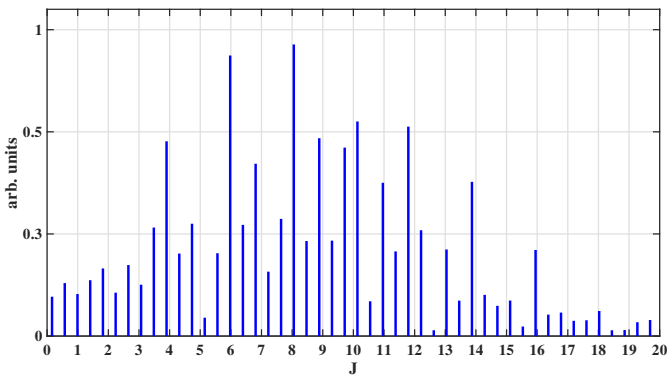

Figure 2.18: Fourier transform of linear polarization (red line) in Fig. 2.17

At the zero delay region, where the pump and probe temporally overlap, the rotational effect is not the only reason of bandwidth broadening, however, instantaneous Kerr effect imposes modulations on the probe spectra i.e. when the pump and probe pulses are overlapping, intensity of the pump is high enough to induce cross-phase modulation on the weaker probe pulse [2]. The effect of a generated plasma channel on the refractive index is ignored in our calculations. We assume that the probe's intensity is very weak to go through self-phase modulation. Hence, in order to extract the rotational share of wavelength modulations we filled the gas chamber by argon gas and repeated the pump-probe experiment. Argon is atomic gas and does not carry any rotational or vibrational degrees of freedom.

The phase shift of the probe propagating along the pump for the length z is

$$\phi(t) = 2\pi \; n_2 \; I_{\text{pump}}(t) \; \frac{z}{\lambda_{\text{probe}}} \tag{2.51}$$

where I_{pump}, λ_{probe} and n_2 are the pump intensity, wavelength of the probe and nonlinear refractive index in units of m^2/W, respectively. Temporal evolution of wavelength can be calculated by taking the time derivative of $\phi(t)$.

Alignment revivals of the molecules extend the refractive index modulations beyond the instance of pulse existence. For a weak probe, that propagates in the wake

of strong pump, the propagation equation under the slowly-varying amplitude is

$$\frac{\partial}{\partial z}(\tilde{\mathcal{E}}_x\hat{x}+\tilde{\mathcal{E}}_y\hat{y}) = -i\frac{\mu_0\omega c}{2n}(\tilde{\mathcal{P}}_x\ \hat{x}+\tilde{\mathcal{P}}_y\ \hat{y}), \tag{2.52}$$

where electric field is defined in Eq. 2.13 and polarization of medium is $P = \frac{1}{2}(\tilde{\mathcal{P}}_x\ \hat{x}+\tilde{\mathcal{P}}_y\ \hat{y})\exp[i(\omega t - kz)]$. Polarization along any of the space-fixed axes is related to the polarizability of molecules through [2]

$$\tilde{\mathcal{P}}_i = \epsilon_0 N \sum_j \langle\langle \alpha_{ij} \rangle\rangle\ \tilde{\mathcal{E}}_j\ . \tag{2.53}$$

where N is the molecular density, $\langle\langle\alpha\rangle\rangle$ is the averaged polarizability tensor and $\tilde{\mathcal{E}}$ is the electric field. We already assumed that the polarization plane lies in xy-plane, hence, the required elements of polarizability tensor in Eq. 2.53 are

$$\begin{aligned}
\langle\langle \alpha_{xx} \rangle\rangle &= \Delta\alpha\ \langle\langle \cos^2\theta_x \rangle\rangle + \alpha_\perp \\
\langle\langle \alpha_{yy} \rangle\rangle &= \Delta\alpha\ \langle\langle \cos^2\theta_y \rangle\rangle + \alpha_\perp \\
\langle\langle \alpha_{xy} \rangle\rangle &= \Delta\alpha\ \langle\langle \sin^2\theta_z \sin\phi\cos\phi \rangle\rangle = \langle\langle \alpha_{yx} \rangle\rangle.
\end{aligned} \tag{2.54}$$

We calculate that $\langle\langle \alpha_{xy} \rangle\rangle = 0$ for linear molecules interacting with linear and circular polarizations (cf. Appendix A).

From the definition $k^2 = k_x^2 + k_y^2$, one can calculate the wavelength temporal modulation due to molecular alignment by

$$\frac{d\lambda}{dt} = -\frac{\lambda^2}{2\pi k}\left\{\frac{\partial\varphi_x}{\partial z}\frac{\partial^2\varphi_x}{\partial t\partial z} + \frac{\partial\varphi_y}{\partial z}\frac{\partial^2\varphi_y}{\partial t\partial z}\right\} \tag{2.55}$$

using equations 2.52 and 2.53. Note that the time-independent term, $\alpha_\perp$, in Eq. 2.54 does not contribute to the temporal modulations of wavelength in Eq. 2.55.

2.10.1 Discussion

Argon

Fig. 2.19 shows the probe's $\Delta\lambda_{\mathrm{CS}}$ as function of its delay with the pump for both linearly and circularly polarized pump and probe, when the gas cell is filled with argon at atmospheric pressure. It is obvious that the peak of $\Delta\lambda_{\mathrm{CS}}$ is equal for both linear and circular polarization. Ratio of the second-order refractive index due to the electronic Kerr effect between circular and linear polarizations is known to be $n_2^{\mathrm{cir}} = (2/3)n_2^{\mathrm{lin}}$ [2, 56]. Equal wavelength-shift in argon for linear and circular polarizations observed in our experiment suggests that the intensity inside the filament generated by circularly polarized laser is 1.5 the intensity of the linearly polarized filament. This observation agrees with previous studies on the single filaments produced by linearly and circularly polarized lasers [57, 37] where it is shown that the circularly polarized filament could carry intensities up to twice the intensity of linearly polarized filaments without breaking into multiple filaments. The electronic Kerr effect is calculated by Eq. 2.49 and shown by the black dotted lines in Fig. 2.19. For linear and circular polarization the electronic Kerr peaks at the same delay, which verifies the equality of "$n_2\, I$" factor for either of polarizations.

From Eq. 2.49 we expect that for a symmetric Gaussian pulse, as the pulse in our experiment, the wavelength-shift to be symmetric around zero delay. However, in Fig. 2.19 the positive-delay side around zero-delay does not match the calculations of electronic Kerr effect. If the dashed lines in these figures are added to the dotted lines, which correspond to the electronic Kerr effect, the curve from experimental data is reconstructed. The nature of the phenomenon that creates the dashed line could be attributed to different events during the probe propagation. Doppler shift because of self-generated plasma could be the alleged phenomenon. Although the peak of this effect is not at the zero delay, where we expect peak of the plasma effect

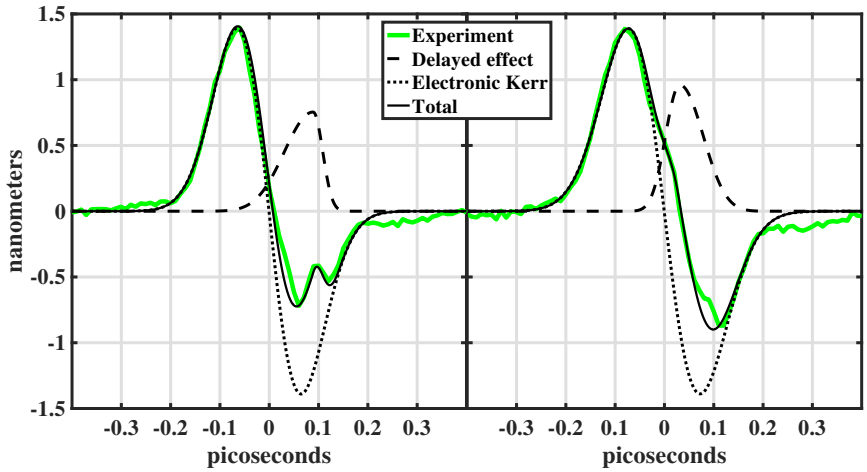

Figure 2.19: $\Delta\lambda_{CS}$ of the probe pulse as function of probe's delay with respect to the pump in argon for linearly pump and probe (left) and circularly pump and probe (right). Green line shows the variations of $\Delta\lambda_{CS}$ in argon from the experiment. Dotted lines are the calculated electronic Kerr effect. The dashed lines are delayed effects that are discussed in the text.

to be, it is shown that plasma formation is not instantaneous [58] and its dynamics depends on the laser polarization [59]. Hence, we could expect the peak of this phenomenon to emerge at slightly longer delays. Peak of this effect adds a notch to the minimum of $\Delta\lambda_{CS}$ for the linearly polarized pump and probe while it adds a shoulder to the falling edge of $\Delta\lambda_{CS}$ for the circularly polarized pump and probe.

Position of the peaks of dashed lines are at +32 fs and +89 fs for circular and linear pump-probe, respectively. Also the magnitude of the peaks of dashed lines are different for linear and circular polarizations in addition to their distinctive temporal shapes. These imply that the effect corresponding to the dashed lines are highly polarization-dependent and could be related to the self-generated plasma.

We did not observe any wavelength shift at longer delays beyond the 400 femtoseconds when the cell is filled with argon.

Nitrogen

Contrary to the argon, for nitrogen $\Delta\lambda_{\mathrm{CS}}$ occurs at longer delays beyond the zero delay region. Fig. 2.20 shows $\Delta\lambda_{\mathrm{CS}}$ in nitrogen gas as function of delay for the linearly and circularly polarized pump and probe. It is obvious that the maximum of $\Delta\lambda_{\mathrm{CS}}$ is larger for the linearly polarized pump and probe compared to the circular polarization. We used Eq. 2.55 to numerically calculate the wavelength shift. From the previous case that the cell was filled with argon we expect the intensity of circularly polarized filament to be 1.5 the intensity of linear filament. Hence, we calculate $\Delta\lambda_{\mathrm{CS}}$ with the assumption that $I_{\mathrm{circular}} = 1.5\ I_{\mathrm{linear}}$. This is shown by dashed-dotted line in Fig. 2.20 and predicts $\Delta\lambda_{\mathrm{CS}}$ very well for both the linear and circular polarization cases. This suggests that at longer delays only molecular alignment is responsible for the wavelength shift of the probe. Hence, a pulse passing through air modulates the refractive index of air for extended times beyond the several picoseconds.

Fig. 2.21 shows variations of probe's $\Delta\lambda_{\mathrm{CS}}$ for linearly and circularly polarized pump and probe near the zero-delay region, when the gas cell is filled with N_2. The molecular Kerr effect (dashed-dotted line) is not sufficient to reconstruct the experimental data. We need to consider the electronic Kerr effect at zero delay. It is calculated from Eq. 2.49 and shown with black dotted line.

Peaks of $\Delta\lambda_{\mathrm{CS}}$ due to the electronic Kerr are equal for linear and circular polarizations. This is similar to what we observed in argon. Therefore, we conclude that the "$n_2 I$" factor is the same for linear and circular polarizations in nitrogen. However, wavelength-shift due to the molecular alignment is smaller for circularly polarized pump than the linearly polarized one.

Molecular and electronic Kerr effects should be sufficient to reconstruct the experimental data of wavelength-shift, however, we notice that similar to the experiment

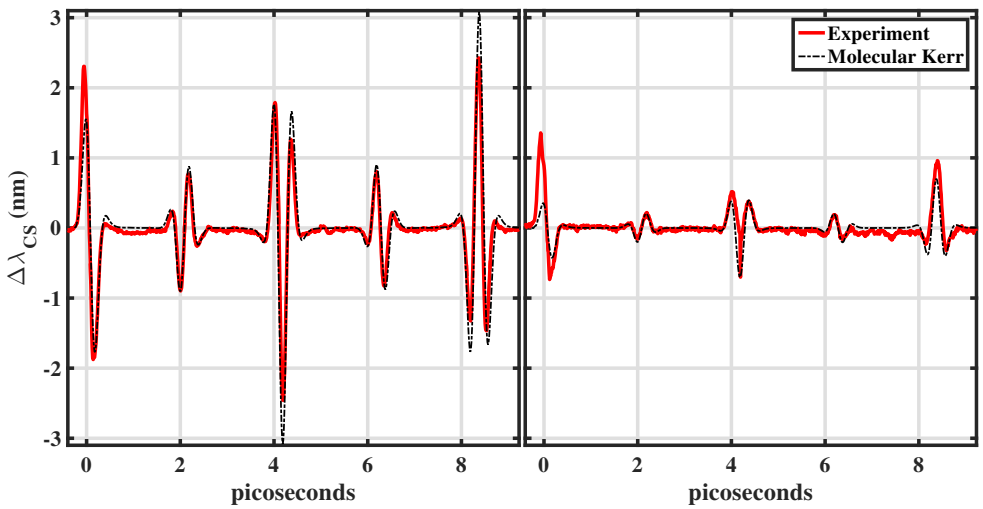

Figure 2.20: $\Delta\lambda_{CS}$ of the probe pulse as function of probe's delay with respect to the pump for linearly pump and probe (left) and circularly pump and probe (right). Red line shows the variations of $\Delta\lambda_{CS}$ in nitrogen from the experiment. Dotted and dashed-dotted lines are the calculated electronic Kerr and molecular Kerr effect and solid black line is the addition of these lines to the dashed line (for discussion about the dashed line see the text).

with the argon another curve is required to be added to the electronic and molecular effects to match the experimental data. Ratio of the peak of this effect in circular to linear pump-probe experiments is 1.35 which is approximately equal to the same ratio in argon. Position of the peaks of dashed lines occur at +25 fs and +82 fs which considering the delay resolution in our setup that is 10 fs the position of peaks are the same as the experiment in argon.

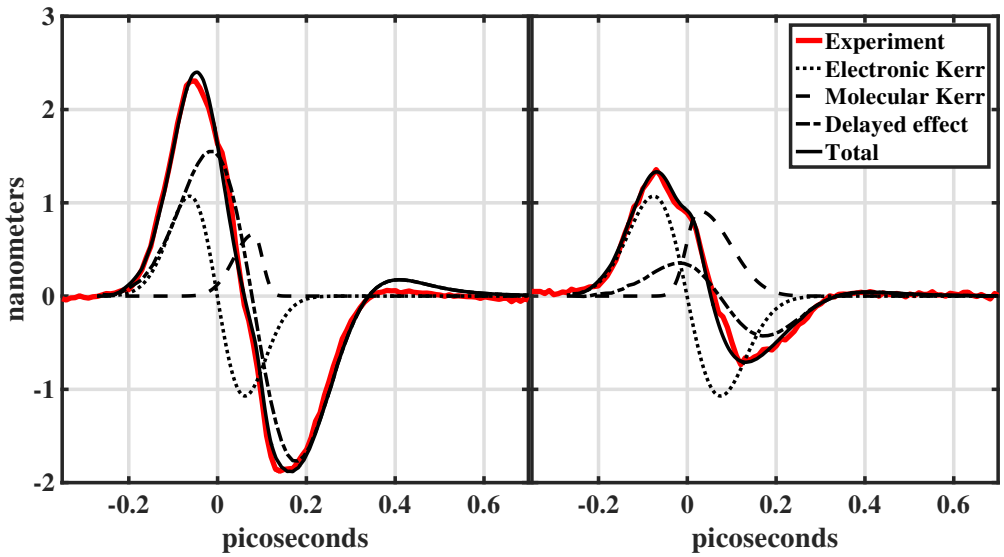

Figure 2.21: $\Delta\lambda_{CS}$ variation of the probe when the gas cell is filled with nitrogen and pump and probe are linearly polarized (left) and circularly polarized (right). $\Delta\lambda_{CS}$ from experiment is shown with the green curve. Dotted and dashed lines represent the calculated $\Delta\lambda_{CS}$ change due to instantaneous Kerr effect and plasma effect, respectively. Black solid line is the addition of dotted and dashed lines.

2.11 Energy exchange between the pump and the probe

We calculate the energy variation of the probe by defining the energy as

$$\Xi = \int_{\lambda_1}^{\lambda_2} \frac{A(\lambda)}{\lambda}\, d\lambda \tag{2.56}$$

where the parameters are defined in Eq. 2.49. Therefore the energy modulation is defined as

$$\Delta\Xi = \Xi - \Xi_0 \tag{2.57}$$

with Ξ_0 the energy of the probe when the pump is blocked.

Argon

Fig. 2.22 shows the energy modulations of the probe propagating in the wake of the pump in argon gas for linearly and circularly polarized pump and probe. This shows that the probe gains energy while interacting with the pump i.e. laser filament. Note that the energy shift maxima are very close in linear and circular polarizations. This is a consequence of equal strength of electronic Kerr in linear and circular polarizations as stated before. Note that at the falling edge of $\Delta\Xi$ i.e. where the probe is returning to its initial energy, a revival of energy occurs. This is shown by the circles in Fig. 2.22. The peak position of this revival matches the peak position of the delayed effect (dashed lines in the figures 2.19 and 2.21) that we already discussed. Higher peak of the delayed effect for the circularly polarized pump and probe case (as is obvious in Fig. 2.19) causes the peak of the revival of $\Delta\Xi$ to be larger for the circular polarization compared to the linear polarization.

Nitrogen

Fig. 2.23 shows $\Delta\Xi$ for the case that the gas cell is filled with nitrogen. This shows that $\Delta\Xi$ depends on the derivative of the refractive index change. Contrary to the previous explanation of this phenomenon [60], according which the energy variation occurs due to the change of coupling of the probe into the spectrometer's fiber tip, we believe that the dependence on the derivative of the refractive index shows that $\Delta\Xi$ could depend on other mechanisms. We notice that the amount of energy exchange is larger for the linear pump and probe case compared to the circular one.

In Fig. 2.24 we zoom into the zero-delay region. We observe that the temporal width of $\Delta\Xi$ is larger for the case that the cell is filled with nitrogen. This is because of onset of the rotational alignment of molecules which occurs at longer delays than

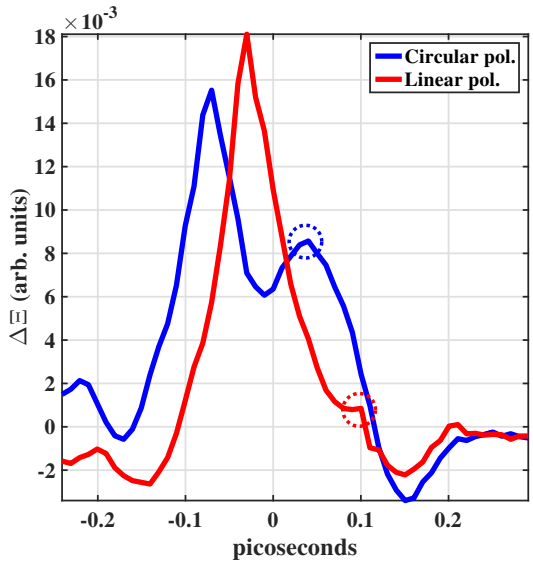

Figure 2.22: $\Delta\Xi$ variation of the probe when the gas cell is filled with argon and pump and probe are linearly polarized (red) and circularly polarized (blue). Temporal position of the dashed lines in the Fig. 2.19 are shown with the center of circles with the corresponding colors.

the electronic Kerr, as discussed before. Here the delayed effect, shown by the dashed lines in Fig. 2.21, further widens the temporal width of $\Delta\Xi$. The temporal position of the peaks of dashed lines in Fig. 2.21 are shown by the circles in Fig. 2.24. It is obvious that at the position of theses peaks the energy is revived with much strength for the case of circular polarization.

2.12 Summary

With the purpose of studying the effect of laser filament propagation in transparent medium we investigated the molecular rotations and its effects on the refractive index of medium. It is shown that the rotation of molecules which occurs on time scale of picoseconds can be controlled by laser field. As the classical model of electric dipole in an electric field suggests that the dipole aligns along the laser field, we

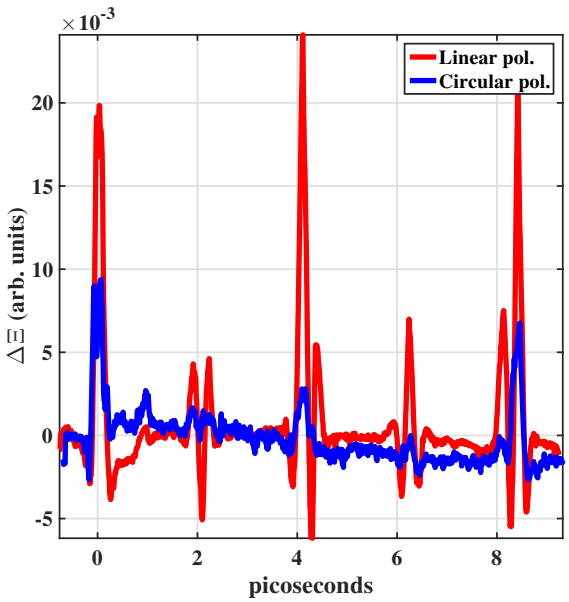

Figure 2.23: $\Delta\Xi$ variation of the probe when the gas cell is filled with nitrogen and pump and probe are linearly polarized (red) and circularly polarized (blue).

showed that for the case of linear molecules the angular distribution of molecules in presence of electric field change in a way that the expectation value of cosine of polar angle reaches a maximum. Depending on the pulse duration there are two types of alignment; adiabatic alignment for which the pulse duration is comparable to the rotational period of molecules and non-adiabatic or impulsive alignment where the pulse duration is much shorter than the rotational period of molecules. In former case the molecules align along the laser polarization axis and reach the minimum angle at the peak of the pulse. At the pulse turn-off molecular ensemble is returned to its isotropic angular distribution. However, for the impulsive scenario the laser field exerts an impulsive excitation of rotational states and leaves the molecules in a superposition of rotational states. These states freely evolve and create a beating pattern that we know them as rotational revivals. Hence, when the pulse is very short the rotational effects persist for time scales far longer than the pulse duration.

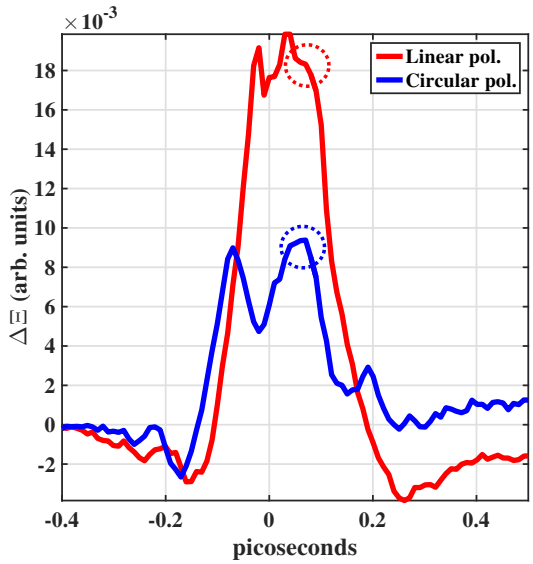

Figure 2.24: $\Delta\Xi$ variation of the probe near the zero-delay region when the gas cell is filled with nitrogen and pump and probe are linearly polarized (red) and circularly polarized (blue). Temporal position of the dashed lines in the Fig. 2.21 are shown with the center of circles with the corresponding colors.

In addition, we studied the effects of pulse intensity and medium temperature on the alignment. Laser polarization showed an important role in the alignment strength and the spatial planes that molecules lie; for linear polarization molecules are aligned around the laser polarization axis and are isotropic in the perpendicular plane, however, circularly polarized laser field aligns the molecules isotropically in the polarization plane.

We related the molecular alignment to the refractive index of medium. Rotational revivals are experimentally showed by a pump-probe experiment and their effect is measured. The theoretical results are fitted against the experimental data by the refractive index modulation formula and polarizability anisotropy of nitrogen is deduced.

It was shown that an additional delayed effect is required to be considered at the

zero delay in order to describe the behavior of the medium under the influence of strong laser pulse. This delayed effect was observed for both atomic and molecular gases. Features of this effect such as peak position, temporal shape and strength, depend on the polarization of the strong pulse. We believe that this effect stems from the retarded formation of the self-generated plasma.

Chapter 3

Emission from laser filaments

Generation of a coherently emitting source at far distances have been a trending field recently to facilitate the stand-off spectroscopy and sensing. The best candidate is to utilize the air constituents as the gain medium. Emission from nitrogen and oxygen, the most abundant parts of air, as they interact with laser filaments have been the subject of extensive studies recently [42, 47, 61].

In oxygen two-photon dissociation by 226 nm breaks the molecule into two atoms of oxygen, one in ground electronic state and the other is excited. Upon the absorption of two photons the atom in ground state makes a transition to the higher state of 3p and then emits an 854 nm photon in backward and forward direction as it decays to 3s state spontaneously [42]. However, absorption and scattering of UV pulse in the atmosphere limits the applications of this method.

Forward and backward emission have been observed in nitrogen, as well. In forward direction emission from the nitrogen ion at 427.8 nm and 391 nm are detected [44] as well as molecular emission at 337 nm [62], however, in the backward direction only transition from molecular excited state at 337 nm is observed [47]. Contrary to emission from oxygen that its population inversion mechanism is known, the

mechanisms of stimulated emission from nitrogen molecules is under debate [48] and the emission mechanism of ions are not understood, yet.

In backward emission of nitrogen the transition of $C^3\Pi_u \rightarrow B^3\Pi_g$ results in a photons in the range between 300-400 nm. The transition from ground state of nitrogen, $X^1\Sigma_g^+$, to $C^3\Pi_u$ (or $B^3\Pi_g$) is optically forbidden in near-IR, hence, collisional pumping should be involved. One channel that could populate the $C^3\Pi_u$ state is

$$\begin{aligned} N_2^+ + N_2 &\rightarrow N_4^+ \\ N_4^+ + e &\rightarrow N_2^+(C^3\Pi_u) + N_2(X^1\Sigma_g^+) \end{aligned} \tag{3.1}$$

Dependence of 337 nm backward lasing on the polarization of the pump suggests another channel in addition to the above-mentioned [63]

$$N_2(X^1\Sigma_g^+) + e \rightarrow N_2^+(C^3\Pi_u) + e \tag{3.2}$$

This process has a maximum cross-section at 14 eV energy of the electrons [63]. It is known that in ionization with circular polarization the electrons acquire higher kinetic energy than the electrons that are liberated in linear polarization. As shown in [64], majority of electrons ionized by circularly polarized filaments with 10^{14} W/cm^2 intensity have energy of 14 eV, however, the electrons liberated by linearly polarized filaments have a peak of energy close to zero. Hence, circular polarization is able to give the electrons enough energy to pump the molecules [64]. Emission from molecular nitrogen is hindered if nitrogen is mixed with oxygen due to the de-excitation of nitrogen by its collision with oxygen [62].

Depending on the pressure of the gas [44], emission from the nitrogen cation is detected in 427.8 nm or 391 nm that correspond to the transition between different

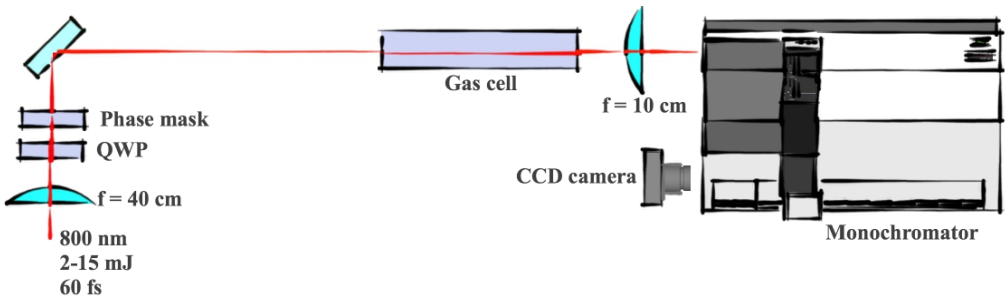

Figure 3.1: The experiment setup that is used to record the emission in the forward direction.

vibrational levels of $X^2\Sigma_g^+ \rightarrow B^2\Sigma_u^+$ [50]. The mechanism of population inversion between ion ground state, $X^2\Sigma_g^+$, and ion excited state, $B^2\Sigma_u^+$, is not revealed yet. According to the Amosov-Delone-Krainov (ADK) model [65] of tunnel ionization the population of $X^2\Sigma_g^+$ is always larger than the $B^2\Sigma_u^+$ if ionization is supposed to be the only pumping mechanism. The reason is that ionization from highest occupied molecular orbital (HOMO) of nitrogen, for which the electron ends up in $X^2\Sigma_g^+$ is more likely (ionization potential 15.6 eV) than the ionization from HOMO-2 for which the electron lands in $B^2\Sigma_u^+$ (ionization potential is 18.7 eV). Hence a population inversion never will form if no post-ionization process takes place. Recently, it is shown that a series of transitions between $X^2\Sigma_g^+$, $A^2\Pi_u$ and $B^2\Sigma_u^+$ after the ionization, yet during the presence of the pump, lead to the population inversion between $X^2\Sigma_g^+$ and $B^2\Sigma_u^+$ [61], however, effect of molecular alignment is neglected.

In this section we present our study on the emission from nitrogen in forward and backward direction pumped by an IR laser filament. The experiment setup is shown in Fig. 3.1. A 10Hz laser at 800 nm wavelength and 60 fs duration provides energies up to 20 mJ. It is focused into a gas cell with controlled pressure. We first present the results of forward emission.

3.1 Emission in the forward direction

Investigation of forward emission is performed by focusing the laser by an f=40 cm lens. The laser beam after gas cell is collected by a 10 cm fused silica lens and focused on the entrance aperture of a monochromator. Configuration of the monochromator is a Czerny-Turner type with focal length of 64 cm. The exit slit of the monochromator is equipped with a CCD with 4872×3248 pixels (each pixel corresponds to 0.0088 nm). The pixel array of CCD spans 42 nm with its center at 426 nm. Polarization of the laser is adjusted by a quarter-wave-plate (QWP) and angular momentum of the beam is controlled by a phase mask.

Fig. 3.2 shows the spectrum recorded by the CCD when the gas pressure is 15 psi. A sharp peak at 427.8 nm is observed that corresponds to $B^2\Sigma_u^+$ ($\nu = 0$) $\rightarrow X^2\Sigma_g^+$ ($\nu = 1$) transition [50]. Circular polarization creates a weak emission at this wavelength than linearly polarized laser. One reason is that the number of ions generated by linearly polarized field is larger than the number of ions created by circularly polarized field for the same intensity. Dependence of stimulated emission on the number of ions is supported by the fact that emission at 427.8 nm is totally vanished when we change the focusing lens to an f=1 m lens. The regime of pulse energy is multiphoton ionization regime, hence, the rate of ionization is proportional to the intensity of pulse [10]. The group of the peaks on the blue side of spectrum are from rotational states of nitrogen and worth to be discussed. Stimulated emission at 427.8 nm in forward direction travels through the molecules that are excited vibrationally and rotationally by the pump. Hence 427.8 nm plays the role of a probe that can investigate the rovibratational levels. Molecular electronic energy levels have energy sub-levels related to the vibrational motion of the molecules. These vibrational levels in turn consist of energy sub-levels that are related to the rotational motion [33]. By considering molecules to behave as anharmonic oscillators that at the same time rotate like a nonrigid rotator, the energy of each rovibrational level is

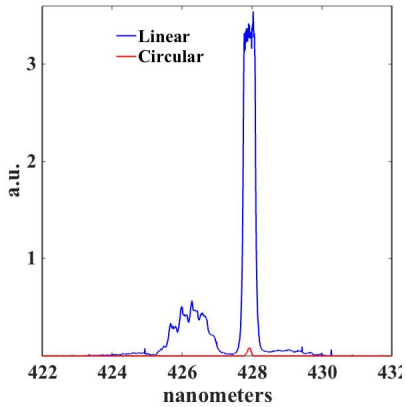

Figure 3.2: Spectra of emission from N_2^+ created by linearly (blue) and circular (red) polarizations.

	T_0	ω_e	$\omega_e x_e$	$\omega_e y_e$	B_e	α_e	$D_e(\times 10^{-6})$
$X^2\Sigma_g^+$	0	2207	16.10	-0.040	1.93176	0.01881	6.1
$A^2\Pi_u$	9166.9	1903	15.02		1.744	0.0188	5.6
$B^2\Sigma_u^+$	25461.4	2419.84	23.18	-0.537	2.07456	0.024	6.17

Table 3.1: Properties of N_2^+ energy states in (cm^{-1})[66]

(cf. Appendix C)

$$E = T_e + \omega_e(\nu + \frac{1}{2}) - \omega_e x_e(\nu + \frac{1}{2})^2 + \omega_e y_e(\nu + \frac{1}{2})^3 + \dots$$
$$+ B_\nu J(J+1) - D_e J^2(J+1)^2 + \dots \tag{3.3}$$

where ν is the vibrational quantum number, J is the rotational quantum number and T_e is the energy of each electronic state. x_e and y_e represent the anharmonicity of vibrational potential and D_e accounts for the non-rigidity of rotating molecule and $B_\nu = B_e - \alpha_e(\nu + \frac{1}{2})$. These values for transitions between $X^2\Sigma_g^+ \leftrightarrow B^2\Sigma_u^+$ are given in Table 3.1.

In Section 2.3 we showed when a molecule is interacting with an intense electromagnetic field, that is far off from any resonant transition between vibrational states, Λ-type rotational transitions with $\Delta J = 0, \pm 2$ occur (Fig. 3.3). On the other hand a

	T_0	ω_e	$\omega_e x_e$	$\omega_e y_e$	B_e	α_e	$D_e(\times 10^{-6})$
$X^1\Sigma_g^+$	0	2358.57	14.32	-0.00226	1.99824	0.017318	-

Table 3.2: Properties of N_2 energy states in (cm^{-1})[67]

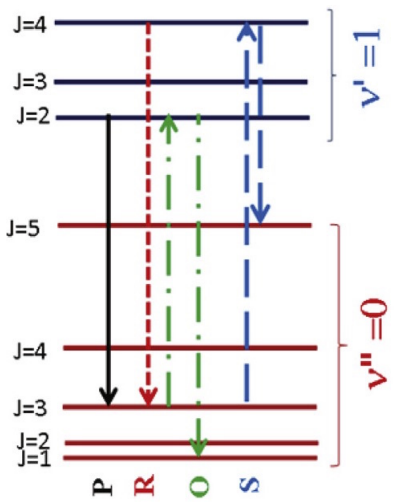

Figure 3.3: Definition of P, R, O and S branches.

photon is emitted when molecule makes transition between different rotational states of $B^2\Sigma_u^+$ ($\nu = 0$) $\rightarrow X^2\Sigma_g^+$ ($\nu = 1$) with $\Delta J = \pm 1$. As previously mentioned, the 427.8 nm (23375 cm^{-1}) photons act as the probe, hence, one can distinguish the transitions involved during the propagation of 427.8 nm by matching the lines corresponding to the R, P, S and O-branches to experimental data. This could shed some light on the dynamics of N_2^+ levels while impulsively excited by intense pulse.

In Fig. 3.4 the measured spectra is plotted as a function of wavenumber in cm^{-1} with 23374 cm^{-1} (427.8 nm) as the zero ($|1/\lambda_{427.8} - 1/\lambda|$). Lines related to even "J"s are superposed on the blue side and red side of the spectrum. Each line is labeled by the final J state e.g. S(2) is related to $J' = 0 \rightarrow J'' = 2$. In Fig. 3.4 R-branch and P-branch lines are plotted on the spectrum. P-branch, that fits to the strongest peak of the spectrum around 427.8 nm, starts from the blue-side and moves toward the red-side. However, as J increases a bandhead is formed and lines

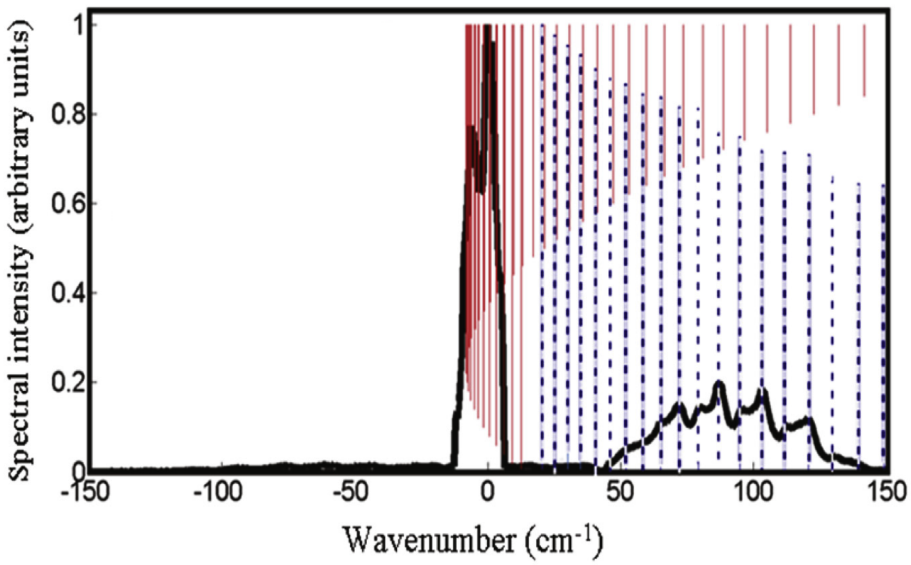

Figure 3.4: Spectrum of emission in forward direction in frequency shift. Zero corresponds to 427.8 nm (23374 cm^{-1}). Red lines correspond to P-branch and Blue lines represent the R-branch transitions of $B^2\Sigma_u^+$ $(\nu' = 0)$ $\rightarrow X^2\Sigma_g^+$ $(\nu'' = 1)$.

change direction towards the blue-side again. R-branch lines, however, start from the blue-side and continue to shorter wavelengths as J increases. This resolves that the strongest peaks around zero are generated by direct transitions among different J states of $B^2\Sigma_u^+$ $(\nu' = 0)$ $\rightarrow X^2\Sigma_g^+$ $(\nu'' = 1)$. Resolution of spectrum is not sufficient for different J states of P-branch to be resolved. Higher J states of P-branch match the lower J values of R-branch, however, R-branch lines match the spectra more precisely.

Fig. 3.5 is a closer look to the side peaks of the spectrum. The liens corresponding to S, O and P-branch are superposed on the spectrum. S-branch lines that correspond to Raman-type transitions are a series of equidistant lines with B(4J+6) separation. First two lines of S-branch, $J' = 0 \rightarrow J'' = 2$ and $J' = 1 \rightarrow J'' = 3$, are covered by the central peaks and $J' = 6$ matches the peak on the red-side. From the Boltzmann

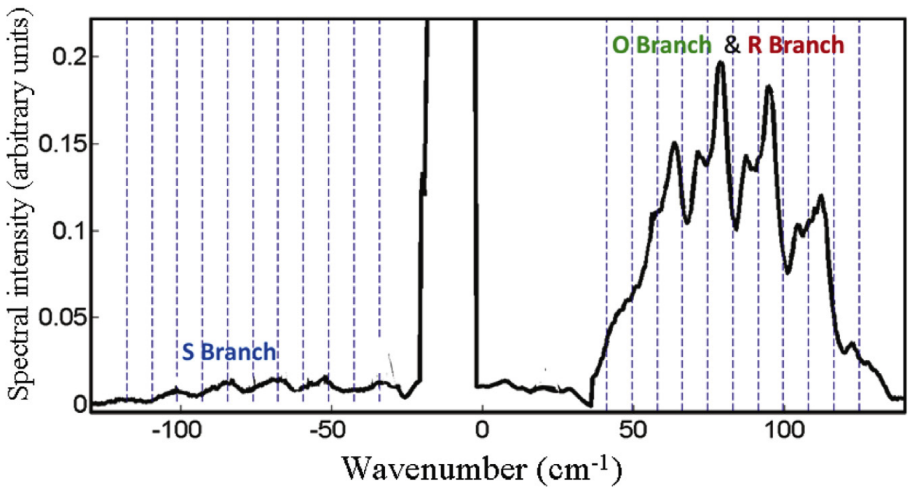

Figure 3.5: Zoomed in version of Fig. 3.4. O and R-branch lines are fitted to the blue-side and S-branch lines are shown on the red-side. Electronic transitions correspond to $B^2\Sigma_u^+$ $(\nu' = 0) \rightarrow X^2\Sigma_g^+$ $(\nu'' = 1)$.

distribution of rotational states we have

$$J_{\max} = \sqrt{k_B T / 2B_e} - \frac{1}{2}, \tag{3.4}$$

hence, the rotational temperature of molecules is 250°K.

Contrary to the equidistant peaks on the red side, the separation of maxima on the blue side are not linear. O-branch and R-branch for $B^2\Sigma_u^+ \rightarrow X^2\Sigma_g^+$ are shown in Fig. 3.5. We see that both lines are at close proximity of the peaks, however, they are not matching satisfactorily. With our measurement apparatus this resolution is the best that we can have. In conclusion we expect the peaks to be a mixture of O and R transitions and definitive results need more precise apparatus and theoretical studies.

One of the factors that is usually ignored in numerical calculations of transitions between the nitrogen ion states is the rotation of molecules. Optical transition between $A^2\Pi_u$ and $B^2\Sigma_u^+$ is forbidden and depends on the orientation of nitrogen ion for $A^2\Pi_u \rightarrow X^2\Sigma_g^+$ and $B^2\Sigma_u^+ \rightarrow X^2\Sigma_g^+$. The dipole matrix element for these tran-

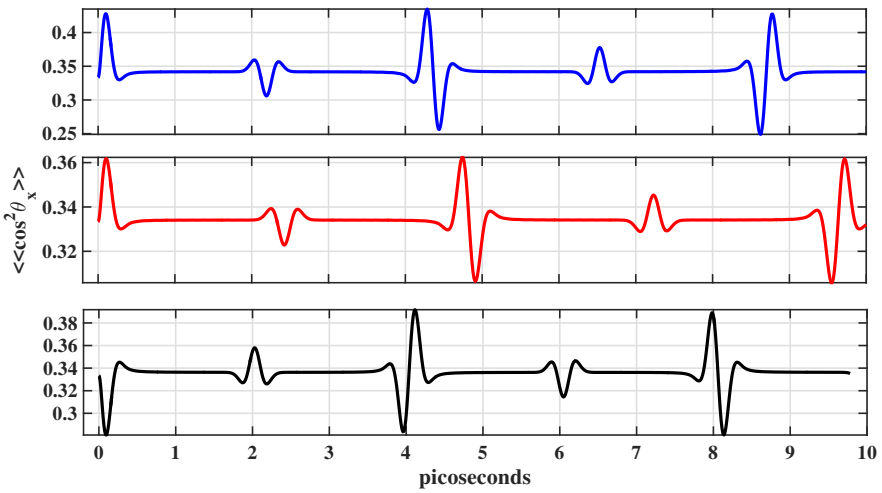

Figure 3.6: $\langle\langle \cos^2\theta \rangle\rangle$ of different states of N_2^+ interacting with a 60 fs pulse carrying 50 TW/cm^2. $X^2\Sigma_g^+$ (blue), $A^2\Pi_u$ (red) and $B^2\Sigma_u^+$ (black).

sitions are $\langle X^2\Sigma_g^+|\mu_\perp|A^2\Pi_u\rangle = 0.7 Debye$, $\langle X^2\Sigma_g^+|\mu_\parallel|A^2\Pi_u\rangle = 0$, $\langle X^2\Sigma_g^+|\mu_\parallel|B^2\Sigma_u^+\rangle = 1.8 Debye$ and $\langle X^2\Sigma_g^+|\mu_\perp|B^2\Sigma_u^+\rangle = 0$ [68, 69].

Variations of $\langle\langle \cos^2\theta \rangle\rangle$ of different states of N_2^+ interacting with a laser pulse of 60 fs duration and 50 TW/cm^2 intensity are calculated and shown in Fig. 3.6 by the same methods as Chapter 2. We assume that the ionization occurs at the peak of the pulse. Difference in the strength of alignment at revivals and even at the flat parts is obvious. This implies that the above-mentioned dipole matrix elements should be reevaluated by considering the change of dipole moment because of alignment. More important is the different revival periods of states. This suggests that despite the negligible effect of alignment on the stimulated emission [61] alignment can play an important role on the transitions initiated by the 427.8 nm. Ni et. al. showed that the lifetime of fluorescence emission from nitrogen ion is more than 20 picoseconds [70]. Hence, our numerical simulations of alignment for nitrogen ion emphasize the importance of alignment effect on the transitions of N_2^+.

3.2 Effect of the laser beam's angular momentum on the forward emission

In Fig. 3.1 we showed that the effect of the beam angular momentum is tested by placing a phase mask in the path of 800 nm pulse. Phase masks produce optical vortices by gradual phase shift across the beam profile by $\exp(im\phi)$, modulo 2π, where "m" defines the order of the vortex [71]. As shown in Fig. 3.7, design of the optical mask is in the form of a pie that each slice of it has a different optical path. For m-order mask, it imposes a total phase shift of $2m\pi$ between the areas of the beam that pass through the thinnest and the thickest part of the mask. The emerging beam from the optical mask is in form of a helix as a result of the delay.

Optical vortices collapse to $2m + 1$ filaments if the beam power is more than the critical power of $P_{\text{crit}}(m) = 2\sqrt{3}mP_{\text{crit}}(0)$ where $P_{\text{crit}}(0)$ is the critical power of a Gaussian beam. This implies that beams with angular momentum $m \neq 0$ have higher clamping intensities that bring stronger nonlinear interactions inside the filament.

One of the important features of the laser filamentation is supercontinuum generation [21]; a broad continuum of new wavelengths are generated because of self-phase modulation and enhanced by four-wave-mixing [24].

Given that the clamping intensity inside the filaments with $m \neq 0$ is higher one expects that they generate supercontinuum generated that is stronger in spectrum than the one generated by $m = 0$ filaments. Fig. 3.8 shows that the spectrum from the filament with $m = 1$ has stronger features around the 400 nm region compared to the spectrum of $m = 0$ filament. This could be a proof of the seeding assumption. We see that in Fig. 3.8 427.8 nm emission and its side-peaks run over a continuum in the case of beam with angular momentum. More interesting is that with angular momentum the circularly polarized beam has a competitive amount of 427.8 nm with

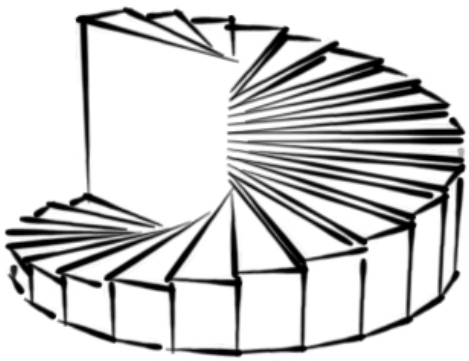

Figure 3.7: Schematic of the structure of a phase mask. Thickness of the transparent material is different across the transverse beam profile, hence, it creates phase lags between different parts of the beam.

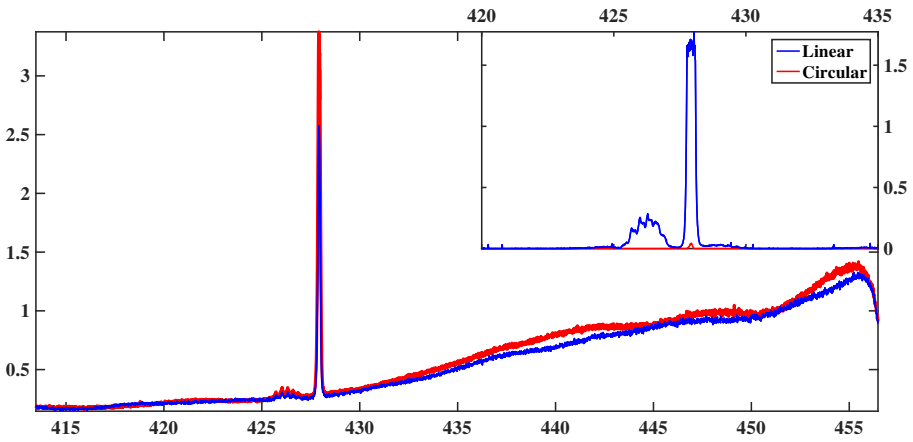

Figure 3.8: Comparison of forward emission at 427.8 nm for linear (blue) and circular (red) polarizations with phase-mask. Inset shows results of the same experiment but without phase-mask. Abscissa is in nanometers unit and units of ordinate are arbitrary, however, comparable to ordinate of inset.

the one from linear polarization.

The effect of polarization on the emission could be twofold. Firstly, for the same intensity, linearly polarized light has a higher ionization rate and ,secondly, circular and linear polarizations drive the electrons in differently in terms of drift energy which affects the collisional pumping. The former should favor stronger forward emission with linear polarization while the later is not involved in any of the alleged processes known for nitrogen ion pumping. This brings us to the conclusion that the shape of focusing plays a role in the nitrogen ion pumping for $m = 1$ the beam breaks into two spots that propagate while spinning around the center of initial Gaussian beam.

3.3 Emission in the backward direction

The experiment's setup for detecting the backward emission from N_2 is shown in Fig. 3.9. In the backward direction we used an f=1 m lens to focus the laser. Behind the tilting mirror, that stirs pump towards the gas cell, there is a fused silica lens with f=10 cm to focus the backward emission into an optical fiber. On the other tip of the fiber there is another 10 cm biconvex lens that couples the output into the same monochromator described above, however, CCD is replaced by a photomultiplier tube detector.

Recorded spectrum is shown in Fig. 3.10 with its peaks at 336.8 nm, 353.1 nm, 357.4 nm, 375.4 nm and 380.3 nm. These values match the spectrum of neutral N_2 for transition between various vibrational levels of $C^3\Pi_u \rightarrow B^3\Pi_g$ [50]. With the change of lens to an f=2 m or f=40 cm signal is lost or at least drops significantly below the sensitivity of detector.

In Fig. 3.11 we compare the signal in backward direction for different values of

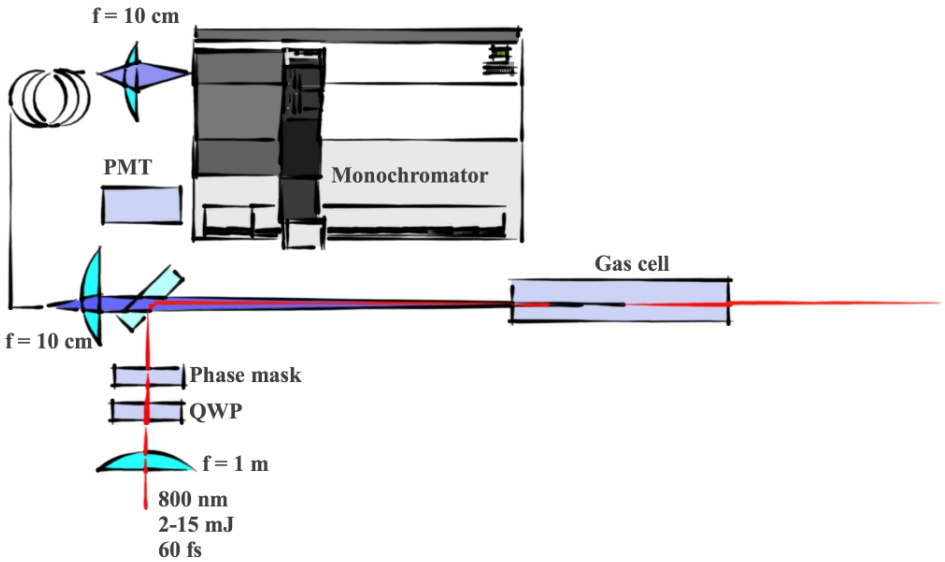

Figure 3.9: Experimental setup for detecting the backward emission from N_2. 800 nm laser pulses with 60 fs duration are focused into the gas cell by a f=2 m lens. The signal in backward direction is collected by a focusing lens of f=10 cm into the aperture of an optical fiber and coupled into the opening of a monochromator by another f=10 cm lens. A PMT detector records the signal.

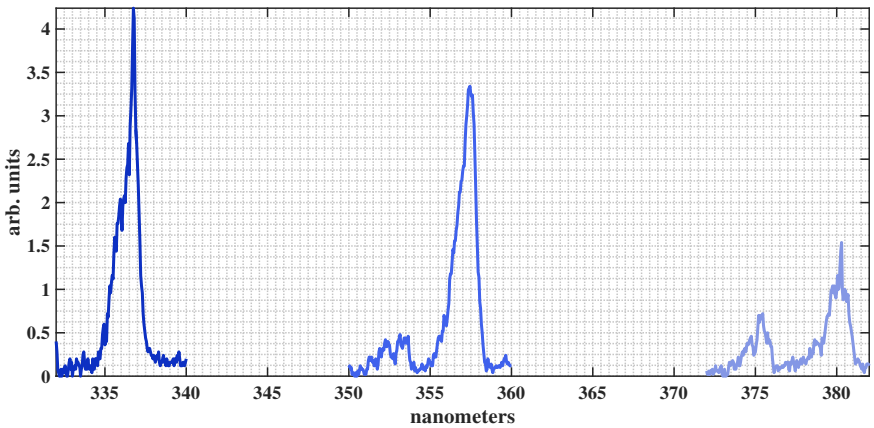

Figure 3.10: Spectrum of backward emission from a nitrogen gas pumped by linearly polarized 800 nm pulse with 60 fs duration.

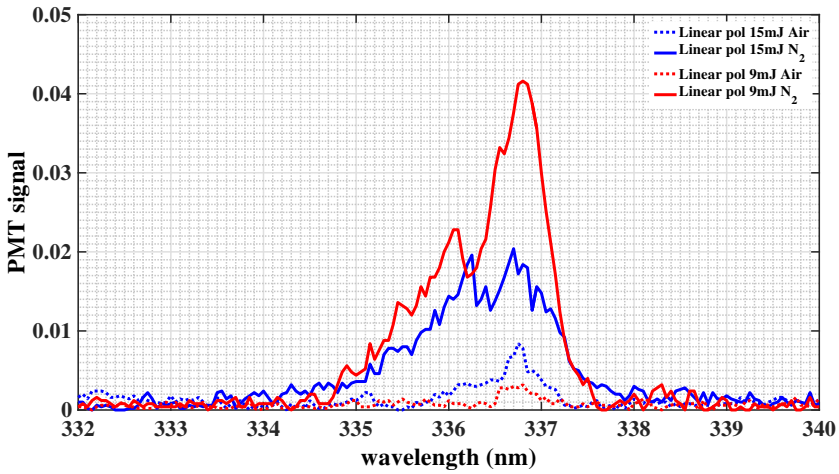

Figure 3.11: Signal of the backward emission for two different pulse energies.

energy in air and pure nitrogen. We observe that in the air the signal decreases compared to its value in pure nitrogen. This shows that the pumping mechanism is less efficient in the air. The quenching effect in air that is responsible for depopulating $C^3\Pi_u$ is [72]

$$N_2(C^3\Pi_u\ ) + O_2 \rightarrow N_2(X^1\Sigma_g^+\ ) + O + O. \tag{3.5}$$

We also observe that the increase in the pump's energy does not increase the value of backward signal i.e. the signal is less for the 15 mJ pump compared to the signal of 9 mJ pump. This suggests that the increase in the pump's energy could counteract the populating effect and suppress the signal in backward direction from nitrogen molecules.

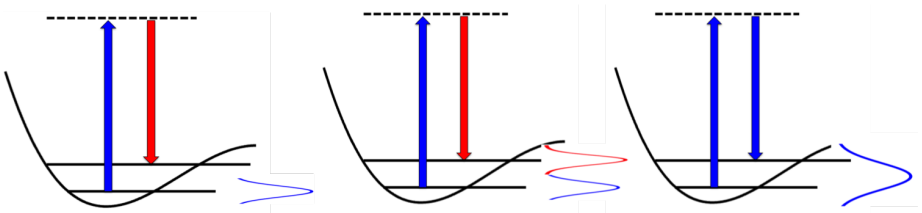

Figure 3.12: Different types of Raman scattering depending on the pulse bandwidth. Left, Spontaneous Raman scattering where only one pulse is required. The bandwidth of this pulse is narrower than the energy spacing between the two states. Middle, Stimulated Raman scattering which needs two simultaneous beams. Each of these beams have a bandwidth that is narrower than the energy spacing between the two states and their central wavelengths are slightly different. Right, impulsive Raman scattering where one pulse with a bandwidth broader than the spacing of two levels is required. Levels can be either vibrational or rotational levels.

3.4 Backward Raman scattering stimulated by laser filamentation

Raman scattering in gases is the result of inelastic scattering of photons by molecules. As discussed in Chapter 2, polarizability of a Raman-active molecule i.e. a molecule that inelastically scatters off a photon, must be changed during the interaction. Polarizability of a molecule changes in two ways; (1) by rotation of molecule (cf. Chapter 2) that causes rotational Raman scattering and (2) displacement of internuclear distance which leads to vibrational Raman scattering. Spacing between vibrational levels is several times the spacing between rotational states e.g. vibrational Raman scattering of N_2 in ground state ($X^1\Sigma_g$) shifts the frequency about 2358 cm^{-1} and rotational Raman scattering for the same electronic level and lowest vibrational level shifts the photon's energy about 12 cm^{-1} (cf. Eq. C.18).

Depending on the bandwidth of the exciting pulse there are different types of Raman scattering. Left panel of Fig. D.1 shows the spontaneous Raman scattering where one pulse is sufficient with its bandwidth (ω) narrower than the spacing

between the involved states (Ω). Stimulated emission, Fig. D.1 middle, needs two pulses with their bandwidths narrower than Ω and relation between their central frequencies $\omega_2 - \omega_1 = \Omega$. Impulsive stimulated Raman scattering picks the involved photons in the scattering from frequencies of a single pulse, where the bandwidth of the pulse is larger than Ω. This case is shown in right panel of Fig. D.1.

In stand-off spectroscopy in gaseous medium the spontaneous Raman scattering is popular because it is straightforward to initiate. Simplicity of this method is because it requires a narrow bandwidth pulse which technically is easier to produce than broadband pulses. However, it is a challenging task to collect the signal as the cross section of interaction is small [73] and the generated wavelength is spatially isotropic. We have recorded spontaneous Raman signal of nitrogen molecules in air by a 266 nm pump. This laser produces 200 ps pulses with 100 mJ energy at 1 Hz repetition rate. Recorded anti-Stokes signal is shown in Fig. 3.13. Ration of the pump to anti-Stokes is not clear as the spectrometer is saturated. Wavelength shift matches the value of 2358 cm^{-1} of N_2.

Coherent Raman scattering methods, which benefit from directionality of signal, have significantly higher gain. Drawback to this method is that one needs widely tunable sources to initiate the stimulated Raman scattering or a a widely broadband sources to stimulate the impulsive Raman scattering e.g. to establish coherent oscillations between the vibrational levels of N_2 ground state with $\omega_e = 2358$ cm^{-1} (cf. Appendix C) the pulse width must be shorter than 15 fs. Another significant issue is diffraction of the pump beams which hinders the efficiency of interaction at the desired location.

Laser filamentation can suppress the bandwidth obstacle through strong self-phase modulation which leads to supercontinuum generation and with appropriate compensation the pulse can be compressed in time [21, 74]. Self-phase modulation expands the bandwidth of the pulse as a function of intensity derivative [2]. Clamped

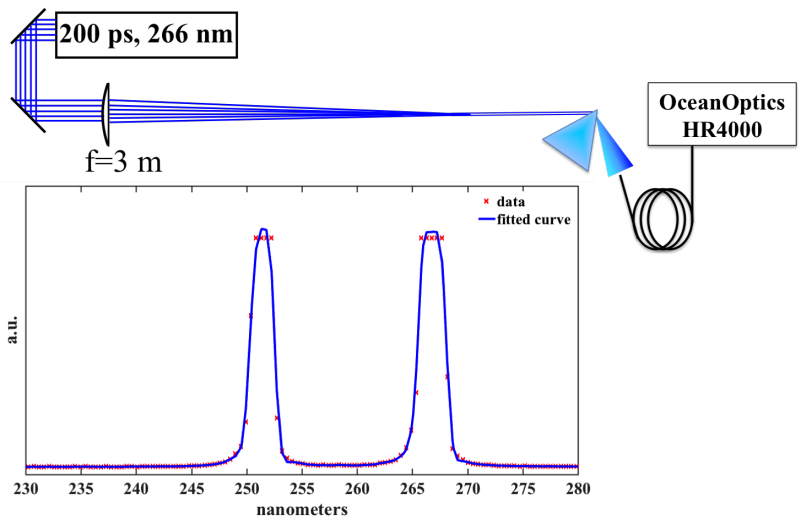

Figure 3.13: Spontaneous Raman signal of 266 nm laser by nitrogen molecules in air. Signal is saturated and the ratio between the peaks is not clear. Beam after focus passes through a fused silica prism to separate the pump and then spectrum is recorded by an OceanOptics HR4000 spectrometer.

intensity inside the filament core reaches extreme values [64] that enhance the self-phase modulation process. It is shown that laser filamentation process can be used to compress a 38 fs pulse down to 7 fs [75]. The beam self-cleaning which is another spectacular outcome of filamentation [23] delivers a beam with nice spatial profile which is very important from the focusing viewpoint. Resultant short pulse can be used to excite the impulsive Raman process in many molecules. Odhner and colleagues stimulated the impulsive Raman scattering by a filament-assisted compression method and probed it by a very longer pulse to detect the constituents of air [22]. In [76] no chirp post-compensation is used to shorten the pulse duration, however, the compression during the filamentation is enough to excite the coherent Raman scattering.

In stand-off spectroscopy the detection setup is desired to be around the pumping source. Light detection and ranging (LIDAR) techniques have recorded spontaneous

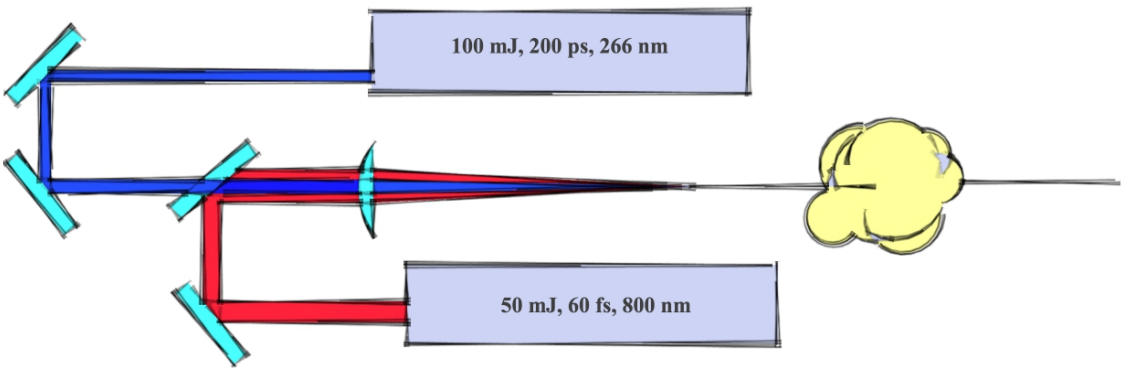

Figure 3.14: Coherent Raman is impulsively stimulated by 800 nm ultrashort laser pulse. A UV pulse at 266 nanometer probes the excited Raman active molecules and signal in backward is amplified.

Raman signals from atmospheric particles [77]. This method needs collecting optics with large numerical aperture to collect enough signal. In coherent Raman scattering if the Raman signal propagates in opposite direction as the pump then the signal-to-noise ratio increases significantly. This signifies the importance of backward Raman signal. Malevich et. al. recorded the Raman signal of nitrogen and oxygen molecules by combining two narrowband tunable lasers [78].

In this section we show the possibility of coherent LIDAR pumped by an 800 nm laser filament and probed by a longer UV pulse Fig. 3.14. 800 nm pulse undergoes filamentation and is compressed enough so its bandwidth is wider than the vibrational levels of molecules. This initiates impulsive Raman interaction and couples the vibrational levels with $\Delta\nu = \pm 1$ (cf. Appendix C). UV pulse encounters an ensemble of already excited molecules and a coherent interaction takes place.

We assume that only two vibrational states are involved which is a legitimate condition for many molecules. The interaction equations are (cf. Appendix D for

details)

$$
\begin{aligned}
\frac{\partial \tilde{E}_\ell}{\partial z} - \frac{n_\ell}{c}\frac{\partial \tilde{E}_\ell}{\partial t} &= -\frac{\mu_0 N |e\lambda_{02}|^2 \omega_\ell c}{2n\hbar}\sigma_{20}^* \\
\frac{\partial \tilde{E}_s}{\partial z} + \frac{n_s}{c}\frac{\partial \tilde{E}_s}{\partial t} &= -\frac{\mu_0 N |e\lambda_{12}|^2 \omega_s c}{2n\hbar}\sigma_{21}^* \\
\dot{\sigma}_{10} &= -i\Delta\sigma_{10} + i(\frac{|\tilde{E}_\ell|^2 - |\tilde{E}_s|^2}{\delta})\sigma_{10} + i\tilde{E}_s\tilde{E}_\ell^*(\frac{\sigma_{11}-\sigma_{00}}{\delta}) \\
\dot{\sigma}_{00} &= 2\mathrm{Re}(\frac{i\tilde{E}_\ell\tilde{E}_s^*\sigma_{10}}{\delta}) \\
\dot{\sigma}_{11} &= 2\mathrm{Re}(\frac{i\tilde{E}_\ell^*\tilde{E}_s\sigma_{10}^*}{\delta}) \\
\sigma_{20} &= i\frac{\sigma_{00}\tilde{E}_\ell^* + \sigma_{10}\tilde{E}_s^*}{\delta} \\
\sigma_{21} &= i\frac{\sigma_{11}\tilde{E}_s^* + \sigma_{10}^*\tilde{E}_\ell^*}{\delta}
\end{aligned}
\tag{3.6}
$$

where Δ, δ are shown in schematic of levels in Fig. 3.15. σ_{ij} are the elements of density matrix while $\tilde{E}_\ell$ and $\tilde{E}_s$ are the Rabi frequencies (cf. Eq. D.6). Level 2, shown in Fig. 3.15 as a thick line, is assumed to be far from any resonances with the electric fields.

The set of Eq. 3.6 is numerically solved by fourth-order Runge-Kutta method [79]. Fig. 3.15 shows the numerical results of impulsive interaction with initial conditions of $\sigma_{11} = 0$, $\sigma_{00} = 1$ and $\sigma_{10} = 0$ or in other words electron is in the lowest level which is true for vibrational levels of molecules in room temperature. It is assumed that the losses of electric fields are negligible i.e. the first two equations in Eq. 3.6 are ignored. Laser pulse is considered as 10 fs with 10 TW/cm^2 of intensity and with the detuning $\Delta = 1$ THz and $\delta = 100$ THz. Final values at the end of the pulse

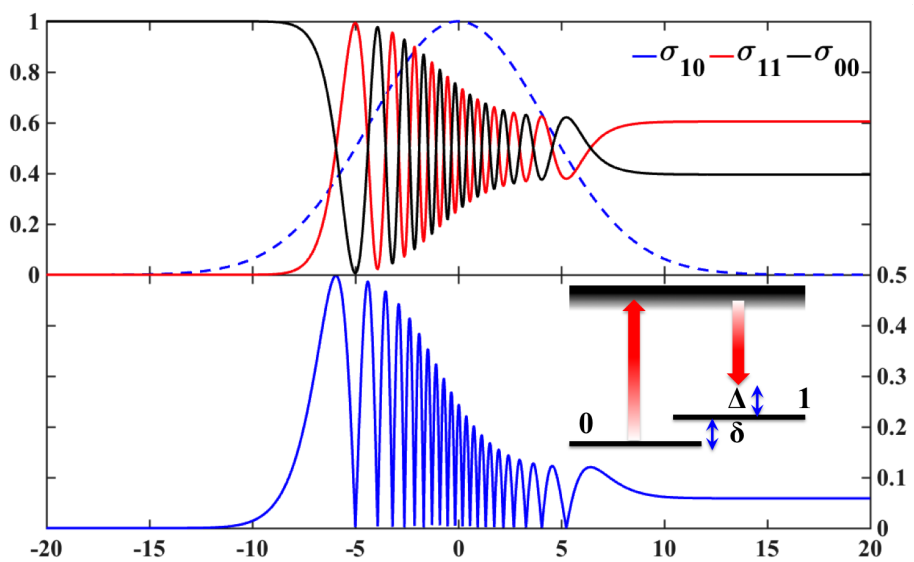

Figure 3.15: Time evolution of correlation between $|0\rangle$ and $|1\rangle$ levels. Pulse duration is 10 fs with peak intensity of 1×10^{13} W/cm^2, $\Delta = 1 \times 10^{12}$ Hz and $\delta = 1 \times 10^{14}$ Hz. Inset: schematic of the involved levels and detuning definitions. Abscissa is in femtoseconds unit.

are $\sigma_{11} = 0.6$, $\sigma_{00} = 0.4$ and $\sigma_{10} = 0.06$. These show that an impulsive interaction establishes correlation between states and population of upper level is increased from its initial value of zero.

Final values shown in Fig. 3.15 are introduced in Eq. 3.6 as initial values and the problem of interaction with UV probe is numerically treated. Initial value of $\tilde{E}_s$ is set to zero which implies that no signal exists, initially, and $\tilde{E}_\ell = 2 \times 10^{12}$ Hz. We assume a 100 fs UV pulse. This differs from the practical pulse durations that we will use in future, however, this approximation is enough to give the minimal of the signal amplitude that we can expect. Final values of $\tilde{E}_\ell$ and $\tilde{E}_s$ are shown in Fig. 3.16. We should note that signal amplification occurs only for the case that $\sigma_{10} \neq 0$ or $\sigma_{11} \neq 0$ & $\sigma_{11} \neq \sigma_{00}$. Backward pulse has a step-like shape which is because of the spatial distribution of σ_{ij} with the same step-like function with the higher side with values $\sigma_{11} = 0.6$, $\sigma_{00} = 0.4$ and $\sigma_{10} = 0.06$ and lower side with $\sigma_{11} = 0.55$, $\sigma_{00} = 0.45$ and $\sigma_{10} = 0.04$. Either sides are connected with a linear function of negative slope.

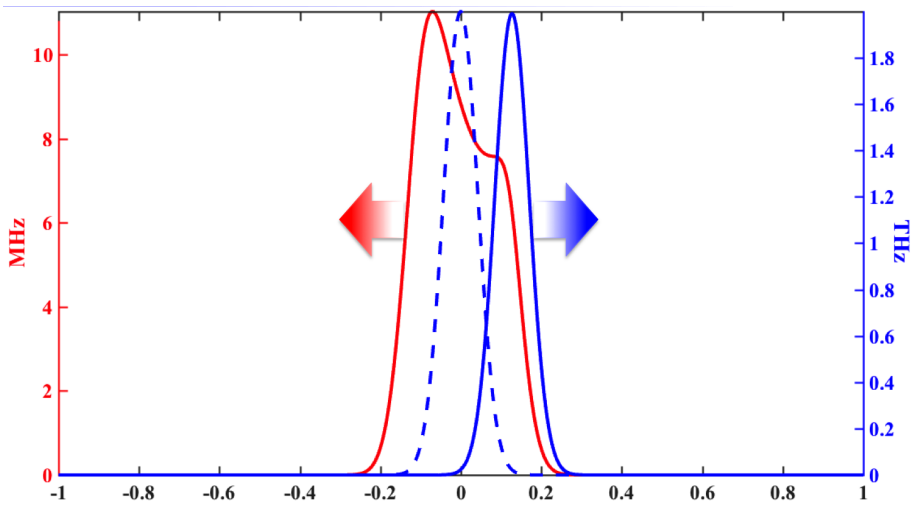

Figure 3.16: Numerical results of backward Raman signal from a molecule that is pumped impulsively as Fig. 3.15. A UV pulse (blue line) with 100 fs duration and Rabi frequency $\tilde{E}_\ell = 2 \times 10^{12}$ Hz interacts with the levels and a Stokes signal in backward direction is generated (red). Signal propagates against the UV probe. Dashed line shows the initial position of the probe in time. Abscissa is in picoseconds units.

These results show the ability of combining IR beams, which need to be of orders of femtosecond in duration to form laser filaments [17], with UV beams to amplify coherent Raman in backward Raman direction. 2D numerical simulations are in order to achieve more realistic results that match the experimental data, however, with this minimal numerical calculations we showed the possibility of detecting Raman signal in backward direction.

3.5 Summary

We studied the resultant emission from interaction of 800 nm laser filaments with nitrogen molecules. Laser filament produces a plasma channel in space from which N_2^+ ions emit through the $B^2\Sigma_u^+$ ($\nu = 1$) $\rightarrow X^2\Sigma_g^+$ ($\nu = 0$) transition at 427.8 nm. This emission is polarization dependent, that is, emission pumped by linearly polarized

pulses is very stronger than the case of pumping with circularly polarized pulse, at the range of energies of our experiment. By matching the lines related to rotational transitions we suggested that the forward emission around 427.8 nm correspond to P-branch transitions from $B^2\Sigma_u^+$ to $X^2\Sigma_g^+$. We showed that the central peak of the spectrum at 427.8 nm plays the role of a probe and the ions that are excited by the laser filament imprint their characteristics on it through Raman-type and resonant transitions. From the recorded spectra we extracted these imprinted information and found that on the red-side of 427.8 nm there are Raman transitions of S type. However, on the blue-side we believe resonant R-branch wavelengths. We ascribe the effect of polarization to the difference in rate of ionization for linear and circular polarizations. Collisional channel which favors the circular polarization is inferior to the other channels in the range of pulse energies in our experiment.

Effect of molecular alignment on the fluorescence emitted from nitrogen ion, pumped by laser filament, is presented. At the instances of molecular alignment the ion signal increases significantly. Pump duration rules out ionization of nitrogen by the pump at picosecond instances. However, the pump excites the nitrogen molecules and impulsively induced alignment revivals increase the ionization rate by the probe pulse. Fourier transform of the signal confirms that emission from $B^2\Sigma_u^+$ is modulated by molecular alignment.

We also investigated the effect of beam's angular momentum on the forward emission from the plasma channel. Signal at 427.8 nm is larger for both circular and linear polarizations compared to the beam without angular momentum and the amount of signal for both polarizations are comparable contrary to the case of beam without momentum. We believe that this discrepancy is due to higher intensities clamped inside the filament generated by beams with angular momentum and the spatial profile of filament generated by beams with angular momentum. We also suggested that for thorough understanding of the forward emission form nitrogen

ion one needs to consider the effect of alignment as the transition between ion states depend on the alignment of molecule with respect to the laser polarization.

Emission from the neutral nitrogen molecules in backward direction are shown. This emission is pumped by 800 nm laser filament and with linear and circular polarizations. Signal spectrum peaks at 336.8 nm, 353.1 nm, 357.4 nm, 375.4 nm and 380.3 nm that match the spectrum of neutral nitrogen molecule for transitions between different vibrational levels of $C^3\Pi_u$ and $B^3\Pi_g$. Magnitude of emission amplitude in backward direction pumped with linearly polarized filament is comparable with the amplitude of emission from circularly polarized filament. We ascribe this to collisional pumping of $C^3\Pi_u$ which favors the circular polarization. At the range of pump energies in our experiment circularly polarized pulse generates electrons with enough energies that are able to populate $C^3\Pi_u$. On this range of energies, ionization channel that favors the linear polarization produces comparable population at $C^3\Pi_u$ as the collisional channel for which circular polarization is more efficient.

In last section we suggested a method to generate Raman emission in backward direction for potential applications in stand-off spectroscopy. We proposed the beam combining between IR and UV pulses. IR pulse is short enough to undergo filamentation and be compressed to very short durations to be able to impulsively correlate two vibrational states of molecules. UV pulse encounters a channel of molecules with correlated vibrational states. Hence, a coherent scattering of UV pulse causes the signal generation. We consider the possibility of this signal to propagate in opposite direction as the UV's. With numerical simulations we showed that signal is generated from its initial value of zero. Practical steps to test the feasibility of this method is discussed in Future Work chapter.

Chapter 4

Filament refueling by Four-Wave Mixing

For many applications it is of great importance to extend the length of filaments. In order to capture the spectrum of a remote sample one needs the high intensity beam to reach the object or control of lightning with laser beams requires the propagation of laser from ground to the sky, however, energy of the filament inside the channel is limited and is dissipated through ionization. Increasing the initial energy of the pulse can help up to a limit, however, excessive energy causes multiple filamentation which divides energy of the pulse between different channels which defeats the goal.

Propagating filament consists a high intensity core that is embraced by a low-intensity background which is called energy reservoir. It is shown that the existence of this energy reservoir is essential to the formation of the filament [29]. In [29] area of this energy reservoir is 5 times the filament core and contains 50% of pulse energy. Numerical simulations show that the filament propagation occurs through the exchange of energy between the core and the reservoir [13].

Scheller et. al. [80] could enhance the longevity of the 800 nm filament by dressing

it with an auxiliary beam which is a loosely focused 800 nm beam. Dressing beam is focused by an axicon lens which generates Bessel beams. Contrary to the Gaussian beams that the longitudinal distribution of intensity is high over a limited range the Bessel beams maintain constant intensity over a long linear focal length i.e. they generate non-diffracting beams [81].

We propose a method to amplify the energy reservoir of the filament by four-wave-mixing (FWM) process. General form of FWM is combination of four different frequencies that are coupled by the third order susceptibility of the medium [2, 1]. This is also called as non-degenerate FWM. Non-degenerate FWM have been used to generate extreme wavelengths [82] from an 800 nm ultrashort pulse. Ghotbi et. al [82] used the third-harmonic of 800 nm and combined it with output of an OPA at 1.6 μm, which is pumped by 800 nm, to generate wavelengths around 150 nm.

Here we use non-collinear combination of 800 nm pulse with a strong 266 nm pulse in air to amplify the IR pulse through FWM

$$\omega_{\mathrm{UV}} = \omega_s + \omega_1 + \omega_2 \tag{4.1}$$

where ω_{UV} and ω_s are the frequencies of 266 nm, 800 nm pulses and ω_1 and ω_2 are two spectral components from 800 nm pulse. For the case of degenerate FWM we have $\omega_s = \omega_1 = \omega_2$.

4.1 Phase-matching with axicon

In addition to the energy conservation, Eq. 4.1, the phase matching parameter is

$$\Delta k = \vec{k}_{\mathrm{UV}} - \vec{k}_s - \vec{k}_1 - \vec{k}_2 \tag{4.2}$$

where subscripts are the same as Eq. 4.1. Difference in refractive indexes of the UV and IR pulses make the collinear phase-matching impossible. However, if 266 nm is

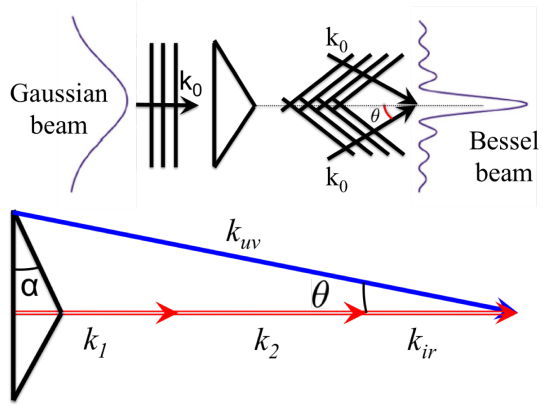

Figure 4.1: Effect of focusing by an axicon on plane wavefront of a Gaussian beam (top). The phase-matching between UV pulse focused by axicon and IR pulse passing a tiny hole at the center of axicon (bottom).

focused by an axicon lens the oblique wavefronts tilt the wavevector of UV pulse. Fig. 4.1 shows wavefronts of the UV beam focused by an axicon and the resultant phase-matching scheme. The coherence length defined as [2]

$$L_{\text{coh}} = \frac{\pi}{k_{UV}\cos\theta - k_1 - k_2 - k_{IR}} \tag{4.3}$$

can be the scale of coherency between the UV and IR pulses. In Eq. 4.3, $\theta = \alpha(n-1)$ with α shown in Fig. 4.1 and n is refractive index of the axicon. Degenerate FWM between 266nm and 800 nm pulses requires $\theta = 0.381°$, considering the refractive indexes in atmospheric pressure. This angle is achievable with a combination of axicon focusing and fine tuning of phase-matching angle through pressure adjustment.

4.2 Numerical simulations

In this chapter we investigate the conditions under which the four-wave mixing between UV and IR pulses lead to the flow of energy from the former to the later. Consequently, the energy reservoir of filament is fed by the energetic UV beam.

From electromagnetic wave equation in a nonlinear medium one derives four coupled equations that describe the FWM between electric fields, $E_i(t) = \tilde{\mathcal{E}}_i(t)\exp[i(\omega_i t - k_i z)]$, as

$$\begin{aligned}
\left(\frac{\partial}{\partial z} + \frac{1}{v_1}\frac{\partial}{\partial t}\right)\tilde{\mathcal{E}}_1 &= -i\chi^{(3)}\ \frac{3\omega_1}{8c}\ \tilde{\mathcal{E}}_2^*\ \tilde{\mathcal{E}}_s^*\ \tilde{\mathcal{E}}_p\ \mathrm{e}^{-i\Delta k z} \\
\left(\frac{\partial}{\partial z} + \frac{1}{v_2}\frac{\partial}{\partial t}\right)\tilde{\mathcal{E}}_2 &= -i\chi^{(3)}\ \frac{3\omega_2}{8c}\ \tilde{\mathcal{E}}_1^*\ \tilde{\mathcal{E}}_s^*\ \tilde{\mathcal{E}}_p\ \mathrm{e}^{-i\Delta k z} \\
\left(\frac{\partial}{\partial z} + \frac{1}{v_s}\frac{\partial}{\partial t}\right)\tilde{\mathcal{E}}_s &= -i\chi^{(3)}\ \frac{3\omega_s}{8c}\ \tilde{\mathcal{E}}_1^*\ \tilde{\mathcal{E}}_2^*\ \tilde{\mathcal{E}}_p\ \mathrm{e}^{-i\Delta k z} \\
\left(\frac{\partial}{\partial z} + \frac{1}{v_p}\frac{\partial}{\partial t}\right)\tilde{\mathcal{E}}_p &= -i\chi^{(3)}\ \frac{3\omega_p}{8c}\ \tilde{\mathcal{E}}_1\ \tilde{\mathcal{E}}_2\ \tilde{\mathcal{E}}_s\ \mathrm{e}^{i\Delta k z}
\end{aligned} \tag{4.4}$$

where p represents the pump wavelength (UV pulse) and $s, 1$ and 2 are the components of IR pulse. By separating the real and imaginary terms through substitution of $\tilde{\mathcal{E}}(t) = \mathcal{E}\exp(i\phi)$, Eq. 4.4 for degenerate FWM is simplified to

$$\begin{aligned}
\left(\frac{\partial}{\partial z} + \frac{1}{v_s}\frac{\partial}{\partial t}\right)\mathcal{E}_s &= \zeta\ \mathcal{E}_s^2\ \mathcal{E}_p\ \sin(\psi - \Delta k z) \\
\left(\frac{\partial}{\partial z} + \frac{1}{v_p}\frac{\partial}{\partial t}\right)\mathcal{E}_p &= -3\zeta\ \mathcal{E}_s^3\ \sin(\psi - \Delta k z) \\
\\
\left(\frac{\partial}{\partial z} + \frac{1}{v_s}\frac{\partial}{\partial t}\right)\phi_s &= -\zeta\ \mathcal{E}_s\ \mathcal{E}_p\ \cos(\psi - \Delta k z) \\
\left(\frac{\partial}{\partial z} + \frac{1}{v_p}\frac{\partial}{\partial t}\right)\phi_p &= -3\zeta\ \mathcal{E}_s^3\ \frac{1}{\mathcal{E}_p}\ \cos(\psi - \Delta k z)
\end{aligned} \tag{4.5}$$

with $\psi = \phi_p - 3\phi_s$ and $\zeta = \chi^{(3)}\ 3\omega_s/8c$. In this equation we assume that signal's wavelength is three times the wavelength of the pump. For the case of phase-matching if the difference between initial phases of the pump and three photons of signal is $\pi/2$, then phases of the either of fields are constant over the time and for $\chi^{(3)} > 0$ the flow of energy is from pump to the signal. Adjustment of phases is possible by manipulation of Gouy phase through focal point variations or by altering the refractive index of one the pulses.

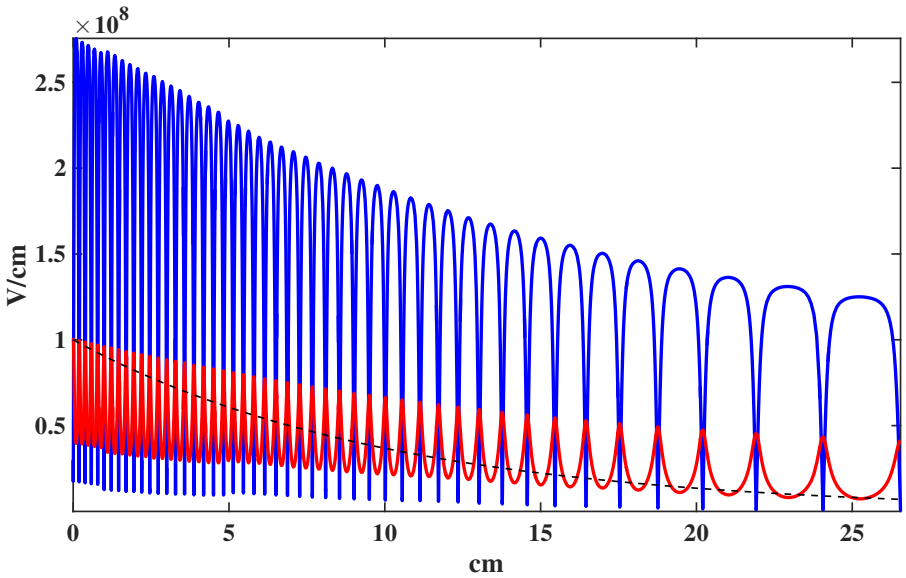

Figure 4.2: Degenerate, phase-matched four-wave mixing between 266 nm field (blue) with initial value of $\mathcal{E}_p^2 = 9 \times 10^{14}$ (V/cm)^2 and 800 nm field (red) with initial value of $\mathcal{E}_s^2 = 10^{16}$ (V/cm)^2. Initial phase difference is $\psi = 3\pi/5$ and IR field is damped by $-0.1\mathcal{E}_s$ factor. Dashed line shows the damping of IR pulse without the pump.

The equation set in Eq. 4.5 are solved numerically by 4th order Runge-Kutta method and the results for initial values of $\mathcal{E}_p = 3 \times 10^7$ V/cm, $\mathcal{E}_s = 10^8$ V/cm and $\psi = 3\pi/5$ are shown in Fig. 4.2. Signal wavelength is 800 nm and pump's wavelength is 266 nm. A damping factor equal to $-0.1\mathcal{E}_s$ accounts for the decay of signal. In this chapter value of $\chi^{(3)} = 2.6 \times 10^{-19}$ W/cm^2 [83] from its relation with $\bar{n}_2$ [1]. Dashed line in Fig. 4.2 shows the signal that propagates with loss, however, no FWM presents. It is obvious that after about 6 cm this field is decreased to half its initial magnitude. With degenerate FWM between this field and UV field, however, periodic exchange of energy between signal and pump takes place. At the end of the simulation range, value of the signal is clearly twice as its magnitude without four-wave mixing. This proves that if FWM is established between the pump and probe it can be used as a method to compensate for the losses of filament channel.

Effect of initial phases of either pulses is discussed and shown in Fig. 4.3. Initial

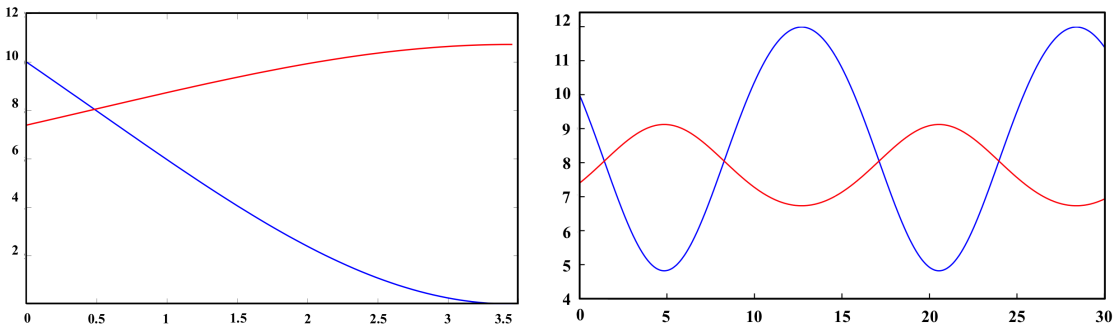

(a) (b)

Figure 4.3: Degenerate phase-matched ($\Delta k = 0$) FWM between 800 nm (red) and 266 nm (blue) fields with initial amplitudes of $\mathcal{E}_p^2 = 10 \times 10^{13}$ (V/cm)^2 and $\mathcal{E}_s^2 = 7 \times 10^{13}$ (V/cm)^2 and initial phases of (a) $\psi = \pi/2$ and (b) $\psi = \pi/10$. Abscissa is in cm units and ordinates are divided by 10^{13}.

differential phase value $\psi = \pi/2$ for which the energy flow is from pump to signal shows a drastic energy exchange and after a short distance pump amplitude hits the zero value, Fig. 4.3a. This is an extreme case and we expect the practical conditions to hinder this situation, however, this proves that the initial phases are crucial to the efficiency of energy exchange and given that the conditions are met energy is drained out of pump, maximally. Comparison of Figures 4.3a and 4.3b signifies the importance of initial phase. We should note that periodic energy exchange could be considered as a drawback to FWM as it seems that energy is pulled from signal at some instances, however, as we shown in Fig. 4.2 for the case of propagation in lossy media the residual amplitude of signal is larger when it is coupled through FWM to a pump.

Eq. 4.5 is numerically solved for the signal as an IR pulse with 40 fs duration and the pump as a UV pulse which is much longer than the signal, therefore, it is assumed to be a DC field. DC value of intensity resembles our proposed experimental method as with the axicon intensity of focused beam is almost invariant over the meter ranges. Initial value of the field square is $\mathcal{E}_s = 7.4 \times 10^{13}$ (V/cm)^2 and $\mathcal{E}_p = 1 \times 10^{14}$ (V/cm)^2

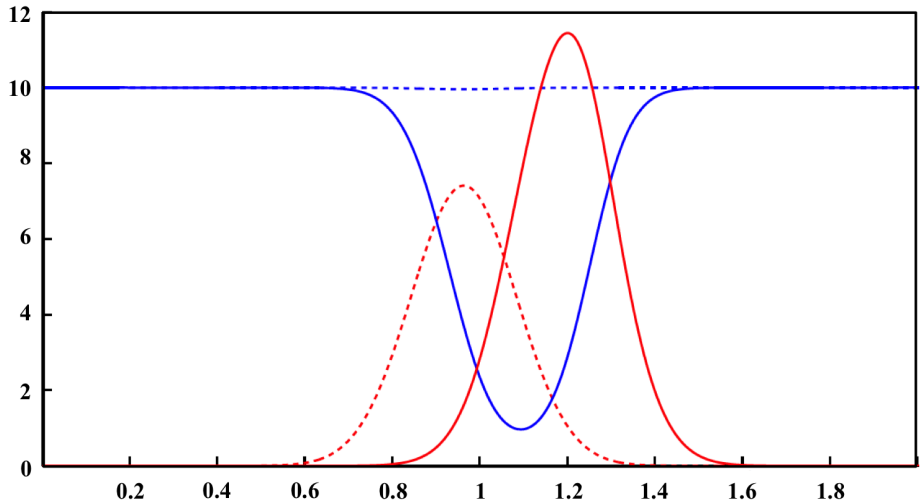

Figure 4.4: Numerical results of Eq. 4.5 for an IR pulse (red) with 40 fs duration and $\mathcal{E}_s = 7.4 \times 10^{13}$ (V/cm)^2 interacting with a DC, UV field (blue) with $\mathcal{E}_p = 1 \times 10^{14}$ (V/cm)^2 through FWM. Initial value of phase difference is $\psi = \pi/2$. Dashed lines represent the initial fields. Abscissa is time axis with 10^{-13} second resolution and ordinate shows square of fields and is divided by 10^{13}.

with $\psi = \pi/2$ and $\Delta k = 0$. Fig. 4.4 depicts the amplification of IR pulse propagating along UV pulse. We account for the difference of velocities between pump and signal, hence, the IR pulse, which propagates faster, moves along UV field. It is obvious that the UV field is refueling the IR field with its energy.

4.3 Summary

The possibility of energy feeding of IR filaments with a UV beam by four-wave mixing is presented. This process depends on the phase-matching parameter which is normally nonzero because of different refractive indexes of the fields. We suggested to use axicon lens and pressure control of the interaction medium to adjust the phase-matching parameter between UV and IR pulses. It is shown that a periodic energy exchange between UV and IR fields occurs, however, IR field that suffers losses has

larger amplitude compared to its value without four-wave mixing after interaction with the pump through FWM. For the initial phase difference of $\pi/2$ the equations suggest that the energy flow is unidirectional from the pump to the signal. Energy exchange process is phase sensitive and in practice the initial phases of the fields can be controlled by focus adjustments or phase manipulation by a thin quartz slab.

Appendix A

Euler rotations and polarizability transformation

In order to project a coordinate frame on another frame by rotational transformation we need three rotations; one around any of the axes of the frame to be rotated, then around any of the other two axes and finally rotation around the first axis. By convention we assume the transformation from body-fixed (XYZ) to space-fixed (xyz) is multiplication of three rotations, first around Z-axis for ϕ (CCW), then around Y-axis for θ (CW) and again Z-axis for ψ (CCW). These rotations are shown in Fig. A.1. So the total rotation matrix is

$$
\begin{aligned}
R &= \begin{bmatrix} \cos\psi & \sin\psi & 0 \\ -\sin\psi & \cos\psi & 0 \\ 0 & 0 & 1 \end{bmatrix} \begin{bmatrix} \cos\theta & 0 & -\sin\theta \\ 0 & 1 & 0 \\ \sin\theta & 0 & \cos\theta \end{bmatrix} \begin{bmatrix} \cos\phi & \sin\phi & 0 \\ -\sin\phi & \cos\phi & 0 \\ 0 & 0 & 1 \end{bmatrix} \qquad \text{(A.1)} \\
&= \begin{bmatrix} -\sin\phi\sin\psi + \cos\phi\cos\psi\cos\theta & \cos\psi\sin\phi + \cos\phi\cos\theta\sin\psi & -\cos\phi\sin\theta \\ -\cos\phi\sin\psi - \cos\theta\cos\psi\sin\phi & \cos\phi\cos\psi - \cos\theta\sin\phi\sin\psi & \sin\phi\sin\theta \\ \cos\psi\sin\theta & \sin\psi\sin\theta & \cos\theta \end{bmatrix}
\end{aligned}
$$

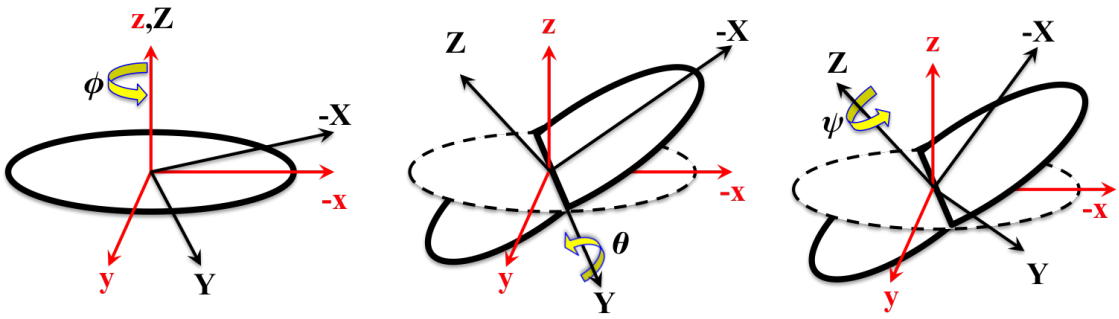

Figure A.1: Euler rotations transformation from body-fixed frame (black) to space-fixed frame (red).

so

$$\begin{bmatrix} x \\ y \\ z \end{bmatrix} = R \begin{bmatrix} X \\ Y \\ Z \end{bmatrix} \tag{A.2}$$

And inverse of rotation matrix is

$$\begin{aligned} R^{-1} &= \begin{bmatrix} \cos\phi & -\sin\phi & 0 \\ \sin\phi & \cos\phi & 0 \\ 0 & 0 & 1 \end{bmatrix} \begin{bmatrix} \cos\theta & 0 & \sin\theta \\ 0 & 1 & 0 \\ -\sin\theta & 0 & \cos\theta \end{bmatrix} \begin{bmatrix} \cos\psi & -\sin\psi & 0 \\ \sin\psi & \cos\psi & 0 \\ 0 & 0 & 1 \end{bmatrix} \\ &= \begin{bmatrix} -\sin\phi\sin\psi + \cos\phi\cos\psi\cos\theta & -\cos\psi\sin\phi - \cos\phi\cos\theta\sin\psi & \cos\phi\sin\theta \\ \cos\phi\sin\psi + \cos\theta\cos\psi\sin\phi & \cos\phi\cos\psi - \cos\theta\sin\phi\sin\psi & \sin\phi\sin\theta \\ -\cos\psi\sin\theta & \sin\psi\sin\theta & \cos\theta \end{bmatrix} \end{aligned} \tag{A.3}$$

so

$$\begin{bmatrix} X \\ Y \\ Z \end{bmatrix} = R^{-1} \begin{bmatrix} x \\ y \\ z \end{bmatrix} \tag{A.4}$$

Then the polarizability tensor in space-fixed axes is

$$\begin{bmatrix} \alpha_{xx} & \alpha_{xy} & \alpha_{xz} \\ \alpha_{yx} & \alpha_{yy} & \alpha_{yz} \\ \alpha_{zx} & \alpha_{zy} & \alpha_{zz} \end{bmatrix} = R^{-1} \begin{bmatrix} \alpha_{XX} & \alpha_{XY} & \alpha_{XZ} \\ \alpha_{YX} & \alpha_{YY} & \alpha_{YZ} \\ \alpha_{ZX} & \alpha_{ZY} & \alpha_{ZZ} \end{bmatrix} R \tag{A.5}$$

For linear molecule where $\alpha_{XX} = \alpha_{YY} = \alpha_{\perp}$ and $\alpha_{ZZ} = \alpha_{\parallel}$

$$\begin{aligned} \alpha_{xx} &= -\alpha_{\perp} \sin^2\theta \cos^2\phi + \alpha_{\perp} + \alpha_{\parallel} \sin^2\theta \cos^2\phi \\ \alpha_{yy} &= -\alpha_{\perp} \sin^2\theta \sin^2\phi + \alpha_{\perp} + \alpha_{\parallel} \sin^2\theta \sin^2\phi \\ \alpha_{zz} &= -\alpha_{\perp} \cos^2\theta + \alpha_{\perp} + \alpha_{\parallel} \cos^2\theta \\ \alpha_{xy} &= -\alpha_{\perp} \sin^2\theta \sin\phi \cos\phi + \alpha_{\parallel} \sin^2\theta \sin\phi \cos\phi = \alpha_{yx} \end{aligned} \tag{A.6}$$

From equation A.2 cosine of the angle between x-axis and Z-axis is $Z.x = \cos\theta_x = \sin\theta\cos\phi$, cosine of the angle between y-axis and Z-axis is $Z.y = \cos\theta_y = \sin\theta\sin\phi$ and cosine of the angle between z-axis and Z-axis is $Z.z = \cos\theta_z = \cos\theta$. Hence

$$\begin{aligned} \alpha_{xx} &= \Delta\alpha \ \cos^2\theta_x + \alpha_{\perp} \\ \alpha_{yy} &= \Delta\alpha \ \cos^2\theta_y + \alpha_{\perp} \\ \alpha_{zz} &= \Delta\alpha \ \cos^2\theta_z + \alpha_{\perp} \end{aligned} \tag{A.7}$$

Appendix B

$\langle \cos^2\theta \rangle$ and selection rules

From the recurrence relation [84]

$$\begin{aligned} x(2j-1)P_{j-1}^m(x) &= (j-m)P_j^m(x) + (j+m-1)P_{j-2}^m(x) \\ \Rightarrow x(2j+1)P_j^m(x) &= (j-m+1)P_{j+1}^m(x) + (j+m)P_{j-1}^m(x) \end{aligned} \tag{B.1}$$

So

$$\begin{aligned} x^2 P_j^m(x) &= \frac{j-m+1}{(2j+3)(2j+1)}\Big[(j-m+2)P_{j+2}^m(x) + (j+m+1)P_j^m(x)\Big] \\ &+ \frac{j+m}{(2j-1)(2j+1)}\Big[(j-m)P_j^m(x) + (j+m-1)P_{j-2}^m(x)\Big] \end{aligned} \tag{B.2}$$

Now the integral

$$\int_{-1}^{1} P_{j'}^m(x)(1-x^2)P_j^m(x)dx \tag{B.3}$$

can be calculated analytically using the orthogonality integral

$$\int_{-1}^{1} P_{j'}^m(x)P_j^m(x)dx = \frac{2}{2j+1}\frac{(j+m)!}{(j-m)!}\delta_{jj'} \tag{B.4}$$

Then

$$\begin{aligned}
\int_{-1}^{1} P_{j'}^{m}(x)(1-x^2)P_{j}^{m}(x)dx &= \int_{-1}^{1} P_{j'}^{m}(x)P_{j}^{m}(x)dx - \int_{-1}^{1} P_{j'}^{m}(x)\ x^2\ P_{j}^{m}(x)dx \\
&= \Big(\frac{2}{2j+1}\Big)\frac{(j+m)!}{(j-m)!}\ \delta_{j'j} \\
&- \Big(\frac{2}{2j+3}\Big)\frac{(j-m+1)(j-m+2)}{(2j+3)(2j+1)}\ \frac{(j+m+2)!}{(j-m+2)!}\ \delta_{j',j+2} \\
&- \Big(\frac{2}{2j-3}\Big)\frac{(j+m)(j+m-1)}{(2j-1)(2j+1)}\ \frac{(j+m-2)!}{(j-m-2)!}\ \delta_{j',j-2} \\
&- \Big(\frac{2}{2j+1}\Big)\frac{(j-m+1)(j+m+1)}{(2j+3)(2j+1)}\ \frac{(j+m)!}{(j-m)!}\ \delta_{j',j} \\
&- \Big(\frac{2}{2j+1}\Big)\frac{(j-m)(j+m)}{(2j-1)(2j+1)}\ \frac{(j+m)!}{(j-m)!}\ \delta_{j',j}
\end{aligned} \tag{B.5}$$

Legendre polynomials and spherical harmonics are related as

$$Y_j^m(\theta,\phi) = \sqrt{\frac{2j+1}{4\pi}\frac{(j-m)!}{(j+m)!}}P_j^m(\cos\theta)\mathrm{e}^{im\phi} \tag{B.6}$$

with orthogonality integral

$$\int_{-1}^{1}\int_{0}^{2\pi} Y_{j'}^{m'}(\theta,\phi)\ \ Y_j^{m*}(\theta,\phi)\ d\cos\theta\ d\phi = \delta_{m'm}\ \delta_{j'j} \tag{B.7}$$

Considering that

$$\int_{0}^{2\pi} \mathrm{e}^{-im'\phi}\ \mathrm{e}^{im\phi}\ d\phi = 2\pi\ \delta_{m'm} \tag{B.8}$$

we calculate the integral below

$$\int_{-1}^{1}\int_{0}^{2\pi} Y_{j'}^{m'*}(\theta,\phi)\ \cos^2\theta\ Y_j^m(\theta,\phi)\ d\cos\theta\ d\phi =$$
$$\Lambda \times \int_{-1}^{1} P_{j'}^{m'}(x)\ x^2\ P_j^m(x)dx \int_0^{2\pi} \mathrm{e}^{-im'\phi}\ \mathrm{e}^{im\phi}\ d\phi$$
$$= \Big[\frac{(j-m+1)(j+m+1)}{(2j+3)(2j+1)} + \frac{(j-m)(j+m)}{(2j+1)(2j-1)}\Big]\ \delta_{m',m}\delta_{j'j}$$
$$+ \sqrt{\frac{(j+m+1)(j-m+1)(j+m+2)(j-m+2)}{(2j+1)(2j+5)(2j+3)(2j+3)}}\ \delta_{m',m}\delta_{j+2,j}$$
$$+ \sqrt{\frac{(j+m-1)(j-m-1)(j+m)(j-m)}{(2j+1)(2j-3)(2j-1)(2j-1)}}\ \delta_{m',m}\delta_{j-2,j} \tag{B.9}$$

where

$$\Lambda = \frac{1}{4\pi}\sqrt{\frac{(2j'+1)(2j+1)(j'-m')!(j-m)!}{(j'+m')!(j+m)!}} \tag{B.10}$$

Appendix C

Vibrational and rotational states of molecules

Molecules have two additional types of motion compared to the atoms; they can *rotate* around their axes of symmetry and concurrently *vibrate* to and fro because of the restoring electric force between their atoms. These additional degrees of freedom bring spectral features to the molecular spectra that are not present in the atomic spectra. Molecules are different in term of their symmetry and consequently their behavior, however, in this section we only discuss the spectra of diatomic molecules without the loss of generality.

C.1 Rigid rotator model of diatomic molecules

The Schrödinger equation of a rotating object that is bound by a restoring force to a very heavy object that is not moving compared to the light object is

$$-\frac{\hbar^2}{2\mu}\Big[\frac{1}{r^2}\Big(r\frac{\partial}{\partial r}\Big)\Big(r\frac{\partial}{\partial r}\Big)+\frac{1}{r}\frac{\partial}{\partial r}-\frac{1}{\hbar^2 r^2}\mathrm{J}^2\Big]\Psi(r,\theta,\varphi)=\Big[E-V(r)\Big]\Psi(r,\theta,\varphi) \tag{C.1}$$

where $\mu = m_1 m_2/(m_1+m_2)$ is the reduced mass of the objects, $V(r)$ is the bonding potential and (r,θ,φ) are the spherical coordinate components. J is the angular momentum operator which commutes with its z-component; $[\mathrm{J}^2,\mathrm{J}_z]=0$. One can assume that the displacement of the particle from its equilibrium point is negligible. The Hamiltonian of a rotating quantum object is therefore

$$H_{\mathrm{rot}}=\frac{\mathrm{J}_X^2}{2I_{XX}}+\frac{\mathrm{J}_Y^2}{2I_{YY}}+\frac{\mathrm{J}_Z^2}{2I_{ZZ}} \tag{C.2}$$

where $I_{XX},\ I_{YY}$ and I_{ZZ} are the moments of inertia, μr^2, around the body-fixed (X,Y,Z) axes. Ψ can be separated to radial and angular parts as $\Psi = R(r)Y(\theta,\varphi)$. Angular solutions of the Schrödinger equation above are shown to be spherical harmonics, $Y_{j,m}(\theta,\varphi)$, with the eigenvalues of

$$\mathrm{J}^2\ Y_{j,m}(\theta,\varphi) = J(J+1)\hbar^2\ Y_{j,m}(\theta,\varphi) \tag{C.3}$$

$$\mathrm{J}_z\ Y_{j,m}(\theta,\varphi) = m\hbar\ Y_{j,m}(\theta,\varphi) \tag{C.4}$$

with $J=0,1,2,\ldots$ and $m\le|J|$.

We focus on the case of linear molecule for which $I_{XX}=I_{YY}=I,\ I_{ZZ}\approx 0$. From $\mathrm{J}^2=\mathrm{J}_X^2+\mathrm{J}_Y^2+\mathrm{J}_Z^2$ the rotation of molecule creates a series of discrete states with energies

$$E_{\mathrm{rot}}=\frac{J(J+1)\hbar^2}{2I} \tag{C.5}$$

In spectroscopy it is more popular to consider the rotational energy terms in units of wavenumber, therefore, for the rigid rotator model we introduce

$$F(J) = \frac{h}{8\pi^2 cI}\ J(J+1) = B\ J(J+1) \tag{C.6}$$

where B is the rotational constant in cm^{-1} units, h is the Planck's constant and c is the speed of light.

C.2 Oscillator model of diatomic molecules

Either of atoms in a diatomic molecule are bound together by a restoring force caused by their electrons' cloud. This force in first approximation can be approximated as a linear function of displacement from the equilibrium point, i.e., $F(r) = -k(r - r_e)$. This model is equivalent of classical harmonic oscillator.

So for the radial part of C.1 the potential energy is

$$V(r) = \frac{1}{2}kr^2 \tag{C.7}$$

Solutions of Schrödinger equation of a harmonic oscillator can be found in many introductory quantum mechanics books. The vibrational states have energies of

$$E_{\text{vib}} = \hbar\omega_{\text{vib}}(v + \frac{1}{2}) \tag{C.8}$$

with $v = 0, 1, 2, \ldots$ where

$$\omega_{\text{vib}} = \sqrt{\frac{k}{\mu}} \tag{C.9}$$

In spectroscopic units (cm^{-1}), the vibrational energy is

$$G(v) = \frac{\hbar\omega_{\text{vib}}}{hc}(v + \frac{1}{2}) = \omega(v + \frac{1}{2}) \tag{C.10}$$

This shows that the energies of harmonic oscillator are equally spaced contrary to the rotational energies of a rigid rotator.

Although the harmonic oscillator model is sufficient to address the features of molecular spectra for small values of v, for higher values this model can not be precise enough. This is due to the shape of vibration potential curve. We expect that if atoms of a molecule move so much from their equilibrium value, the molecule dissociates, i.e., it becomes as two separate atoms. Equivalently, the potential curve flattens for large values of r. In other words the potential curve is deformed from the parabolic shape of harmonic oscillator model.

So the vibration potential of anharmonic oscillator is a polynomial with higher powers of displacement added to the potential of the harmonic oscillator. Energy levels of the solutions of the Schrödinger equations for anharmonic oscillator in cm^{-1} are

$$G(v) = \omega_e(v + \frac{1}{2}) - \omega_e\ x_e(v + \frac{1}{2})^2 + \omega_e\ y_e(v + \frac{1}{2})^3 + \dots \tag{C.11}$$

Values of ω_e, $\omega_e x_e$ and $\omega_e y_e$ decrease rapidly, e.g. these values for the $X^1\Sigma_g^+$ electronic state of N_2 molecule are $\omega_e = 2358.57$, $\omega_e x_e = 14.324$ and $\omega_e y_e = -0.00226$. Anharmonicity removes the equality of distances between energy states that is valid for harmonic oscillator. From C.11 the spacing between vibrational levels decline as v increases.

C.3 Nonrigid rotator model of diatomic molecules

In C.1 the rotator is assumed to be rigid, i.e. distance between the center of gravity and the rotating object is constant over one rotation period. However, this assumption is proved to be an approximate for molecules by observation of their spectra. Variation of internuclear distance in molecules because of the vibration of molecules

affects the rotational motion in two ways. First, a classical picture of rotation requires a centrifugal force to compensate the restoring force. In classical paradigm of rotation we have

$$\mu\omega^2 r = \frac{J^2}{\mu r^3} \tag{C.12}$$

and the equation of centrifugal force and restoring force is

$$r - r_e = \frac{J^2}{\mu r_e^3 k} \tag{C.13}$$

where r_e is the vibration equilibrium position with assumption that $r - r_e \approx r_e$ as the displacement of molecule from its equilibrium position is very small. Energy of a vibrating rotator is

$$E = \frac{J^2}{2\mu r_e^2} + \frac{1}{2}k(r - r_e)^2 = \frac{J^2}{2\mu r_e^2} - \frac{J^4}{2\mu^2 r_e^6 k} \tag{C.14}$$

Quantum mechanical Hamiltonian of this system is resulted by substituting the angular momentum operator. The eigenvalues of such Hamiltonian in cm^{-1} units are

$$\begin{aligned} E &= \frac{1}{hc}\Big[\frac{\hbar^2}{2\mu r_e^2}J(J+1) - \frac{\hbar^4}{2\mu^2 r_e^6 k}J^2(J+1)^2\Big] \\ &= B\ J(J+1) - D\ J^2(J+1)^2 \end{aligned} \tag{C.15}$$

As a result the centrifugal distortion decreases the spacing between rotational energies. In Eq. C.15 higher terms can be introduced if nharmonicity is involved, however, they play less important roles as their amounts are negligible compared to the first two constants.

The second way that vibrations change the rotational motion is that the variation of internuclear distance manipulates the amount of moment of inertia, I, as it is a function of $(r - r_e)$. This in turn affects the values of B and D as

$$B_v = B_e - \alpha(v + \frac{1}{2}) \tag{C.16}$$

$$D_v = D_e - \beta_e(v + \frac{1}{2}) \tag{C.17}$$

Here, higher terms are neglected as their effect is negligible. In conclusion the amount of energy that a molecule contains due to its rotation and vibration is

$$T = \omega_e(v+\frac{1}{2}) - \omega_e x_e(v+\frac{1}{2})^2 + \omega_e y_e(v+\frac{1}{2})^3 + \ldots \\ + B_v J(J+1) - D_v J^2(J+1)^2 + \ldots \qquad \text{(C.18)}$$

Appendix D

Stimulated Raman scattering

Start point is to develop the problem in terms of the differential equations for laser field and matter states

$$i\hbar\frac{\partial\rho}{\partial t} = [H_a - e\hat{\lambda}E(t), \rho] \tag{D.1}$$

where

$$E(t) = \tilde{\mathcal{E}}_\ell(t)e^{i\omega_l t} + \tilde{\mathcal{E}}_s(t)e^{i\omega_s t} + c.c. \tag{D.2}$$

$\tilde{\mathcal{E}}_\ell(t)$ is the laser field and $\tilde{\mathcal{E}}_s(t)$ represents the stokes amplitude of scattered wave and they are slowly varying amplitudes. Some assumptions are made: level 2 never gets populated and it acts as just an intermediate level. Other condition for this system is that there is no optical transition between level 0 and 1 $\lambda_{10} = \lambda_{01} = 0$.

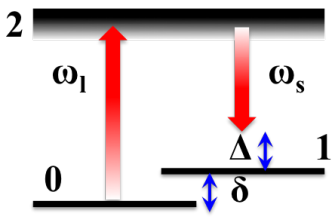

Figure D.1: Sketch showing the three levels 0, 1 and 2 and their detunings with electric fields, ω_ℓ and ω_s.

By expanding Eq. D.1 for a three level atom the differential equations become

$$\begin{aligned}
i\hbar\frac{\partial\rho_{00}}{\partial t} &= eE(t)[\lambda_{20}\rho_{02} - \lambda_{02}\rho_{20}] \\
i\hbar\frac{\partial\rho_{11}}{\partial t} &= eE(t)[\lambda_{21}\rho_{12} - \lambda_{12}\rho_{21}] \\
\frac{\partial}{\partial t}(\rho_{22}+\rho_{11}+\rho_{00}) &= 0 \\
i\hbar\frac{\partial\rho_{10}}{\partial t} &= \hbar(\omega_1-\omega_0)\rho_{10} + eE(t)[\lambda_{12}\rho_{20} - \lambda_{20}\rho_{12} + \lambda_{10}(\rho_{11}-\rho_{00})] \\
i\hbar\frac{\partial\rho_{20}}{\partial t} &= \hbar(\omega_2-\omega_0)\rho_{20} + eE(t)[\lambda_{10}\rho_{21} - \lambda_{21}\rho_{10} + \lambda_{20}(\rho_{22}-\rho_{00})] \\
i\hbar\frac{\partial\rho_{21}}{\partial t} &= \hbar(\omega_2-\omega_1)\rho_{21} + eE(t)[\lambda_{01}\rho_{20} - \lambda_{20}\rho_{01} + \lambda_{21}(\rho_{22}-\rho_{11})]
\end{aligned} \tag{D.3}$$

Elements of matrix ρ for a rotating wave approximation need to be considered as functions that are counter-propagating with respect to the electromagnetic field

$$\begin{aligned}
\rho_{10} &= \sigma_{10}e^{-i(\omega_\ell-\omega_s)} \\
\rho_{20} &= \sigma_{20}e^{-i\omega_\ell t} \\
\rho_{21} &= \sigma_{21}e^{-i\omega_s t}
\end{aligned} \tag{D.4}$$

We have

$$
\begin{aligned}
\dot{\sigma}_{10} &= -i[(\omega_1-\omega_0)-(\omega_\ell-\omega_s)]\sigma_{10}+e\frac{i(-\tilde{\mathcal{E}}_s\lambda_{12}\sigma_{20}+\tilde{\mathcal{E}}^*_\ell\lambda_{20}\sigma^*_{21})}{\hbar}\\
\dot{\sigma}_{20} &= -i(\omega_2-\omega_0-\omega_\ell)\sigma_{20}+e\frac{i\lambda_{21}\tilde{\mathcal{E}}^*_s}{\hbar}\sigma_{10}-e\frac{i\lambda_{20}\tilde{\mathcal{E}}^*_\ell}{\hbar}(\sigma_{22}-\sigma_{00})\\
\dot{\sigma}_{21} &= -i(\omega_2-\omega_1-\omega_s)\sigma_{21}+e\frac{i\lambda_{20}\tilde{\mathcal{E}}^*_\ell}{\hbar}\sigma^*_{10}-e\frac{i\lambda_{21}\tilde{\mathcal{E}}^*_s}{\hbar}(\sigma_{22}-\sigma_{11})\\
\dot{\sigma}_{00} &= \frac{ie}{\hbar}(\lambda_{02}\tilde{\mathcal{E}}_\ell\sigma_{20}-\lambda_{20}\tilde{\mathcal{E}}^*_\ell\sigma^*_{20})\\
\dot{\sigma}_{11} &= \frac{ie}{\hbar}(\lambda_{12}\tilde{\mathcal{E}}_s\sigma_{21}-\lambda_{21}\tilde{\mathcal{E}}^*_s\sigma^*_{21})
\end{aligned}
\tag{D.5}
$$

Introducing these into set of Eq. D.3 resluts in

$$
\begin{aligned}
\dot{\sigma}_{10} &= -i\Delta\sigma_{10}-\sigma_{20}\tilde{E}_s-\sigma^*_{21}\tilde{E}^*_\ell\\
\dot{\sigma}_{20} &= -i\Delta_{20,\ell}\sigma_{20}-\sigma_{10}\tilde{E}^*_s+\tilde{E}^*_\ell(\sigma_{22}-\sigma_{00})\\
\dot{\sigma}_{21} &= -i\Delta_{21,s}\sigma_{21}-\sigma^*_{10}\tilde{E}^*_\ell+\tilde{E}^*_s(\sigma_{22}-\sigma_{11})\\
\dot{\sigma}_{00} &= 2\mathrm{Re}(\tilde{E}_\ell\sigma_{20})\\
\dot{\sigma}_{11} &= 2\mathrm{Re}(\tilde{E}_s\sigma_{21})
\end{aligned}
$$

where

$$
\begin{aligned}
\Delta &= (\omega_1-\omega_0)-(\omega_\ell-\omega_s)\\
\Delta_{20,\ell} &= (\omega_2-\omega_0-\omega_\ell)\\
\Delta_{21,s} &= (\omega_2-\omega_1-\omega_s)
\end{aligned}
$$

are detuning defenitions and

$$
\begin{aligned}
\tilde{E}_\ell &= \frac{ie\lambda_{02}\tilde{\mathcal{E}}_\ell}{\hbar}\\
\tilde{E}_s &= \frac{ie\lambda_{12}\tilde{\mathcal{E}}_s}{\hbar}
\end{aligned}
\tag{D.6}
$$

are the Rabi frequencies.

If detuning of transitions to state $|2\rangle$ is much larger than the related Rabi frequencies,i.e., $\Delta_{20,\ell} \gg \tilde{E}_\ell$, $\Delta_{21,s} \gg \tilde{E}_s$, then the time evolution of transitions from levels $|0\rangle$ and $|1\rangle$ to $|2\rangle$ could be ignored

$$\dot{\sigma}_{20} = \dot{\sigma}_{21} = 0 \tag{D.7}$$

as well as the fact that detunings $\Delta_{20,\ell}$ and $\Delta_{21,s}$ are approximately equal due to the large difference between optical and vibrational frequency

$$\Delta_{20,\ell} \approx \Delta_{21,s} = \delta \tag{D.8}$$

and also

$$\sigma_{22} = 0 \tag{D.9}$$

As a result Eq. D.6 are reformed into

$$\begin{aligned}
\dot{\sigma}_{10} &= -i\Delta\sigma_{10} + i(\frac{|\tilde{E}_\ell|^2 - |\tilde{E}_s|^2}{\delta})\sigma_{10} + i\tilde{E}_s\tilde{E}_\ell^*(\frac{\sigma_{11} - \sigma_{00}}{\delta}) \\
\dot{\sigma}_{00} &= 2\mathrm{Re}(\frac{i\tilde{E}_\ell\tilde{E}_s^*\sigma_{10}}{\delta}) \\
\dot{\sigma}_{11} &= 2\mathrm{Re}(\frac{i\tilde{E}_\ell^*\tilde{E}_s\sigma_{10}^*}{\delta}) \\
\sigma_{20} &= i\frac{\sigma_{00}\tilde{E}_\ell^* + \sigma_{10}\tilde{E}_s^*}{\delta} \\
\sigma_{21} &= i\frac{\sigma_{11}\tilde{E}_s^* + \sigma_{10}^*\tilde{E}_\ell^*}{\delta}
\end{aligned}$$

So far equations related to time variation of matter are derived. Now the electromagnetic wave variations can be found by Maxwell's eqaution of electromagnetic wave

$$\frac{\partial^2 E}{\partial z^2} - \frac{n^2}{c^2}\frac{\partial^2 E}{\partial t^2} = \mu_0 \frac{\partial^2 \langle P \rangle}{\partial t^2} \tag{D.10}$$

in which

$$\langle P \rangle = N \mathrm{Tr}(\rho e \hat{\lambda}) \tag{D.11}$$

and $e = 1.6 \times 10^{-19}$C is the unit of electric charge.

$\langle P \rangle$ in Eq. D.11 is a time varying factor with the same frequency as the electric field. Hence the laser field and Raman field are defined as

$$\begin{aligned} \langle P \rangle_\ell &= eN\rho_{20}\lambda_{20} = eN\sigma^*_{20}\lambda_{20}e^{i\omega_\ell t} \\ \langle P \rangle_s &= eN\rho_{21}\lambda_{21} = eN\sigma^*_{21}\lambda_{21}e^{i\omega_s t} \end{aligned} \tag{D.12}$$

Slowly varying amplitude approximation applied on left side of equation Eq. D.10 gives

$$\begin{aligned} &2ik_\ell \frac{\partial \tilde{\mathcal{E}}_\ell}{\partial z} - 2i\omega_\ell \frac{n^2}{c^2}\frac{\partial \tilde{\mathcal{E}}_\ell}{\partial t} \\ &2ik_s \frac{\partial \tilde{\mathcal{E}}_s}{\partial z} - 2i\omega_s \frac{n^2}{c^2}\frac{\partial \tilde{\mathcal{E}}_s}{\partial t} \end{aligned} \tag{D.13}$$

and introducing Eq. D.12 into Eq. D.10 we have

$$\begin{aligned} &\mu_0 eN\lambda_{20}(\ddot{\sigma}^*_{20} + 2i\omega_\ell \dot{\sigma}^*_{20} - \omega_\ell^2 \sigma^*_{20}) \\ &\mu_0 eN\lambda_{21}(\ddot{\sigma}^*_{21} + 2i\omega_s \dot{\sigma}^*_{21} - \omega_s^2 \sigma^*_{21}) \end{aligned} \tag{D.14}$$

where only the last term remains if we ignore the variation of level $|2\rangle$, then

$$\begin{aligned}\frac{\partial\tilde{\mathcal{E}}_\ell}{\partial z}-\frac{n}{c}\frac{\partial\tilde{\mathcal{E}}_\ell}{\partial t}&=\frac{i\mu_0 eN\lambda_{20}\omega_\ell c}{2n}\sigma_{20}^*\\ \frac{\partial\tilde{\mathcal{E}}_s}{\partial z}+\frac{n}{c}\frac{\partial\tilde{\mathcal{E}}_s}{\partial t}&=\frac{i\mu_0 eN\lambda_{21}\omega_s c}{2n}\sigma_{21}^*\end{aligned}\tag{D.15}$$

Then the final set of equations that we should consider is

$$\begin{aligned}\frac{\partial\tilde{E}_\ell}{\partial z}-\frac{n}{c}\frac{\partial\tilde{E}_\ell}{\partial t}&=-\frac{\mu_0 N|e\lambda_{02}|^2\omega_\ell c}{2n\hbar}\sigma_{20}^*\\ \frac{\partial\tilde{E}_s}{\partial z}+\frac{n}{c}\frac{\partial\tilde{E}_s}{\partial t}&=-\frac{\mu_0 N|e\lambda_{12}|^2\omega_s c}{2n\hbar}\sigma_{21}^*\\ \dot{\sigma}_{10}&=-i\Delta\sigma_{10}+i(\frac{|\tilde{E}_\ell|^2-|\tilde{E}_s|^2}{\delta})\sigma_{10}+i\tilde{E}_s\tilde{E}_\ell^*(\frac{\sigma_{11}-\sigma_{00}}{\delta})\\ \dot{\sigma}_{00}&=2\mathrm{Re}(\frac{i\tilde{E}_\ell\tilde{E}_s^*\sigma_{10}}{\delta})\\ \dot{\sigma}_{11}&=2\mathrm{Re}(\frac{i\tilde{E}_\ell^*\tilde{E}_s\sigma_{10}^*}{\delta})\\ \sigma_{20}&=i\frac{\sigma_{00}\tilde{E}_\ell^*+\sigma_{10}\tilde{E}_s^*}{\delta}\\ \sigma_{21}&=i\frac{\sigma_{11}\tilde{E}_s^*+\sigma_{10}^*\tilde{E}_\ell^*}{\delta}\end{aligned}\tag{D.16}$$

In Eq. D.16 coefficients of electromagnetic wave equation are combinations of these

constants

$$
\begin{aligned}
\mu_0 &= 4\pi \times 10^{-7}\ (\frac{\mathrm{Vs}}{\mathrm{Am}}) \\
e &= 1.6 \times 10^{-19}\ (\mathrm{As}) \\
\lambda_{ij} &= 5 \times 10^{-10}\ (\mathrm{m}) \qquad \text{(Bohr radius)} \\
\hbar &= 1.054 \times 10^{-34}\ (\mathrm{Js}) \\
N &= 2 \times 10^{25} (\mathrm{m}^{-3})
\end{aligned}
$$

References

[1] Jean-Claude Diels and Wolfgang Rudolph. *Ultrashort laser pulse phenomena*. Elsevier, second edition, 2006.

[2] Robert Boyd. *Nonlinear Optics*. Academic Press, third edition, 2008.

[3] J.H. Marburger. Self-focusing: Theory. *Progress in Quantum Electronics*, 4:35 – 110, 1975.

[4] Gadi Fibich, Shmuel Eisenmann, Boaz Ilan, Yossi Erlich, Moshe Fraenkel, Zohar Henis, Alexander L. Gaeta, and Arie Zigler. Self-focusing distance of very high power laser pulses. *Opt. Express*, 13(15):5897–5903, Jul 2005.

[5] G. G. Luther, J. V. Moloney, A. C. Newell, and E. M. Wright. Self-focusing threshold in normally dispersive media. *Opt. Lett.*, 19:862–864, 1994.

[6] P. Polynkin, C. Ament, and J. V. Moloney. Self-focusing of ultraintense femtosecond optical vortices in air. *Phys. Rev. Lett.*, 111:023901, Jul 2013.

[7] Aron Bernestein. *Measurements of ultrashort pulses self-focusing in air*. PhD thesis, University of New Mexico, 1995.

[8] S. A. Akhmanov, A. P. Sukhorukov, and R. V. Khokhlov. Self focusing and self trapping of intense light beams in a nonlinear medium. *Sov. Phys JETP*, 23:1025–1033, 1966.

[9] E. Freysz, M. Afifi, A. Ducasse, B. Pouligny, and J. R. Lalanne. Critical microemulsions as optically nonlinear media. *Journal of the Optical Society of America B*, 1:433, 1984.

[10] P. Agostini and L. F. DiMauro. Atoms in high intensity mid-infrared pulses. *Contemporary Physics*, 49(3):179–197, 2008.

[11] A. Braun, G. Korn, X. Liu, D. Du, J. Squier, and G. Mourou. Self-channeling of high-peak-power femtosecond laser pulses in air. *Opt. Lett.*, 20(1):73–75, Jan 1995.

[12] Y. R. Shen. *The Principles of Nonlinear Optics*. John Wiley & Sons, New York, 1984.

[13] M. Mlejnek, E.M. Wright, and J.V. Moloney. Power dependence of dynamic spatial replenishment of femtosecond pulses propagating in air. *Opt. Express*, 4(7):223–228, Mar 1999.

[14] P. Béjot, J. Kasparian, S. Henin, V. Loriot, T. Vieillard, E. Hertz, O. Faucher, B. Lavorel, and J.-P. Wolf. Higher-order kerr terms allow ionization-free filamentation in gases. *Phys. Rev. Lett.*, 104:103903, Mar 2010.

[15] Miroslav Kolesik, D Mirell, J-C Diels, and Jerome V Moloney. On the higher-order kerr effect in femtosecond filaments. *Optics letters*, 35(21):3685–3687, 2010.

[16] S. L. Chin. From multiphoton to tunnel ionization. In *Advances in Multi-Photon Processes and Spectroscopy*, volume 16, chapter 3, pages 249–271. World Scientific, 2004.

[17] Olivier Chalus, Alexey Sukhinin, Alejandro Aceves, and Jean-Claude Diels. Propagation of non-diffracting intense ultraviolet beams. *Optics Communications*, 281(12):3356 – 3360, 2008.

[18] Olivier J. Chalus, Alexey Sukhinin, Alejandro Aceves, and Jean-Claude Diels. High energy, long pulse filaments in air. In *Conference on Lasers and Electro-Optics/Quantum Electronics and Laser Science Conference and Photonic Applications Systems Technologies*, page CPDB6. Optical Society of America, 2007.

[19] J Schwarz and J-C Diels. Uv filaments and their application for laser-induced lightning and high-aspect-ratio hole drilling. *Applied Physics A*, 77(2):185–191, 2003.

[20] Xiaozhen Xu, Chengyong Feng, and Jean-Claude Diels. Optimizing sub-ns pulse compression for high energy application. *Opt. Express*, 22(11):13904–13915, Jun 2014.

[21] C.P. Hauri, W. Kornelis, F.W. Helbing, A. Heinrich, A. Couairon, A. Mysyrowicz, J. Biegert, and U. Keller. Generation of intense, carrier-envelope phase-locked few-cycle laser pulses through filamentation. *Applied Physics B*, 79(6):673–677, 2004.

[22] Johanan H. Odhner, Erin T. McCole, and Robert J. Levis. Filament-driven impulsive raman spectroscopy. *The Journal of Physical Chemistry A*, 115(46):13407–13412, 2011. PMID: 21977899.

[23] B. Prade, M. Franco, A. Mysyrowicz, A. Couairon, H. Buersing, B. Eberle, M. Krenz, D. Seiffer, and O. Vasseur. Spatial mode cleaning by femtosecond filamentation in air. *Opt. Lett.*, 31(17):2601–2603, Sep 2006.

[24] Trenton R. Ensley, Dmitry A. Fishman, Scott Webster, Lazaro A. Padilha, David J. Hagan, and Eric W. Van Stryland. Energy and spectral enhancement of femtosecond supercontinuum in a noble gas using a weak seed. *Opt. Express*, 19(2):757–763, Jan 2011.

[25] J. Kasparian, M. Rodriguez, G. Méjean, J. Yu, E. Salmon, H. Wille, R. Bourayou, S. Frey, Y.-B. André, A. Mysyrowicz, R. Sauerbrey, J.-P. Wolf, and L. Wöste. White-light filaments for atmospheric analysis. *Science*, 301(5629):61–64, 2003.

[26] J. Kasparian, R. Sauerbrey, and S.L. Chin. The critical laser intensity of self-guided light filaments in air. *Applied Physics B*, 71(6):877–879, 2000.

[27] Sergey I Mitryukovskiy, Yi Liu, Aurélien Houard, and André Mysyrowicz. Re-evaluation of the peak intensity inside a femtosecond laser filament in air. *Journal of Physics B: Atomic, Molecular and Optical Physics*, 48(9):094003, 2015.

[28] J. Bernhardt, W. Liu, S.L. Chin, and R. Sauerbrey. Pressure independence of intensity clamping during filamentation: theory and experiment. *Applied Physics B*, 91(1):45–48, 2008.

[29] W. Liu, F. Théberge, E. Arévalo, J.-F. Gravel, A. Becker, and S. L. Chin. Experiment and simulations on the energy reservoir effect in femtosecond light filaments. *Opt. Lett.*, 30(19):2602–2604, Oct 2005.

[30] François Courvoisier, Véronique Boutou, Jérôme Kasparian, Estelle Salmon, Guillaume Méjean, Jin Yu, and Jean-Pierre Wolf. Ultraintense light filaments transmitted through clouds. *Applied Physics Letters*, 83(2):213–215, 2003.

[31] Yurii P Razer. Breakdown and heating of gases under the influence of a laser beam. *Soviet Physics Uspekhi*, 8(5):650, 1966.

[32] A. Couairon and A. Mysyrowicz. Femtosecond filamentation in transparent media. *Physics Reports*, 441(24):47 – 189, 2007.

[33] Gerhard Herzberg. *Molecular spectra and molecular structure*, volume 1. D. Van Nostrand Company, Inc., 2nd edition, 1963.

[34] Henrik Stapelfeldt and Tamar Seideman. *Colloquium* : Aligning molecules with strong laser pulses. *Rev. Mod. Phys.*, 75:543–557, Apr 2003.

[35] G. Fibich and B. Ilan. Multiple filamentation of circularly polarized beams. *Phys. Rev. Lett.*, 89:013901, Jun 2002.

[36] Gadi Fibich and Boaz Ilan. Self-focusing of circularly polarized beams. *Phys. Rev. E*, 67:036622, Mar 2003.

[37] J Liu, X W Chen, R X Li, and T Kobayashi. Polarization-dependent pulse compression in an argon-filled cell through filamentation. *Laser Physics Letters*, 5(1):45, 2008.

[38] J-C Diels, J Yeak, D Mirell, R Fuentes, S Rostami, D Faccio, and P Di Trapani. Air filaments and vacuum. *Laser physics*, 20(5):1101–1106, 2010.

[39] P. B. Corkum, N. H. Burnett, and F. Brunel. Above-threshold ionization in the long-wavelength limit. *Phys. Rev. Lett.*, 62:1259–1262, Mar 1989.

[40] Magali Durand, Aurélien Houard, Bernard Prade, André Mysyrowicz, Anne Durécu, Bernard Moreau, Didier Fleury, Olivier Vasseur, Hartmut Borchert, Karsten Diener, Rudiger Schmitt, Francis Théberge, Marc Chateauneuf, Jean-François Daigle, and Jacques Dubois. Kilometer range filamentation. *Opt. Express*, 21(22):26836–26845, Nov 2013.

[41] Xin Miao Zhao, Jean-Claude Diels, Cai Yi Wang, and Juan Elizondo. Femtosecond ultraviolet laser pulse induced electrical discharges in gases. *IEEE J. Quantum Electr.*, 31:599–612, 1995.

[42] Arthur Dogariu, James B. Michael, Marlan O. Scully, and Richard B. Miles. High-gain backward lasing in air. *Science*, 331(6016):442–445, 2011.

[43] Jinping Yao, Bin Zeng, Huailiang Xu, Guihua Li, Wei Chu, Jielei Ni, Haisu Zhang, See Leang Chin, Ya Cheng, and Zhizhan Xu. High-brightness switchable multiwavelength remote laser in air. *Phys. Rev. A*, 84:051802, Nov 2011.

[44] Yi Liu, Yohann Brelet, Guillaume Point, Aurélien Houard, and André Mysyrowicz. Self-seeded lasing in ionized air pumped by 800 nm femtosecond laser pulses. *Opt. Express*, 21(19):22791–22798, Sep 2013.

[45] Daniil Kartashov, Skirmantas Ališauskas, Andrius Baltuška, Andreas Schmitt-Sody, William Roach, and Pavel Polynkin. Remotely pumped stimulated emission at 337 nm in atmospheric nitrogen. *Phys. Rev. A*, 88:041805, Oct 2013.

[46] N. Aközbek, A. Iwasaki, A. Becker, M. Scalora, S. L. Chin, and C. M. Bowden. Third-harmonic generation and self-channeling in air using high-power femtosecond laser pulses. *Phys. Rev. Lett.*, 89:143901, Sep 2002.

[47] Sergey Mitryukovskiy, Yi Liu, Pengji Ding, Aurélien Houard, and André Mysyrowicz. Backward stimulated radiation from filaments in nitrogen gas and air pumped by circularly polarized 800 nm femtosecond laser pulses. *Opt. Express*, 22(11):12750–12759, Jun 2014.

[48] Daniil Kartashov, Skirmantas Ališauskas, Audrius Pugžlys, Mikhail N Shneider, and Andrius Baltuška. Theory of a filament initiated nitrogen laser. *Journal of Physics B: Atomic, Molecular and Optical Physics*, 48(9):094016, 2015.

[49] Stephen Gasiorowicz. *Quantum Physics*. John Wiley & Sons, 2nd edition, 1996.

[50] Alf Lofthus and Paul Krupenie. The spectrum of molecular nitrogen. *Journal of physical and chemical reference data*, 6(1):113–307, 1977.

[51] Tamar Seideman and Edward Hamilton. Nonadiabatic alignment by intense pulses. concepts, theory, and directions. volume 52 of *Advances In Atomic, Molecular, and Optical Physics*, pages 289 – 329. Academic Press, 2005.

[52] Maxim Artamonov and Tamar Seideman. Theory of three-dimensional alignment by intense laser pulses. *The Journal of Chemical Physics*, 128(15), 2008.

[53] Tamar Seideman. On the dynamics of rotationally broad, spatially aligned wave packets. *The Journal of Chemical Physics*, 115(13):5965–5973, 2001.

[54] D. Daems, S. Guérin, E. Hertz, H. R. Jauslin, B. Lavorel, and O. Faucher. Field-free two-direction alignment alternation of linear molecules by elliptic laser pulses. *Phys. Rev. Lett.*, 95:063005, Aug 2005.

[55] Jakob Juul Larsen, Kasper Hald, Nis Bjerre, Henrik Stapelfeldt, and Tamar Seideman. Three dimensional alignment of molecules using elliptically polarized laser fields. *Phys. Rev. Lett.*, 85:2470–2473, Sep 2000.

[56] Damian N. Schimpf, Tino Eidam, Enrico Seise, Steffen Hädrich, Jens Limpert, and Andreas Tünnermann. Circular versus linear polarization in laser-amplifiers with kerr-nonlinearity. *Opt. Express*, 17(21):18774–18781, Oct 2009.

[57] Oscar Varela, Amelle Zaïr, Julio San Román, Benjamin Alonso, Iñigo Juan Sola, Camilo Prieto, and Luis Roso. Above-millijoule super-continuum generation using polarisation dependent filamentation in atoms and molecules. *Opt. Express*, 17(5):3630–3639, Mar 2009.

[58] D. A. Romanov and R. J. Levis. Postionization medium evolution in a laser filament: A uniquely nonplasma response. *Phys. Rev. E*, 86:046408, Oct 2012.

[59] Ladan Arissian and Jean-Claude Diels. Ultrafast electron plasma index: An ionization perspective. *Journal of Lasers, Optics & Photonics*, 1(1):1–4, 2014.

[60] F. Calegari, C. Vozzi, and S. Stagira. Optical propagation in molecular gases undergoing filamentation-assisted field-free alignment. *Phys. Rev. A*, 79:023827, Feb 2009.

[61] Huailiang Xu, Erik Lotstedt, Atsushi Iwasaki, and Kaoru Yamanouchi. Sub-10-fs population inversion in N_2^+ in air lasing through multiple state coupling. *Nat Commun*, 6, 09 2015.

[62] Jinping Yao, Hongqiang Xie, Bin Zeng, Wei Chu, Guihua Li, Jielei Ni, Haisu Zhang, Chenrui Jing, Chaojin Zhang, Huailiang Xu, Ya Cheng, and Zhizhan Xu. Gain dynamics of a free-space nitrogen laser pumped by circularly polarized femtosecond laser pulses. *Opt. Express*, 22(16):19005–19013, Aug 2014.

[63] Yukikazu Itikawa. Cross sections for electron collisions with nitrogen molecules. *Journal of Physical and Chemical Reference Data*, 35(1):31–53, 2006.

[64] Sergey Mitryukovskiy, Yi Liu, Pengji Ding, Aurélien Houard, Arnaud Couairon, and André Mysyrowicz. Plasma luminescence from femtosecond filaments in air: Evidence for impact excitation with circularly polarized light pulses. *Phys. Rev. Lett.*, 114:063003, Feb 2015.

[65] X. M. Tong, Z. X. Zhao, and C. D. Lin. Theory of molecular tunneling ionization. *Phys. Rev. A*, 66:033402, Sep 2002.

[66] Nist chemistry webbook. https://goo.gl/WmZKDy. Accessed: March 2017.

[67] Russ R. Laher and Forrest R. Gilmore. Improved fits for the vibrational and rotational constants of many states of nitrogen and oxygen. *Journal of Physical and Chemical Reference Data*, 20(4):685–712, 1991.

[68] Stephen R. Langhoff, Charles W. Bauschlicher, and Harry Partridge. Theoretical study of the n+2 meinel system. *The Journal of Chemical Physics*, 87(8):4716–4721, 1987.

[69] Stephen R. Langhoff and Charles W. Bauschlicher. Theoretical study of the first and second negative systems of n+2. *The Journal of Chemical Physics*, 88(1):329–336, 1988.

[70] Jielei Ni, Wei Chu, Chenrui Jing, Haisu Zhang, Bin Zeng, Jinping Yao, Guihua Li, Hongqiang Xie, Chaojin Zhang, Huailiang Xu, See-Leang Chin, Ya Cheng, and Zhizhan Xu. Identification of the physical mechanism of generation of coherent N_2^+ emissions in air by femtosecond laser excitation. *Opt. Express*, 21(7):8746–8752, Apr 2013.

[71] Pavel Polynkin and Miroslav Kolesik. Critical power for self-focusing in the case of ultrashort laser pulses. *Physical Review A*, 87:053829, 2013.

[72] S.V. Pancheshnyi, S.M. Starikovskaia, and A.Yu. Starikovskii. Measurements of rate constants of the n2(c3u,v=0) and n2+(b2+u,v=0) deactivation by n2, o2, h2, {CO} and {H2O} molecules in afterglow of the nanosecond discharge. *Chemical Physics Letters*, 294(6):523 – 527, 1998.

[73] Young Jong Lee and Marcus T. Cicerone. Vibrational dephasing time imaging by time-resolved broadband coherent anti-stokes raman scattering microscopy. *Applied Physics Letters*, 92(4), 2008.

[74] A Mysyrowicz, A Couairon, and U Keller. Self-compression of optical laser pulses by filamentation. *New Journal of Physics*, 10(2):025023, 2008.

[75] Xiaowei Chen, Xiaofang Li, Jun Liu, Pengfei Wei, Xiaochun Ge, Ruxin Li, and Zhizhan Xu. Generation of 5 fs, 0.7 mj pulses at 1 khz through cascade filamentation. *Opt. Lett.*, 32(16):2402–2404, Aug 2007.

[76] J. H. Odhner, D. A. Romanov, and R. J. Levis. Rovibrational wave-packet dispersion during femtosecond laser filamentation in air. *Phys. Rev. Lett.*, 103:075005, Aug 2009.

[77] Scott E. Bisson, John E. M. Goldsmith, and Mark G. Mitchell. Narrow-band, narrow-field-of-view raman lidar with combined day and night capability for

tropospheric water-vapor profile measurements. *Appl. Opt.*, 38(9):1841–1849, Mar 1999.

[78] P. N. Malevich, D. Kartashov, Z. Pu, S. Ališauskas, A. Pugžlys, A. Baltuška, L. Giniūnas, R. Danielius, A. A. Lanin, A. M. Zheltikov, M. Marangoni, and G. Cerullo. Ultrafast-laser-induced backward stimulated raman scattering for tracing atmospheric gases. *Opt. Express*, 20(17):18784–18794, Aug 2012.

[79] William H. Press, Saul A. Teukolsky, William T. Vetterling, and Brian P. Flannery. *Numerical Recipes in Fortran 90, The Art of Parallel Scientific Computing*, volume 1. Cambridge University Press, 2nd edition, 1996.

[80] Maik Scheller, Matthew S. Mills, Mohammad-Ali Miri, Weibo Cheng, Jerome V. Moloney, Miroslav Kolesik, Pavel Polynkin, and Demetrios N. Christodoulides. Externally refuelled optical filaments. *Nat Photon*, 8(4):297–301, 04 2014.

[81] J. Durnin, J. J. Miceli, and J. H. Eberly. Diffraction-free beams. *Phys. Rev. Lett.*, 58:1499–1501, Apr 1987.

[82] Masood Ghotbi, Peter Trabs, Marcus Beutler, and Frank Noack. Generation of tunable sub-45 femtosecond pulses by noncollinear four-wave mixing. *Opt. Lett.*, 38(4):486–488, Feb 2013.

[83] E. T. J. Nibbering, G. Grillon, M. A. Franco, B. S. Prade, and A. Mysyrowicz. Determination of the inertial contribution to the nonlinear refractive index of air, N_2, and O_2 by use of unfocused high-intensity femtosecond laser pulses. *J. Opt. Soc. Am. B*, 14(3):650–660, Mar 1997.

[84] George B. Arfken, Hans J. Weber, and Frank E. Harris. Chapter 15 - legendre functions. In George B. Arfken, Hans J. Weber, and Frank E. Harris, editors, *Mathematical Methods for Physicists (Seventh Edition)*, pages 715 – 772. Academic Press, Boston, seventh edition, 2013.